Relationship between Aerosol Properties and Characteristics of Supercooled Clouds Using Lidar

Master Thesis in Meteorology
to award the academic degree
Master of Science

Kevin Ohneiser
Matriculation number: 3706099

Contact Person: Dr. Patric Seifert

First Supervisor: Prof. Dr. Andreas Macke

Second Supervisor: Jun.-Prof. Dr. Heike Kalesse

University of Leipzig
Faculty of Physics and Earth Sciences
Leipzig Institute for Meteorology
Leibniz Institute for Tropospheric Research

Date of Submission: 16 November 2019

Abstract

Aerosol particles play a key role for the formation of clouds. However, underlying mechanisms such as the influence of aerosol particles on the glaciation of clouds due to heterogeneous freezing are still not completely understood. There are many studies showing the relationship between cloud-top temperature and heterogeneous freezing by using models as a proxy for the aerosol load. However, this Master's thesis presents a new approach for the investigation of the relationship between aerosol properties and the characteristics of supercooled clouds using the ground-based remote sensing Polly^{XT} lidar (light detection and ranging) technique. The research vessel (RV) Polarstern cruise PS116 from Bremerhaven (Germany) to Cape Town (South Africa) from 10 November to 11 December 2018 was a unique opportunity to test this new approach. Ice nucleating particles (INP) play a key role for heterogeneous freezing at temperatures between 0°C and −38°C. The new part of the approach especially deals with the retrieval of the number concentration of INP using the lidar technique. This new approach was tested on board of RV Polarstern and at a lidar Polly^{XT} site in Dushanbe (Tajikistan). The results were compared to the number concentration of ice nucleating particles retrieved from the MACC (monitoring atmospheric composition and climate) model. Finally, the number concentration of ice nucleating particles was brought into context to the thermodynamic phase of clouds being obtained from the lidar measurements. In addition, the minimal (in case of a mixed-phase cloud) and maximal (in case of a pure liquid water cloud) possible diameters (assuming spherical ice crystals) and radar reflectivities, which would have been measured by a cloud radar (if available), were calculated. This was done by using the threshold of $1 \cdot 10^{-6}\,\mathrm{kg\,m^{-3}}$ as the minimal possible lidar-detectable atmospheric ice water content. In three different case studies, it was found that INP number concentrations of $0.9\,\mathrm{L^{-1}}$ (from lidar) or $0.5\,\mathrm{L^{-1}}$ (from MACC) were sufficient in order to form ice in a supercooled liquid cloud layer at −24°C cloud-top temperature close to Cape Verde. The minimal possible diameters of spherical ice crystals were calculated to 160.8 µm and 132.2 µm from MACC and lidar, respectively. The theoretically calculated minimal possible radar reflectivities would have been −27.9 dBZ and −30.5 dBZ from MACC and lidar, respectively. The second case study showed that $0.1\,\mathrm{L^{-1}}$ (from lidar) or $0.2\,\mathrm{L^{-1}}$ (from MACC) were not sufficient to form ice in a supercooled liquid cloud layer at −21°C in the English Channel. The minimal possible diameters of spherical ice crystals were calculated to 218.2 µm and 275.0 µm from MACC and lidar, respectively. The theoretically calculated minimal possible radar reflectivities would have been −23.9 dBZ and −20.9 dBZ from MACC and lidar, respectively. The third case study showed that at a cloud-top temperature of −9°C in Tajikistan an INP number concentration of $0.1\,\mathrm{L^{-1}}$ (from lidar) or $0.05\,\mathrm{L^{-1}}$ (from MACC) was sufficient in order to form a mixed-phase cloud. The minimal possible diameters of spherical ice crystals were calculated to 275.0 µm from lidar, and 347.4 µm from MACC. The theoretically calculated minimal possible radar reflectivity would have been −20.9 dBZ from lidar, or −17.8 dBZ from MACC. It is shown that the new approach using the lidar technique principally delivers appropriate results, but at the current stage of the technique the amount of uncertainty is high.

Contents

1 Motivation

Aerosol particles have a large impact on the climate of Earth and play a key role for the formation of clouds (Charlson et al., 1992). Especially the knowledge about indirect effects such as the interaction of aerosols with clouds is limited (Boucher et al., 2013). This results in large uncertainties about their importance for the Earth's climate (Rosenfeld et al., 2014). A better understanding of aerosol-cloud interaction processes can lead to enhanced forecast skills of weather and climate models in terms of cloud albedo, cloud life time, and precipitation patterns (Seinfeld et al., 2016). Whereas direct aerosol effects like the aerosol-radiation interaction are easier to model or measure, it is difficult to measure and detect the interaction between aerosols and clouds (Twomey (1977), Boucher et al. (2013)). Especially aerosol particles acting as ice nucleating particles for the heterogeneous freezing process (see Section 2.1) between 0°C and −38°C play a key role for glaciating supercooled clouds (Kanitz et al. (2011), Hoose and Möhler (2012)).
Many laboratory studies have been conducted studying the dependence of aerosol type and heterogeneous freezing temperatures (Murray et al. (2012), Hoose and Möhler (2012)). However, a direct relationship between aerosol properties and cloud microphysics under real atmospheric conditions has not been established yet. Nevertheless, there are indications for dependencies between aerosols and clouds in several studies which use model-derived aerosol information as a proxy for the availability of ice nucleating particles. Sassen et al. (2003) present indications that Saharan dust storms are capable of glaciating supercooled altocumulus clouds. Seifert et al. (2010) divide a long-term data set in Leipzig into aerosol-laden and aerosol-free (aerosol-free meaning almost aerosol-free, less than $1{\cdot}10^{-3}$ µg m^{-3}) and find an increased fraction of ice-containing clouds in the aerosol-laden situation. Seifert et al. (2015) conclude an aerosol-related increase of the fraction of ice-containing clouds during the dry season of the Brazilian Amazon due to the increased biomass burning activities.
There are different techniques for measuring cloud and aerosol properties (Lihavainen et al., 2010). The satellite remote sensing technique has a good spatial coverage but a coarse spatial resolution, meaning that aerosol information cannot be retrieved or brought into relationship with cloud layers (Nakajima et al., 2001). In situ measurements make it possible to detect aerosols and microphysical properties of clouds without using assumptions but measurements are restricted to narrow parts of the cloud or might be limited in the number of measurements (Pratt et al., 2009). Another approach to detect aerosol-cloud interaction is the ground-based remote sensing lidar technique (Althausen et al., 2009). It is possible to retrieve cloud properties (see Section 3.4), optical properties of aerosol layers (see Section 3.5), and microphysical properties like the number concentration of ice nucleating particles (see Section 3.6). The advantage over in situ measurements is the availability of continuous as well as long-term measurement records.
The above presented studies (Sassen et al. (2003), Seifert et al. (2010), Seifert et al. (2015)) all have in common that they rely on model data for determining aerosol type and aerosol load, and bring it in relationship with cloud properties. However, those relationships have not been drawn yet by using measurements only. Improved lidar techniques as well as improved methods enable to obtain aerosol information from lidar measurements directly ((Illingworth et al., 2015), Mamouri and Ansmann (2016), Jimenez et al. (2017)). This will be an improvement compared to existing studies and will be used for the following Master's thesis. An approach showing how to relate aerosol properties to cloud properties by lidar measurements is presented in here.
Basis for the study will be lidar measurements which were conducted in the frame of research vessel (RV) Polarstern cruise PS116 from Bremerhaven to Cape Town from 10

November 2018 to 11 December 2018. These observation will enable to study the aerosol-cloud interaction in different climate zones and especially in regions of different dominating aerosol types like sulfates, dust, organics, and sea salt. Concretely, three case studies (two from RV Polarstern and one additional case study from the lidar located in Dushanbe in Tajikistan) will be presented, relating the direct influence from ice nucleating particles to the thermodynamic phase of clouds.
The following Sections are structured as follows. Section 2 will focus on the physical background of heterogeneous freezing and the technical details of the lidar instrument. Section 3 presents the general approach in order to relate aerosol properties to cloud properties. This includes the Raman and Klett lidar analysis methods, the depolarization ratio, methods how to retrieve cloud boundaries and the cloud phase, retrieval of aerosol properties as well as the retrieval of ice nucleating particle profiles. Section 4 shows existing cloud statistics focusing on different aerosol loads, regions, and seasons. Section 5 shows preparatory studies before presenting the actual case studies including the new approach. These preparatory studies include a general overview over the route of Polarstern, the cloud situation through the whole measurement period from 10 November 2018 to 11 December 2018, and an overview of the MACC-modeled (Monitoring Atmospheric Composition and Climate) aerosol concentration. Furthermore, a comparison of the vertical temperature profile between model and radiosonde, the retrieval of a standard reference backscatter coefficient, as well as the comparison between different INP parametrizations were performed to evaluate the quality of the following case studies. The three case studies shown in Section 6 consist of one case of a mixed-phase cloud observed from RV Polarstern close to Cape Verde, one case of a supercooled liquid water cloud observed from RV Polarstern in the English Channel, and one mixed-phase cloud case observed with a lidar located in Dushanbe (Tajikistan) as there is a high aerosol concentration. The derived aerosol properties from the lidar measurement are compared to the MACC-model-derived aerosol properties. Section 7 summarizes and concludes.

2 Physical and technical background

This Section will focus on the physical background, explaining different mechanisms of heterogeneous freezing and the lidar technique used during PS116. Additionally, a statistical study on heterogeneous freezing under real atmospheric conditions is discussed.

2.1 Heterogeneous freezing

The heterogeneous freezing process describes the process when aerosols which have an insoluble component trigger glaciation of supercooled liquid water droplets. This process requires ice nucleating particles. Below approximately −38°C homogeneous freezing starts to be effective also with soluble aerosol components. In order to clearly separate the heterogeneous freezing process from the homogeneous freezing process the temperature range between 0°C and −38°C is chosen for the analysis. The heterogeneous freezing process requires an ice nucleus which triggers the ice formation. This ice nucleus is part of an ice nucleating particle which itself contains a certain number of ice nuclei (Vali et al., 2015). The number of ice nuclei on an ice nucleating particle depends on the temperature, supersaturation, and the material. The probability of an ice nucleus to form ice heterogeneously can be expressed by the singular description and the stochastic description which are time-independent and time-dependent models (Vali et al., 2015).
Figure 1 illustrates the different types of heterogeneous freezing as shown in Hoose and Möhler (2012). In addition, (homogeneous) freezing of an aqueous solution droplet would take place at temperatures below approximately −38°C and happens without the interaction with an aerosol particle (Pruppacher, 1995). As described, heterogeneous freezing requires an aerosol particle. Different freezing types are differently efficient at different temperatures and supersaturation with respect to ice or liquid water (hereafter referring to ice as solid-phase water and water as liquid water). The highest temperatures and lowest supersaturation above water are required for the contact freezing mechanism. Contact freezing requires a supercooled liquid water droplet and an aerosol that hits the supercooled droplet. An air-water-particle triple interface is formed and the droplet can freeze immediately (Vali et al., 2015). Furthermore, it freezes if the ice nucleating particle from outside is more efficient than the insoluble one within the droplet (Seifert, P., 2011).
Higher supersaturation above water and lower temperatures are needed for the immersion freezing process. For the immersion freezing process the supercooled liquid water droplet will further cool as it is further lifted in altitude in the cloud for example, the supersaturation above water will increase and therefore freezing will occur immersing the particle into the droplet (Seifert, P., 2011). The ice nucleating particle is already dispersed within the supercooled liquid water droplet (this is the only difference to contact freezing) and has a different effectiveness than contact freezing therefore. It is hard to differentiate between both processes, also in laboratory studies (Vali et al., 2015).
At temperature regimes between −20°C and −30°C condensation nucleation is most efficient. A supercooled droplet grows from condensation and at a certain size an insoluble fraction of the haze particle or the cloud condensation nucleus itself triggers the ice formation (Seifert, P., 2011).
Quite low supersaturation above liquid water but low temperatures between −30°C and −38°C are usually required for the deposition freezing. The water vapor will deposit on an ice nucleating particle from the gaseous phase to the solid phase without the liquid phase (Seifert, P., 2011).
In Fig. 2 different aerosol types like black carbon, ammonium sulfate, organics, dust, and

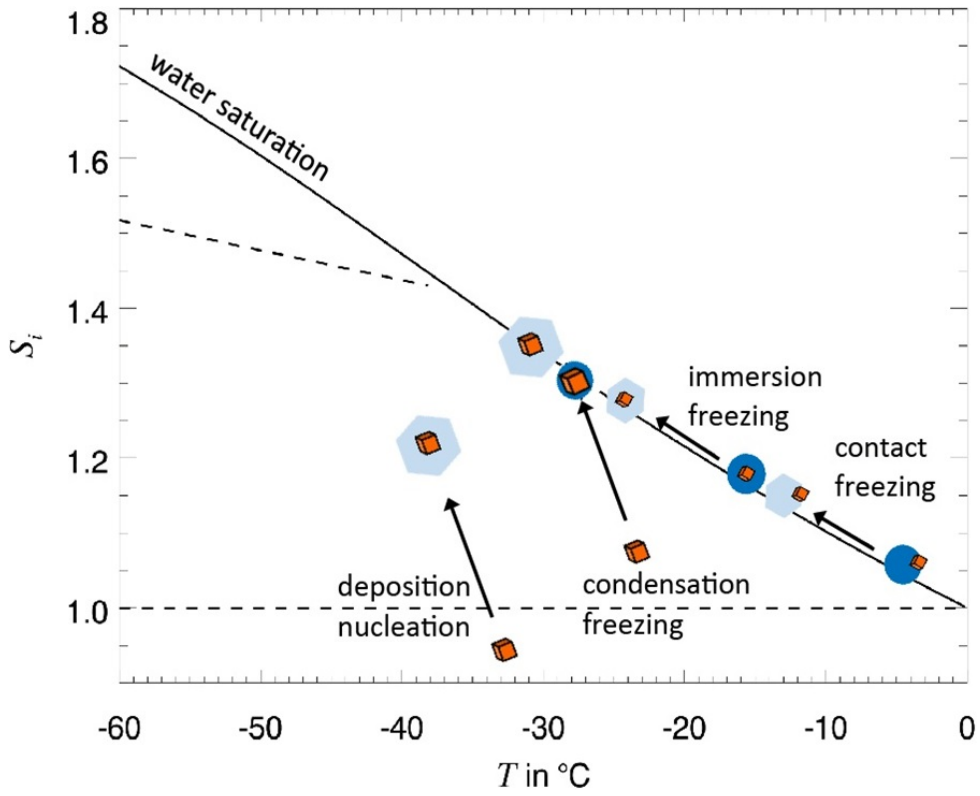

Figure 1: Different types of heterogeneous freezing are shown. The lowest supersaturation above liquid water and lowest supercooling are required for contact freezing, lower temperatures or higher supersaturation above water are needed for immersion freezing, condensation nucleation, and deposition freezing. The lowest temperatures of below −38°C are required for homogeneous freezing (Hoose and Möhler, 2012).

bioaerosols are shown in their efficiency to form ice depending on supersaturation above ice or water and temperature for deposition nucleation, condensation nucleation, and immersion nucleation. It appears that for all aerosol types immersion freezing is already more efficient at higher temperatures than deposition freezing and condensation freezing (Hoose and Möhler, 2012).

According to the review of Hoose and Möhler (2012), bioaerosols (green) are the most efficient ice nucleating particles, being active already at temperatures slightly below 0°C and supersaturation ratios slightly above 1. Dust is usually a less efficient ice nucleating particle than bioaerosols. As higher concentrations of dust can usually occur more frequently than high concentrations of bioaerosols, it still needs to be considered as an efficient ice nucleating particle if bioaerosols are almost absent. Organics, sulfate, and black carbon appear to be inefficient ice nucleating particles, even though in their study there are some indications that black carbon may be efficient for deposition / condensation nucleation between −5°C and −15°C.

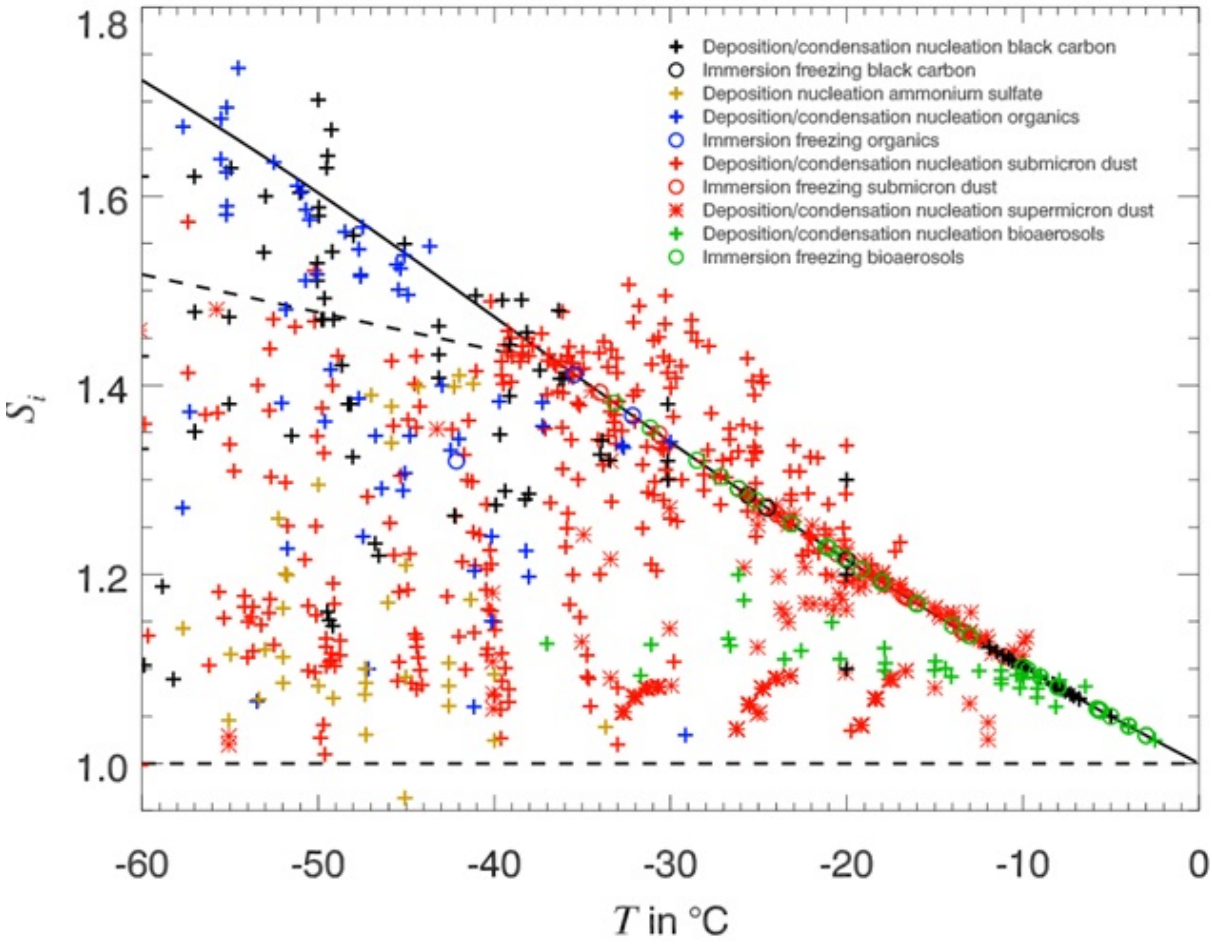

Figure 2: Efficiency of deposition / condensation / immersion freezing as function of temperature and supersaturation above liquid water for black carbon, ammonium sulfate, organics, dust, and bioaerosols. Bioaerosols are the most efficient ice nucleating particles at high temperatures, followed by dust. Black carbon, ammonium sulfate, and organics are not efficient at high temperatures (Hoose and Möhler, 2012).

2.2 Lidar technique

As discussed in Sec. 2.1, information about aerosol and atmospheric conditions are required for the investigation of freezing processes. A technique which enables the observation of aerosols and cloud hydrometeors under ambient atmospheric conditions is the lidar technique. The principle of the optical active remote sensing lidar technique can best be presented by means of the lidar equation 1. First of all a laser beam is emitted with the power $P_0(\lambda)$. It interacts with the atmosphere and its gaseous and particulate constituents and is modified by geometrical effects (Weitkamp (2005), (Seifert, P., 2011)). After transmission, scattering, and absorption processes in the atmosphere, parts of the laser beam are scattered backward. This part is described by the power $P(R, \lambda)$ that is received from a certain distance R and at a certain wavelength λ.

$$P(R, \lambda) = P_0(\lambda) E(\lambda) \frac{O(R)}{R^2} \beta(R, \lambda) T(R, \lambda) \tag{1}$$

The laser beam interacts with the atmosphere and will be absorbed, scattered, and transmitted there. The equation considers the atmospheric transmission $T(R, \lambda) = e^{-\tau(R,\lambda)}$ with the optical depth $\tau(R, \lambda) = 2 \int_0^R \alpha(R, \lambda) \mathrm{d}r$. α is the extinction coefficient of aerosols and air molecules (extinction as absorption plus scattering) and the factor 2 arises from

the beam traveling twice through the atmosphere. A special way of scattering is the backscattering β at an angle of 180° from the atmosphere.
The geometric factor $\frac{O(R)}{R^2}$ contains the overlap function $O(R)$. At the lowest height above the lidar not all parts of the emitted laser that are scattered backward will reach the telescope due to its limited field of view. At a certain height this problem disappears and the overlap equals 1. Using different fields of view, different overlap functions will arise and microphysical properties can be distinguished (Schmidt et al., 2013). Furthermore, the power of the laser pulse decreases by a factor of R^{-2} with range.
The factor $E(\lambda)$ describes the performance of the lidar system. It includes the laser pulse length, the speed of light, the transmissivity of the optical components, and the area of the telescope.
The particle backscatter coefficient and particle extinction coefficient can be derived from the Raman or Klett method (see Section 3.2).
Resolving Eq. 1 for the product of the two directly measured parameters $P(R, \lambda)$ and R^2, yields the range-corrected signal, which is a typical approach for displaying the raw measurements of a lidar. The range-corrected signal is in some instances referred to as the uncalibrated attenuated backscatter coefficient (see, e.g., Fig. 9), because it represents the superposition of atmospheric and particulate backscatter and attenuation in arbitrary units (not-corrected for any system parameters).
In the frame of this study, a lidar system of type Polly$^{\mathrm{XT}}$ Arielle (portable lidar) was deployed on the RV Polarstern. The setup of Polly$^{\mathrm{XT}}$ is illustrated in Fig. 3. The upper part of the Figure shows the frontal view of the lidar, whereas the lower part of the Figure shows the view from above. A laser emits pulses of light of certain energy at 1064-nm wavelength. Parts of the energy are doubled and tripled in frequency, resulting in the additional emission of light at 532 and 355 nm. The atmospheric constituents will partly transmit, absorb, and scatter radiation. Parts of the beam will be scattered at an angle of 180° backward. The beam will be collected by the telescope and forwarded to optical analyzers which makes it possible to retrieve height dependent physical quantities after data acquisition. Arielle has 532-nm dual-field-of-view detectors sensitive to cross-polarized light, and the total signal at 532-nm, as well as the 607-nm vibrational-rotational Raman signal of nitrogen. Further detectors operate in the 355 nm wavelength range with the total and the cross-polarized radiation, the 387 nm vibrational-rotational Raman signal of nitrogen, the 407 nm vibrational-rotational water vapor channel and the 1064 nm total signal.
The detectors for the cross-polarized component of the backscattered light allow to measure the depolarization ratio at 355 nm and 532 nm (see Section 3.3). From the 387 nm and 355 nm wavelength measurements the extinction coefficient, backscatter coefficient and extinction-to-backscatter ratio (lidar ratio) at 355 nm can be determined, and from the 607 and 532-nm wavelength measurements the extinction coefficient, backscatter coefficient and lidar ratio at 532 nm can be determined via the Raman or Klett method (see Section 3.2). Additionally, the backscatter coefficient at 1064 nm can be determined from the Klett method from the 1064 nm total signal.

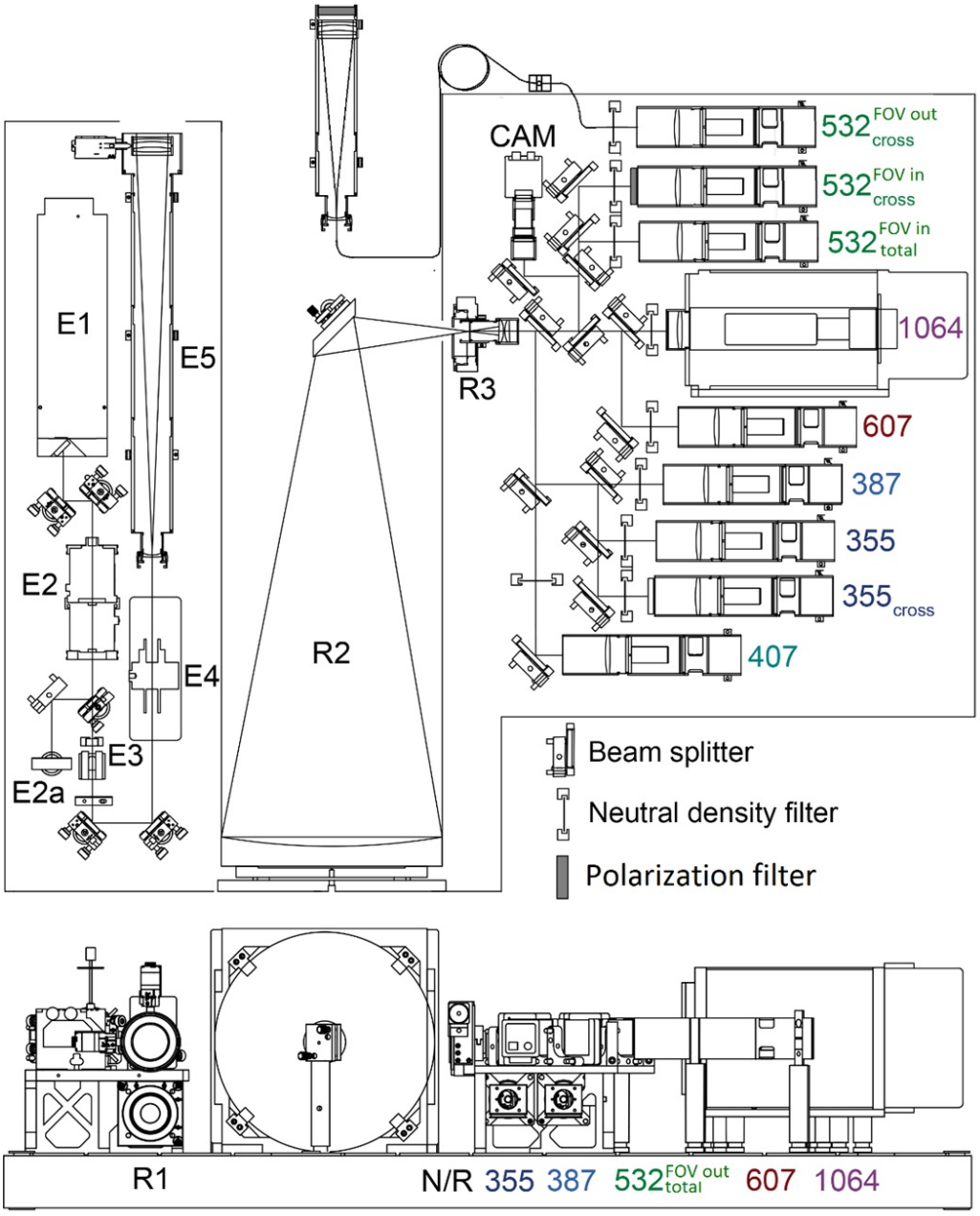

Figure 3: The setup of the extended portable lidar Polly^{XT} Arielle operated on board of the RV Polarstern is illustrated. A laser emits pulses of light of certain energy and 1064-nm wavelength. Parts of the energy are doubled and tripled in frequency, resulting in the emission of light at 532 and 355 nm. The atmosphere transmits, absorbs, and scatters radiation. Parts of the beam will be scattered 180° backward and collected by the telescope and forwarded to optical analyzers. Arielle has 532-nm dual-field-of-view (FOV) detectors sensitive to cross-polarized light, and the total signal at 532 nm, as well as the 607-nm vibrational-rotational Raman signal. Further detectors operate in the 355-nm wavelength range with the total and the cross-polarized radiation, the 387-nm vibrational Raman signal, the 407 nm vibrational-rotational water vapor channel and the 1064 nm total signal. This allows to measure lidar ratio and depolarization ratio at 355 nm and 532 nm, and the backscatter coefficient at 1064 nm. From the dual-field-of-view receiver, microphysical cloud properties can be derived based on exploitation of multiple scattering effects (Jimenez et al., 2017).

2.3 Heterogeneous freezing under real atmospheric aerosol conditions

Apart from laboratory studies on heterogeneous freezing there are also existing studies on heterogeneous freezing under real atmospheric conditions (Seifert et al. (2010), Kanitz et al. (2011), Seifert et al. (2015)). Analyzing the lidar data obtained over a long time period at a measurement site allows the acquisition of cloud statistics. For the whole period the clouds are first separated and analyzed with respect to their cloud-top height. Afterward, radiosonde data is utilized to derive information about the temperature at the height of the cloud-top, which is the cloud-top temperature and usually the coldest region of the cloud. If the cloud-top temperature is between 0°C and −38°C, the cloud is included into the statistics (if there is no cloud layer present within 1000 m above cloud-top height to exclude ice seeding effects from colder clouds). If the cloud is included into the statistics the cloud phase is determined by looking at the combined backscatter coefficient measurements, and depolarization ratio measurements as described in 3.4. In a specific temperature range, the ratio of clouds containing ice or not containing ice can be formed and brought into the statistics as shown in Fig. 4.
Figure 4 hence shows the fraction of ice-containing clouds sorted by different places on Earth in the temperature regime of heterogeneous freezing between 0°C and -38°C. Generally, the fraction of ice-containing clouds increased at lower temperatures. Nevertheless, there were large differences between the different stations. At −15°C cloud-top temperatures Cape Verde clouds and Punta Arenas (Chile) clouds usually did not contain ice (<10%) (Ansmann et al., 2009), Stellenbosch (South Africa) clouds and Atlantic ocean (RV Polarstern) clouds contained ice in 20%, and clouds at Leipzig (Germany) and in the Arctic contained ice in 50-80% of the cases (Seifert et al. (2010), Kanitz et al. (2011)).
Especially Arctic coupled clouds (no temperature inversion between cloud base and surface) contained ice likelier by a factor of approximately 15 compared to Cape Verde clouds at −15°C (unpublished results based on a student assistant's work of Kevin Ohneiser). Already at −5°C large differences were observed. Whereas Arctic coupled clouds contained ice in 80% already, clouds in all the other presented places contained ice in less than 10%. This shows that glaciation of clouds is not a function of temperature only but also a strong function of region and even meteorological situation as can be seen from the large fraction of ice-containing clouds in Arctic coupled clouds compared to the uncoupled clouds (temperature inversion between cloud base and surface). It may be speculated that coupled Arctic clouds had a continuous supply of aerosols from below whereas uncoupled free-tropospheric clouds seemed to behave similar to clouds at Leipzig in terms of glaciation.

Noticeable from Fig. 4 is a generally larger fraction of ice-containing clouds in the northern hemisphere (especially Leipzig and the Arctic (PASCAL, Physical feedbacks of Arctic boundary layer, Sea ice, Cloud and AerosoL) region) than in the southern hemisphere (especially Stellenbosch and Punta Arenas). It is quite surprising that heterogeneous freezing seems to be differently efficient around the world. However, there are large hemispheric and regional differences in aerosol type and aerosol load as Fig. 5 and Fig. 6 illustrate. These regional differences of aerosol characteristics may be related to the regional differences of heterogeneous freezing efficiency. The concrete connections are further studied for example when looking at ice crystal number concentrations from ground-based remote sensing technique (Bühl et al., 2019).
Figure 5 shows a simulation of the distribution of aerosol types worldwide on 17 Aug 2006. This was a typical situation of the distribution of different aerosol types. Organics and black carbon mainly originate from the southern hemispheric tropical rainforests in Africa

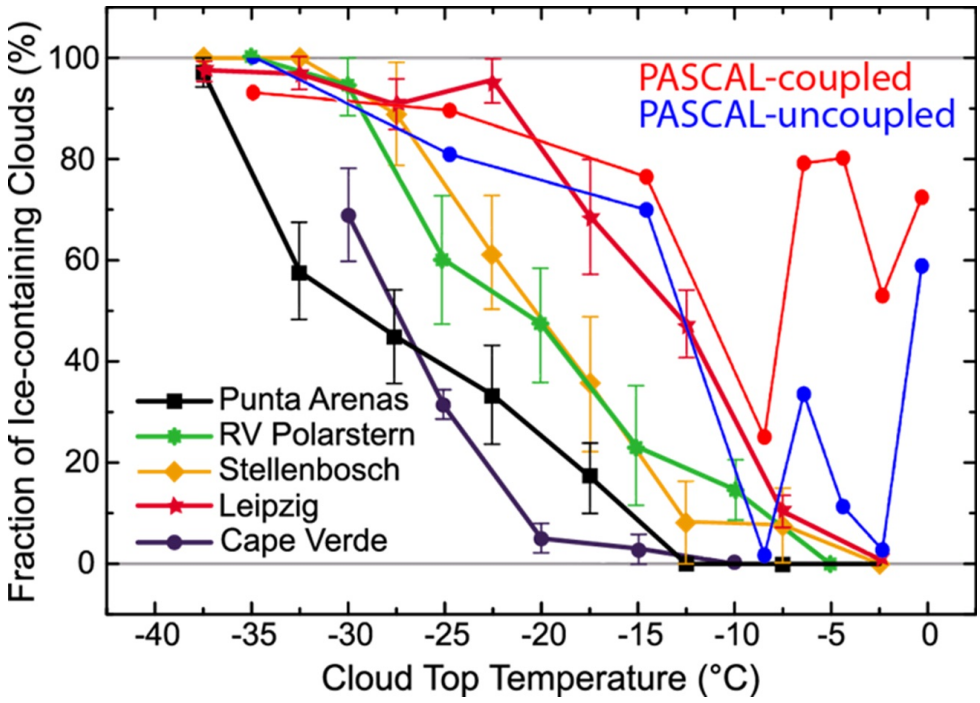

Figure 4: The fraction of ice-containing clouds as a function of cloud-top temperature for different places on Earth. Punta Arenas in Southern Chile (53.17°S, 70.93°W), Stellenbosch in western South Africa (33.92°S, 18.86°E), Leipzig in eastern Germany (51.33°N 12.38°E), RV Polarstern over the Atlantic ocean between Germany and South Africa, Cape Verde in the west of Africa (14.92°N, 23.52°W) and PASCAL (Physical feedback of Arctic planetary boundary level, Sea ice, Cloud and Aerosol) in the Arctic region in a larger area around 78.217°N 15.633°E, coupled meaning that there is no temperature inversion between the surface and the cloud base, uncoupled meaning that there is a temperature inversion. Generally regions with larger aerosol load (see Fig. 6) have a higher fraction of ice-containing clouds at the same cloud-top temperatures (based on Kanitz et al. (2011)).

and the Amazon. Dust mainly moves from northern hemispheric subtropical deserts. The largest dust source worldwide is the Sahara, also with large amounts of westward moving mineral dust over the Atlantic ocean. Sulfate aerosols mainly occur around highly industrialized regions such as Europe, eastern Asia, and northern America. Sea salt exists over all oceans with highest concentrations along the polar front. RV Polarstern may travel through all regions of different aerosol types, ranging from sulfates close to the European continent, dust in the west of the Saharan desert, organics and black carbon in the west of the African tropical rainforests, sea salt spread all over the oceans, and a clean atmosphere on the southern hemisphere and the polar regions.

Not only the aerosol type but also the aerosol load might be a leading factor for heterogeneous ice formation (Seifert et al., 2010). Figure 6 shows the globally resolved averaged aerosol optical depth for November 2018, also during the cruise PS116. The largest mean aerosol optical depths were reached in highly anthropogenically polluted areas like China and India. Naturally, the highest average aerosol optical thickness is reached over deserts. Important to note for the RV Polarstern cruise is the on average westwards traveling dust plume from the Sahara over the Atlantic.

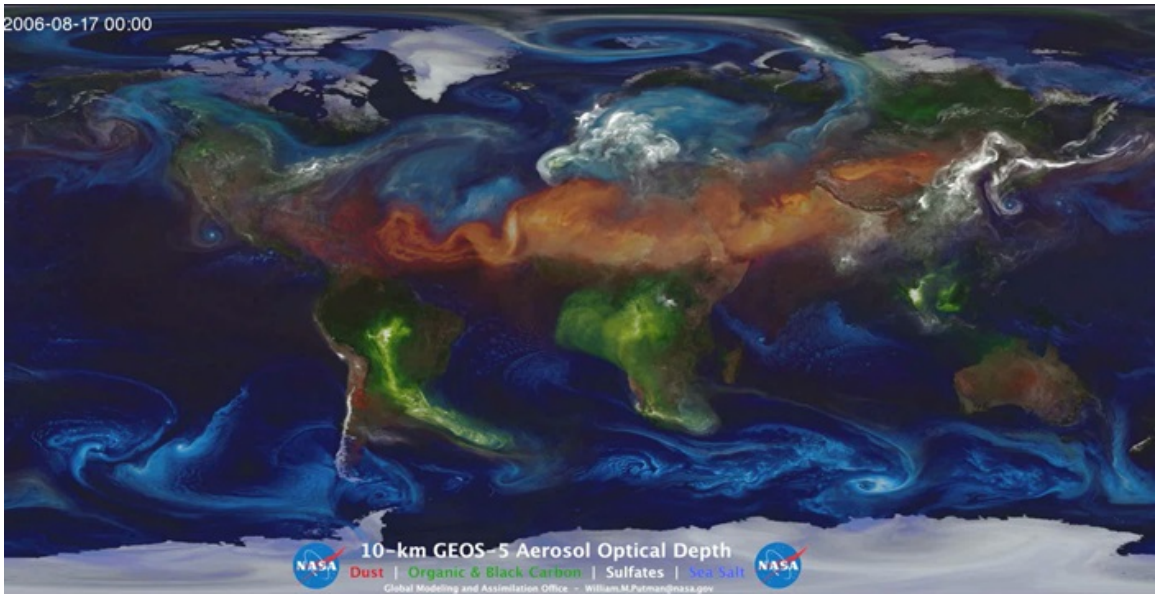

Figure 5: Snapshot of a simulation of the global distribution of aerosol types for 17 Aug 2006 (which represents a typical situation). Orange colored is dust, green colored is organic and black carbon, white colored are sulfates, and blue are sea salt aerosols. Orange, green, white, and blue shades represent dust, organics/black carbon, sulfates, and sea salt, respectively (Pawson, S., 2017).

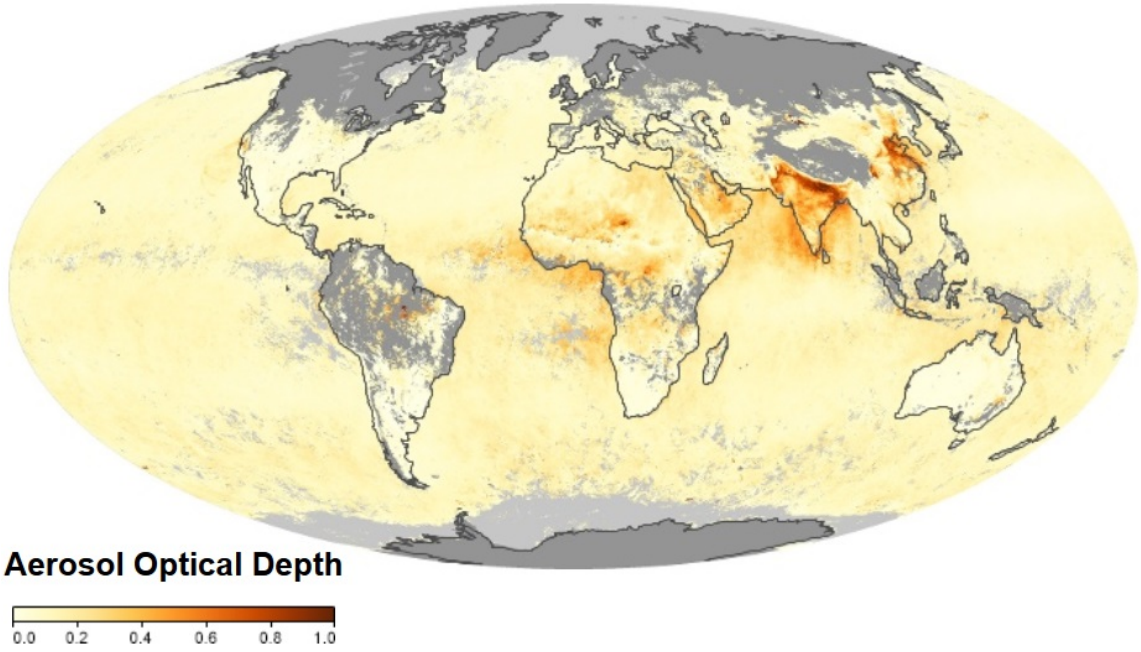

Figure 6: Global monthly-averaged aerosol optical depth for November 2018 based on observations from the Moderate Resolution Imaging Spectroradiometer (MODIS) on NASA's Terra satellite are illustrated. The largest aerosol optical depths are reached in anthropogenically polluted areas like China and India, and naturally over the desert zones. Important for the RV Polarstern cruise are the on average westwards traveling dust plume from the Sahara over the Atlantic as well as the biomass burning plume from Africa (NASA Earth Observatory, 2019).

3 Methods

The following Section presents methods that are applied in order to study the aerosol-cloud interaction from lidar measurements. The general approach of detecting heterogeneous freezing is presented. The Raman and Klett method are presented and the definition and application of the depolarization ratio will be explained. Besides, the detection of cloud boundaries as well as the classification into the cloud phase are shown. The retrieval of aerosol characteristics and the ice nucleating particle profiles will be explained.

3.1 General approach to relate aerosol properties to thermodynamic cloud phase

The detection of aerosol-cloud interaction is a hard venture. An approach to study heterogeneous freezing in clouds is presented. Figure 7 shows a scheme of the data analysis steps.
For the general approach it is necessary to classify the cloud characteristics (see Section 3.4), aerosol characteristics (see Section 3.5) and to retrieve ice nucleating particle profiles (see Section 3.6). Cloud layers with cloud base and cloud top can be determined from the backscatter coefficient (see Section 3.2) like shown in Section 3.4. From the cloud-top height the cloud-top temperature can be obtained from radiosondes. From the depolarization ratio (see Section 3.3) the cloud phase can be retrieved as shown in Section 3.4. In a next step aerosols are differentiated in their type as described in Section 3.5. Furthermore, the aerosol load will be determined from the particle backscatter coefficient. Additionally, profiles of ice nucleating particles will be retrieved as shown in Section 3.6. In the end, ice nucleating particles are brought into context to the phase of clouds in dependence on the cloud-top temperature.

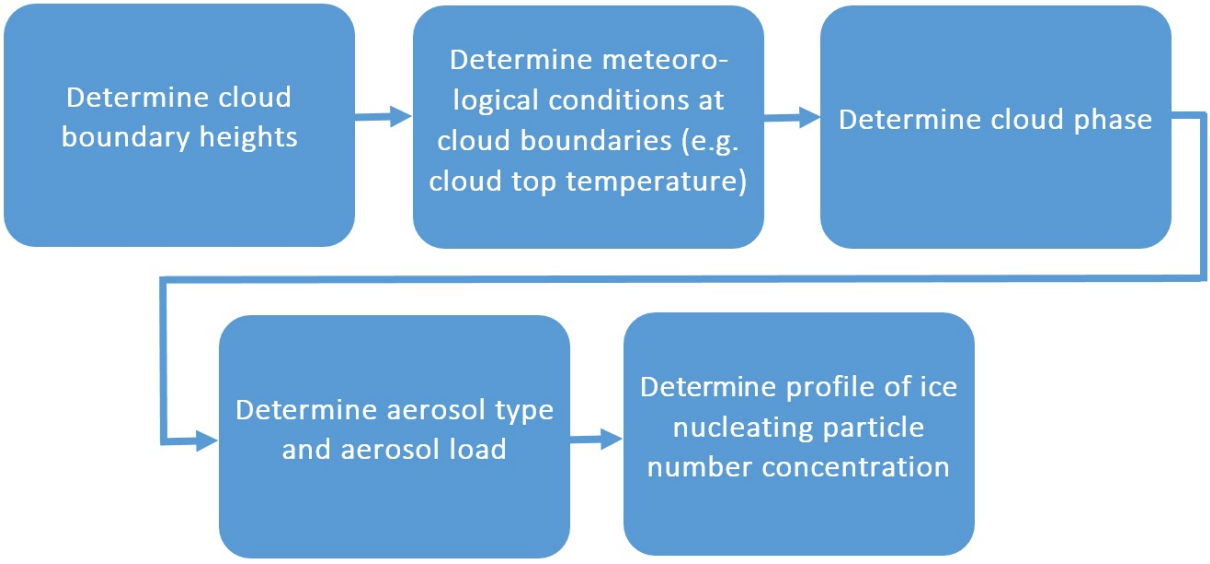

Figure 7: Schematic data analysis steps are shown beginning with the determination of cloud characteristics including the cloud boundaries, cloud-top temperature, and cloud phase. Furthermore, aerosol load and aerosol type need to be retrieved and transferred into ice nucleating particle number concentrations.

3.2 Raman and Klett method

In order to determine the particle backscatter coefficient and particle extinction coefficient of aerosol and cloud particles from equation 1 the most common methods are the Raman and the Klett method (Seifert, P., 2011).
For the Raman method it is necessary to detect the vibrational-rotational inelastic backscatter signal. The emitted laser pulse interacts with the molecules which can change their vibrational-rotational state after the scattering process. The difference corresponds to a specific energy change hence wavelength change of the scattering molecules which is 387 nm for the 355-nm inelastic backscatter, and 607 nm for the 532-nm inelastic backscatter. If a reference backscatter coefficient $\beta_{\mathrm{par}}(R_0, \lambda_0)$ for particles *par* at a specific height R_0 and the emitted wavelength λ_0 is known, the particle backscatter coefficient is given as:

$$\begin{aligned}\beta_{\mathrm{par}}(R, \lambda_0) = & \\ & - \beta_{\mathrm{mol}}(R, \lambda_0) + [\beta_{\mathrm{par}}(R_0, \lambda_0) + \beta_{\mathrm{mol}}(R_0, \lambda_0)] \\ & \cdot \frac{P(R_0, \lambda_{\mathrm{Ra}}) P(R, \lambda_0) N_{\mathrm{Ra}}(R)}{P(R_0, \lambda_0) P(R, \lambda_{\mathrm{Ra}}) N_{\mathrm{Ra}}(R_0)} \\ & \cdot \frac{exp(-\int_{R_0}^{R} (\alpha_{\mathrm{par}}(r, \lambda_{\mathrm{Ra}}) + \alpha_{\mathrm{mol}}(r, \lambda_{\mathrm{Ra}}))\mathrm{d}r)}{exp(-\int_{R_0}^{R} (\alpha_{\mathrm{par}}(r, \lambda_0) + \alpha_{\mathrm{mol}}(r, \lambda_0))\mathrm{d}r)}\end{aligned} \tag{2}$$

with the number concentration of Raman-scattering molecules N_{Ra}, the Raman wavelength λ_{Ra}, the index *mol* for molecules.
The Raman method is usually the most used method during night if Raman signals are available. Otherwise, or also during day when there is a lot of background noise due to the sunlight, the Klett method is used in order to retrieve the backscatter coefficient.
For the Klett method a particle lidar ratio S_{par} is assumed. The particle lidar ratio is the ratio of particle extinction and particle backscatter coefficient $S_{\mathrm{par}} = \frac{\alpha_{\mathrm{par}}}{\beta_{par}}$. An assumption for the particle lidar ratio can be done by taking usual lidar ratios for particles, cloud layers or aerosol-free situations, assuming it to be constant in height. Equation 1 can be solved for the particle backscatter coefficient.

3.3 Depolarization ratio

The depolarization ratio δ is the ratio of the cross-polarized component of the backscattered radiation $P_\perp$ to the parallel polarized radiation $P_\parallel$ (Engelmann et al., 2016):

$$\delta(R, \lambda) = \frac{P_\perp(R, \lambda)}{P_\parallel(R, \lambda)} \tag{3}$$

Initially, the laser emits parallel polarized electromagnetic waves. The atmospheric scatterers may change the degree of linear polarization. The depolarization ratio will therefore increase from single scattering events. The more nonspherical the particle shape is, the larger is the depolarization ratio. Specifically, the spherical water droplets have a depolarization ratio of 0 from single scattering, whereas randomly oriented nonspherical ice crystals have a depolarization ratio of 30-50% (Seifert, P., 2011). Another effect increasing the depolarization ratio is due to multiple scattering. In liquid water clouds the depolarization ratio usually increases with height due to the multiple scattering. This high depolarization ratio due to multiple scattering may complicate the classification between liquid water clouds and mixed-phase clouds. However, mixed-phase clouds usually

form ice virgae below cloud base whereas the depolarization ratio increases with height from the cloud base and upwards in liquid water clouds.
In older studies another complication of the classification of the cloud phase was due to specular reflection caused by horizontally aligned ice crystals for zenith pointing lasers (Seifert, P., 2011). This problem is no more relevant for the Polly^{XT} as it is tilted 5° off the zenith and has additionally a varying offset around 5° due to the movement of the ship.

3.4 Cloud boundary and cloud phase retrieval

In order to detect the cloud phase, first of all cloud layers need to be found. In Fig. 8 the particle backscatter coefficient at 532 nm is shown between 5800 m and 6800 m height for an arbitrary measurement. The classification can be done using thresholds. One way would be to define the cloud boundaries as the height at which the signal gradient of the backscatter coefficient β with height z is larger than a threshold value x as $|\frac{\mathrm{d}\beta}{\mathrm{d}z}| > x$. Seifert et al. (2010) identified the cloud-top height as the level above the signal maximum of the cloud where the backscatter signal is lower than the backscatter signal at cloud base. However, this is only possible if the lidar beam can penetrate through the whole cloud layer which is possible for an optical thickness lower than 3.
When determining the cloud phase, combinations of backscatter coefficients and depolarization ratios can be used. An example is shown in Fig. 9, which shows first data of the lidar measurements from PS116 on 24 November 2018, 1800 UTC to 2300 UTC. Starting from the clouds between 5 km and 8 km between 1900 UTC and 2000 UTC the backscatter coefficient is increased such that it is classified as a cloud layer. The depolarization ratio is high below the cloud base as an ice virga is formed. This cloud is classified as a mixed-phase cloud. The same holds for the clouds at the same height between 2130 UTC and 2230 UTC.
Between 2000 UTC and 2100 UTC the backscatter coefficient is high but the depolarization ratio is not increased and no ice virga is forming below cloud base, so it is classified as a pure liquid water cloud (small exception is a cloud at 7500 m around 2030 UTC). The cloud observed from 1900 UTC to 2130 UTC between 9 km and 12 km has a high depolarization ratio such as an ice virga but as the backscatter coefficient is quite low it is likely an ice cloud only.
Clouds that are relevant for the study should have a cloud-top temperature between 0°C and −38°C, the heterogeneous freezing temperature regime. The cloud-top information is retrieved from combined lidar measurements and radiosondes which are launched everyday before 1200 UTC.

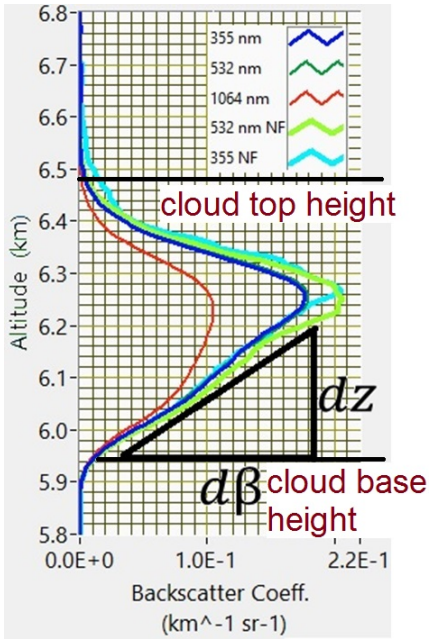

Figure 8: Classification of the boundary of cloud layers by using the signal gradient from lidar. Large signal gradients indicate cloud boundaries.

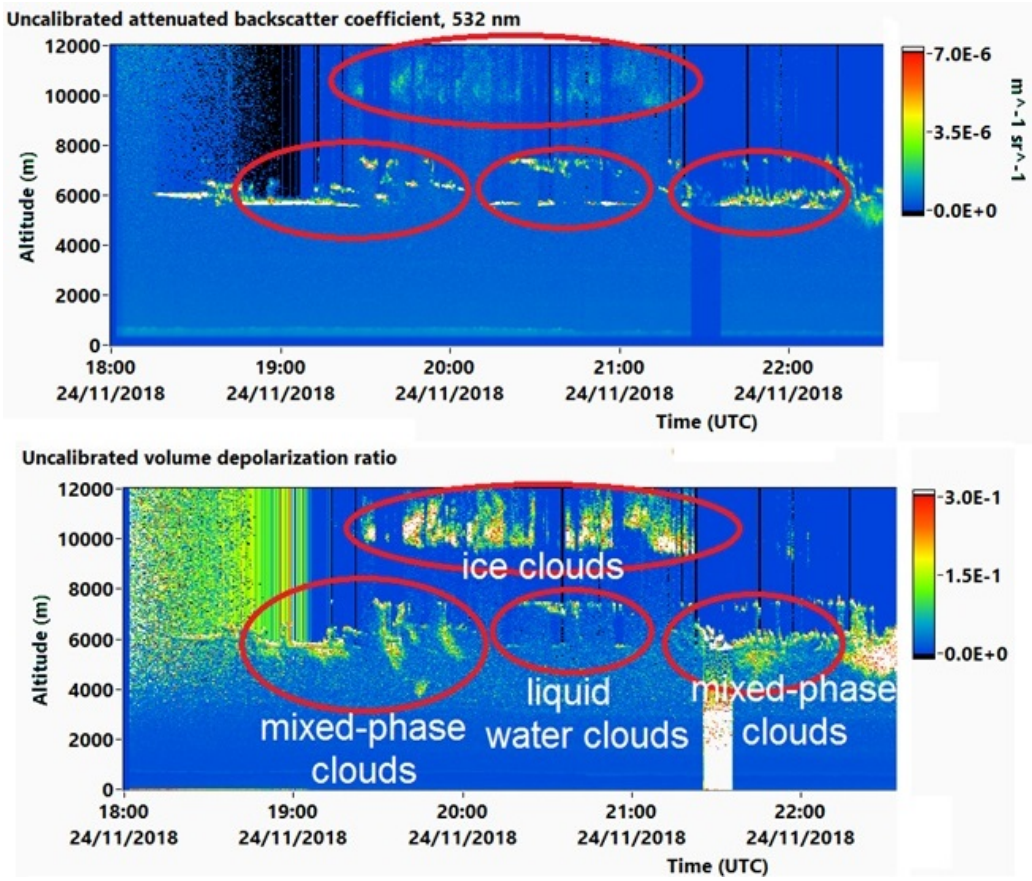

Figure 9: The cloud phase retrieval is done by combined backscatter coefficient and depolarization ratio measurements. High backscatter coefficient with low depolarization ratio indicates liquid water clouds. High backscatter coefficients and high depolarization ratio below cloud base (ice virga) indicates mixed-phase clouds. Lower backscatter coefficient and high depolarization ratio indicates ice clouds.

3.5 Aerosol characterization

An aerosol characterization can be achieved by combining lidar ratio measurements with particle depolarization ratio measurements (Illingworth et al., 2015). This is illustrated in Fig. 10. Typical values for lidar ratios are 20-35 sr for marine particles, 50-80 sr for mineral dust, 35-70 sr for urban particles, and 70-100 sr for biomass burning particles (see Tbl. 1). As there is an overlap of the lidar ratios for different aerosol types, the depolarization ratio is taken into account. The depolarization ratio is low for sea salt only slightly higher than 0%. For pollution and smoke the depolarization ratio is lower than 5%, for biomass burning aerosols usually around 10%. Higher depolarization ratios are reached for dust particles (10%-30%). The highest depolarization ratios are reached for aerosols from volcanic origin (30%-40%). With the combined measurement a classification is generally possible. If the classification is still unsure, the measurements can be combined with modeled backward trajectories to determine aerosol source regions.

Table 1: Lidar ratio [sr] and particle linear depolarization ratio [%] for most frequent aerosol types.

Aerosol type	Lidar ratio (sr)	Particle linear depolarization ratio (%)
Marine particles	20-35	0-5
Mineral dust	50-80	20-35
Urban particles	35-70	0-10
Biomass burning particles	70-100	0-10

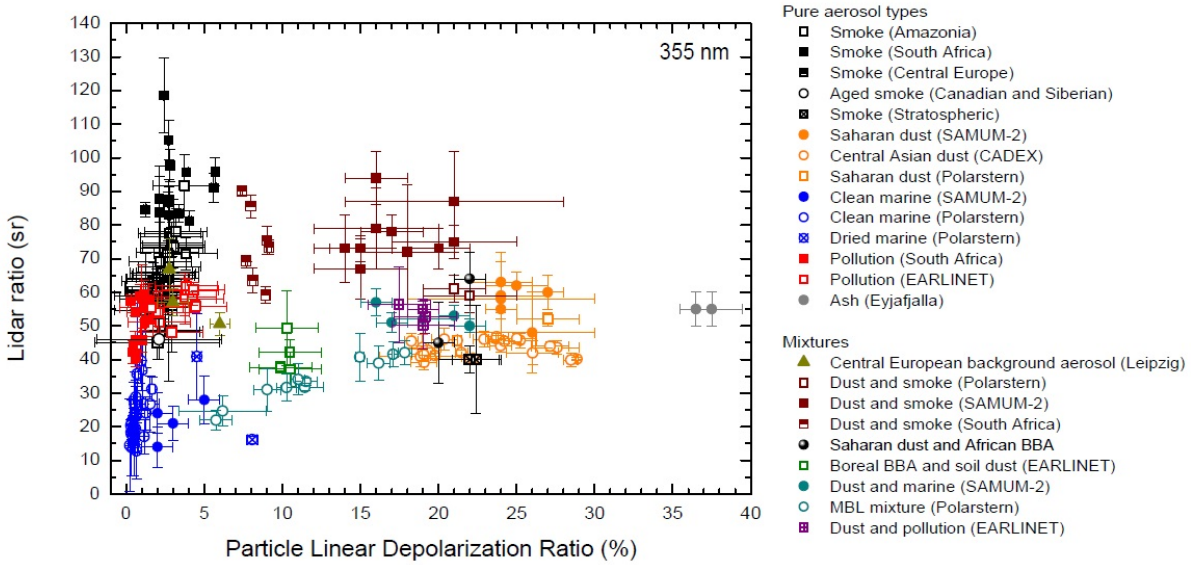

Figure 10: Scheme illustrating the relationship between aerosol types and lidar observables. By combining lidar ratio (absorbing properties) and depolarization ratio (non-sphericity) measurements it is possible to classify aerosol types (Floutsi, 2019).

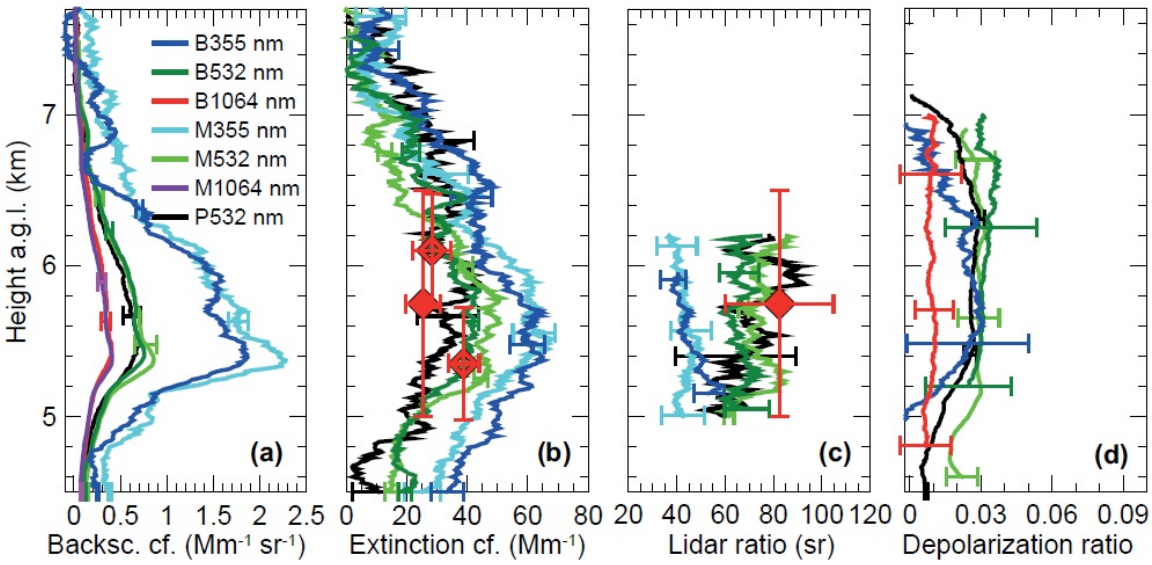

Figure 11: An example of a vertical profile of a tropospheric aerosol layer from Canadian wildfire smoke on 22 August 2017 is presented. The B (BERTHA, Backscatter Extinction lidar-Ratio Temperature Humidity profiling Apparatus), M (MARTHA, Multiwavelength Tropospheric Raman lidar for Temperature, Humidity and Aerosol profiling), and P (Polly^{XT}, Portable lidar system extended) indicate the different lidar types that were in use in Leipzig. The particle backscatter coefficient (a) shows increased values for the wavelengths 355 nm, 532 nm, and 1064 nm, as well as increased extinction coefficients (b). The resulting lidar ratios (c) (backscatter to extinction ratio) for the different wavelengths are different, but constant with height; approximately 40 sr for 355 nm, 70 sr for 532 nm, and 90 sr for 1064 nm. The depolarization ratio (d) is lower than 5% for all wavelengths. The error bars indicate the retrieval uncertainty (1 standard deviation). In the case of the 1064 nm extinction coefficient, a vertical profile could not be determined. Therefore, only a few values for retrieval window length (least-squares method) of 750 and 1500 m (indicated by vertical bars) are shown. The 1064 nm lidar ratio is given for the 1500 m retrieval interval length (Haarig et al., 2018).

Figure 11 shows vertical profiles of optical properties of a tropospheric aerosol layer. The enhanced backscatter and extinction coefficients indicate the height of the aerosol layer. Looking at the low depolarization ratio of less than 5% dust and volcanic ash can be excluded (compare to Fig. 10). The lidar ratios, especially the approximately 70 sr for 532 nm (comparing to Fig. 10) let smoke aerosols appear to be the prevailing aerosol type. Indeed, a smoke plume from intense Canadian wildfires (especially in British Columbia) reached Leipzig after traveling 7-10 days (Haarig et al. (2018)). This procedure shows how a classification into different aerosol types is principally done. Aerosol layers can be detected due to their enhanced extinction coefficient. Usually, the classification is done by using the particle linear depolarization ratio which helps to constrain the aerosol type. The further use of the lidar ratio helps to exclude further aerosol types. Usually, the aerosol type is quite certain then.
If the aerosol concentration is low, usually particle depolarization ratios can not be calculated. In this case, backward trajectories at the height of interest are useful in order to see the origin of the air including aerosols.

3.6 Retrieval of ice nucleating particle profiles from lidar measurements

In Fig. 12 the scheme of how to obtain the number of INP from lidar measurements is shown. The scheme was adapted from Mamouri and Ansmann (2016). As the number of INP is strongly dependent on the aerosol type the scheme includes the aerosol typing as the first instance. Using the particle linear depolarization ratio, the classification is done into marine, continental, or desert dust particles. These particles have a different linear depolarization ratio (Illingworth et al., 2015). However, this principle is only applicable for medium and higher aerosol concentrations as the particle linear depolarization ratio can usually not be calculated for low concentrations. In this case also backward trajectories can give a hint on the origin of the aerosol particles.
After the aerosol classification, the data analysis path in the scheme must consider the type of aerosol. From the lidar measurements the backscatter coefficient β is retrieved (see Section 3.2) and in the next step transferred into an extinction coefficient σ. This is done by using a typical aerosol-type-dependent lidar ratio S_{par} with $\sigma_{\mathrm{par}} = S_{\mathrm{par}}\beta_{\mathrm{par}}$. Typical continental aerosol lidar ratios are around 45 sr and for desert dust usually 55 sr (Illingworth et al. (2015)).
In the next step the extinction coefficient is converted into particle number concentrations by using a particle-type-dependent conversion factor. This factor is derived from an extended AERONET data analysis. AERONET is a worldwide network of photometers measuring the aerosol optical thickness at different wavelengths. From an angle-dependent all-sky scan of the wavelength-dependent sky radiance, scattering phase functions can be retrieved (Mamouri and Ansmann (2016), Shinozuka et al. (2015)). These are transferred into a volume-size distribution which can be transferred into a number-size distribution assuming spherical particles. The retrieved number size distribution is in a next step integrated for all sizes exceeding 500 nm in diameter to yield an estimate of the number concentration of potential ice-active aerosol particles, as this diameter threshold was also used by DeMott et al. (2010). For each size distribution, a corresponding value of the aerosol optical depth is provided by Aeronet. Based on the value pairs c_{250} and optical depth, a relationship between extinction and c_{250} can be derived. This ratio allows to convert lidar observations of aerosol extinction coefficient directly into c_{250}. Typical values are for example $c_{250,\mathrm{d}} = 0.20\,\mathrm{Mm\ cm^{-3}}$ for desert dust (when applying the procedure for Cape Verde and Barbados photometers at 532-nm wavelength for particles larger than 250 nm) or $c_{290,\mathrm{c}} = 0.09\,\mathrm{Mm\ cm^{-3}}$ for continental aerosol at Cyprus at 532 nm for particles larger than 290 nm. Applying the desert conversion factor $c_{250,\mathrm{d}}$ to the desert extinction coefficient σ_d will give the particle number concentration $n_{250,\mathrm{d,dry}} = c_{250,\mathrm{d}} \cdot \sigma_d$ and for the conversion factor $c_{290,\mathrm{c}}$ with the continental extinction coefficient σ_c the particle number concentration of $n_{290,\mathrm{c,dry}} = c_{290,\mathrm{c}} \cdot \sigma_{\mathrm{c}}$. Sea salt aerosols are not further accounted for as these are inefficient ice nucleating particles of around three orders of magnitude weaker than continental aerosol or desert dust (Mamouri and Ansmann, 2016).
As not every particle is efficient for forming an ice crystal, the number of particles need to be transferred into a measure which is directly relevant for the formation of ice in clouds. This measure is the number of ice nucleating particles n_{INP}. From the particle number concentration to the number of ice nucleating particles a particle-type-dependent parametrization (here meaning continental or desert dust particles) is applied. In a first step continental and desert dust particles are brought to surface level by using the factor $f = \frac{T_z p_0}{T_0 p_z}$ with the ambient temperature T_z and ambient pressure p_z as well as the standard temperature T_0=273.16 K and standard pressure p_0=101325 Pa.

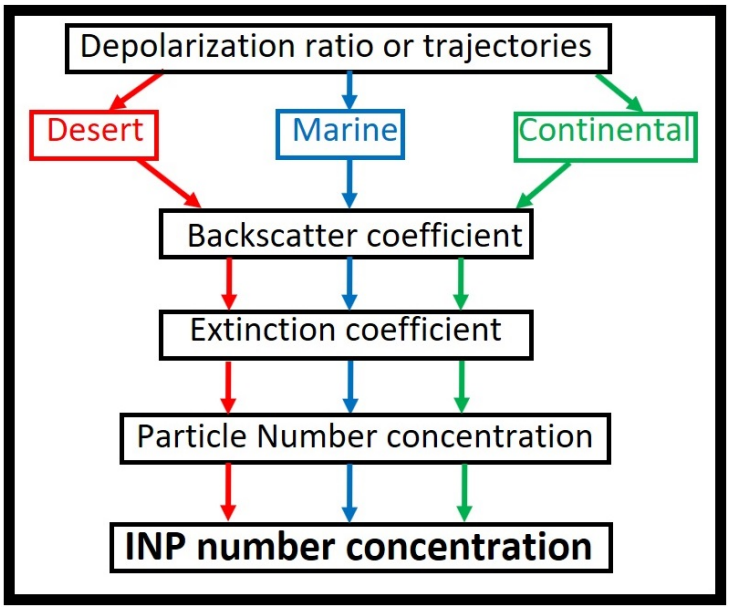

Figure 12: Scheme of the data analysis procedure for the INP retrieval. From depolarization ratios, backward trajectories, and Ångström exponents aerosol types are distinguished between desert and non-desert which is further distinguished into marine and continental. Aerosol-type-dependent particle backscatter coefficient profiles are transferred into aerosol-type-dependent particle extinction coefficient, which is transferred into an aerosol-type-dependent particle number concentration, such that in the end ice nucleating particle number concentration profiles can be determined for the different aerosol types from parametrizations (Mamouri and Ansmann (2016)).

$$n_{290,\mathrm{c}}(p_0, T_0) = f \cdot n_{290,c}(p_z, T_z) \tag{4}$$

$$n_{250,\mathrm{d}}(p_0, T_0) = f \cdot n_{250,\mathrm{d}}(p_z, T_z) \tag{5}$$

Now the aerosol-type-dependent parametrization is applied. The following parametrization is used for continental aerosols:

$$n_{\mathrm{INP,c}}(p_0, T_0, T_z) = a_1 \cdot (273.16 - T_z)^{b_1} \cdot n_{250,\mathrm{c,dry}}(p_0, T_0)^{[c_1 \cdot (273.16 - T_z) + d_1]} \tag{6}$$

with the constants derived from field campaigns $a_1 = 0.0000594$, $b_1 = 3.33$, $c_1 = 0.0265$, and $d_1 = 0.0033$. After multiplying with the factor $\frac{T_0 p_z}{T_z p_0}$ the $n_{\mathrm{INP,c}}(p_0, T_0)$ is transferred into the vertical ice nucleating particle number concentration profile $n_{\mathrm{INP,c}}(p_z, T_z)$.
In case of the desert particles the following parametrization is used:

$$n_{\mathrm{INP,d}}(p_0, T_0, T_z) = f_d \cdot n_{250,\mathrm{d,dry}}(p_0, T_0)^{[a_2 \cdot (273.16 - T_z) + b_2]} \cdot exp[c_2(273.16 - T_z) + d_2] \tag{7}$$

with $f_d = 3$, $a_2 = 0.0$, $b_2 = 1.25$, $c_2 = 0.46$, and $d_2 = -11.6$.
After multiplying with $\frac{T_z p_0}{T_0 p_z}$ again $n_{\mathrm{INP,d}}(p_0, T_0)$ is transferred to $n_{\mathrm{INP,d}}(p_z, T_z)$ for desert aerosols.
Finally, the number concentrations of ice nucleating particles n_{INP} are derived from lidar measurements. The uncertainty is in the range of one order of magnitude. A typical INP concentration during the RV Polarstern cruise PS116 would be $0.1\,\mathrm{L}^{-1}$ for continental aerosols at $-20°\mathrm{C}$ and a backscatter coefficient of $1 \cdot 10^{-2}\,\mathrm{Mm}^{-1}\mathrm{sr}^{-1}$.

3.7 Retrieval of ice nucleating particle profiles from MACC model

In former studies usually models were used in order to retrieve the number of INP. Therefore, a comparison between the retrieved number of INP from measurements and from a model is done. MACC (Monitoring Atmospheric Composition and Climate, ECMWF (2019a)) provides information on the global aerosol distribution in the atmospheric layers. MACC is co-ordinated by ECMWF (European Centre for Medium-Range Weather Forecasts) and superseded by CAMS (Copernicus Atmosphere Monitoring Service). The MACC model gives information on 4 different aerosol types. These are sea salt aerosols in different diameters (0.03 - 0.5 µm, 0.5 - 5 µm, and 5 - 20 µm), dust aerosols (0.03 - 0.55 µm, 0.55 - 0.9 µm, and 0.9 - 20 µm), hydrophilic organic matter, hydrophobic organic matter, hydrophilic black carbon, hydrophobic black carbon, and sulphate aerosols. All aerosol information is provided as a mixing ratio in kg kg^{-1}. The MACC model has a temporal resolution of three hours, spatial resolution of 0.75°x0.75° as latitude and longitude, and is structured into 137 model levels vertically. These 137 model levels can directly be transferred into pressure and height levels with a table at ECMWF (2019b). Each model level belongs to a fixed pressure level. If there is radiosonde data available, the pressure level can be transferred into a height level with the barometric height formula. Otherwise, the table in ECMWF (2019b) also delivers the information on the geopotential and geometric altitude for a standard atmosphere. In this case no calculation needs to be done - model levels can directly be transferred into pressure or height levels. The distance between two model levels is smaller close to the surface and increases in higher altitudes. The highest model level is at approximately 70,000 m (depending on the pressure distribution). All model levels contain the mentioned aerosol information as well as temperature information for every grid point at every certain time.

As the aerosol information as a model output is given as a mixing ratio in kg kg^{-1}, it needs to be transferred into aerosol densities in µg m^{-3}, equivalent particle backscatter coefficients $\beta_{\mathrm{par,eq}}$ in Mm^{-1} sr^{-1}, and into INP number concentrations in L^{-1} in order to make the numbers comparable to the lidar retrieved aerosol properties.

The conversion from mixing ratios into aerosol densities is done by applying the ideal gas law.

$$\rho_{\mathrm{aer}} = \rho_{\mathrm{aer,conv}} \frac{p}{RT} \tag{8}$$

with $\rho_{\mathrm{aer,conv}}$ as the aerosol load (from the MACC model) in kg kg^{-1} being converted into the aerosol density ρ_{aer} in µg m^{-3}. R is the gas constant, p is the atmospheric pressure, and T the atmospheric temperature. As there are no radiosonde launches at every grid point, the temperature from the MACC model is used for all model levels.

In a next step the aerosol concentration is converted into an equivalent backscatter coefficient. For this the parametrization in Mamouri and Ansmann (2017) is used. The equivalent particle backscatter coefficient $\beta\mathrm{par, eq}$ at 532 nm is:

$$\beta\mathrm{par, eq} = \frac{M_{\mathrm{par}}}{\rho_{\mathrm{par}} c_{\mathrm{v,par}} S_{\mathrm{par}}} \tag{9}$$

with the mass concentration M_{par}, the particle density ρ_{par}, the extinction-to-volume conversion factor $c_{\mathrm{v,par}}$, and the lidar ratio S_{par}. All of these are particle-type-dependent and can be found in Mamouri and Ansmann (2017).

In the last step the equivalent particle backscatter coefficient is used in order to retrieve the number of INP in the same way as presented in Section 3.6.

4 Remote-sensing of the relationship between aerosol properties and heterogeneous ice formation at TROPOS

In former studies usually proxies like models were used in order to determine the aerosol load (Seifert, P., 2011). The load of aerosols within a vertical column is of minor relevance though. It is important to obtain the aerosol concentration at the height in which the clouds occur. In the following Section studies from TROPOS (Leibniz Institute for Tropospheric Research) are presented showing the fraction of ice-containing clouds for different cloud-top temperatures depending on dust load, region, and season. These studies relate aerosol properties to cloud characteristics. However, a direct relationship to measurements of aerosol properties is not shown.

4.1 Fraction of ice-containing clouds depending on seasons

The aerosol concentration at the height where the clouds occur or rather the efficiency of the aerosols to form ice heterogeneously in clouds regionally also varies with season. This aspect as well as the impact for heterogeneous freezing in clouds is studied in Seifert et al. (2015) for the region of the Amazonian tropical rainforest. Figure 13 shows the fraction of ice-containing clouds in the Brazilian Amazon. During the dry season, the fraction of ice-containing clouds was found to be up to two times larger than during the wet season (Seifert et al., 2015). Looking at the MACC-modeled (Copernicus, 2019) aerosol load in Fig. 14 also the aerosol load seems to be enhanced during the dry season by a factor of 2 to 10. Especially hydrophobic organic matter as well as coarse dust appeared to occur in higher loads during the dry season. The higher amount of ice nucleating particles may be related to the increased fraction of ice-containing clouds.

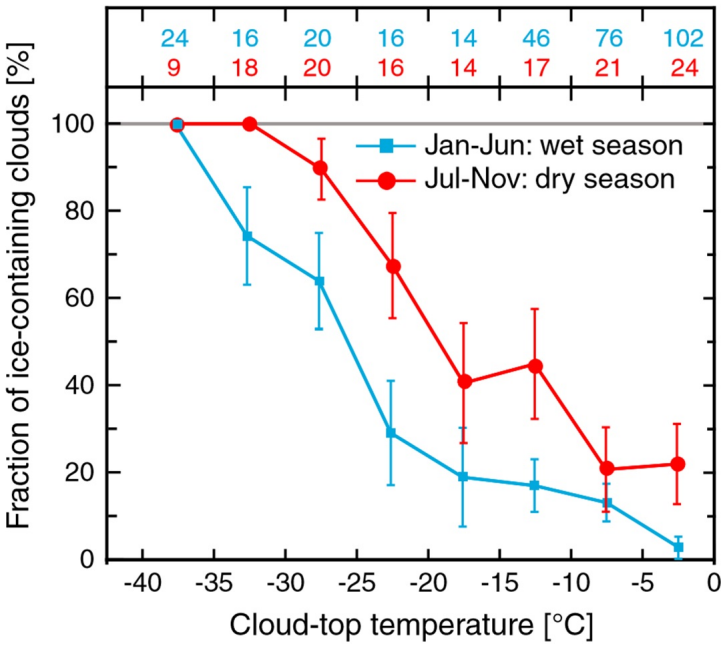

Figure 13: The fractions of ice-containing clouds as a function of cloud-top temperature in the wet and dry season, respectively, in the Brazilian Amazon are shown. There is a larger fraction of ice-containing clouds during the dry season possibly due to an increased amount of aerosols released by biomass burning activities (Seifert et al., 2015).

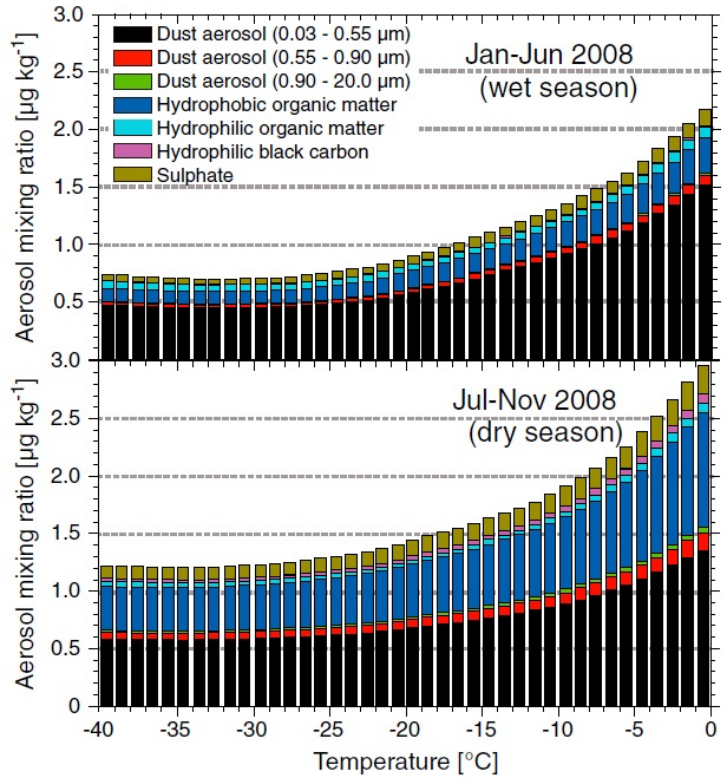

Figure 14: Monitoring Atmospheric Composition and Climate (MACC) model simulation of the aerosol load of dust, organic matter, black carbon, and sulphate during the wet season (top) and dry season (bottom) (Seifert et al., 2015).

4.2 Fraction of ice-containing clouds depending on geographical regions

As it was shown in Fig. 4 the fraction of ice-containing clouds is quite different for different regions on Earth. The cloud-top temperatures are in the heterogeneous freezing temperature regime. It was speculated and shown that differences of aerosol type and aerosol load influence the glaciation of clouds. The more aerosol-polluted northern hemispheric stations of Leipzig and PASCAL were found to have a higher fraction of ice-containing clouds than the north-south cross-section of the Atlantic ocean and especially the southern hemispheric stations of Punta Arenas and Stellenbosch. The low fraction of ice-containing clouds found above Cape Verde is surprising as the total aerosol load is usually high at this site. There, frequently dust plumes emitted from the Saharan desert travel westwards due to the prevailing easterly wind, such that large amounts of dust regularly pass Cape Verde. Furthermore, dust particles are known to be efficient ice nucleating particles (Hoose and Möhler, 2012). It is thus worth considering the vertical distribution of the aerosol load. With respect to the time period from which the Cape Verde cloud statistics (Ansmann et al., 2009) were derived, the vertical distribution of the dust mass concentration as simulated with the Dust Regional Atmospheric Model DREAM (Nickovic et al. (2001)) is shown in Fig. 15 as shown by Seifert, P. (2011). The white vertical bars indicate the classified cloud cases used in the Cape Verde statistics shown in Fig. 4. The black line indicates the isoline of the $2\,\mu g\,m^{-3}$ which was the threshold to dust-laden situations used in Seifert et al. (2010) see Section 4.3. This means that no classified cloud case would be situated in an aerosol-laden time and height period compared to Seifert et al. (2010). The highest dust concentrations seemed to occur in the surface-near regions between 0 km and 4 km. This is the region where mixed-phase clouds do not occur as the temperature is usually above 0°C. In the relevant region for heterogeneous freezing between 4 km and 10 km where the majority of the clouds was identified, the dust concentration was found to be lower and the dust-laden threshold of Seifert, P. (2011) was not reached.
The study shows that it is important to have aerosol information dependent on the height. Here, the profiles of aerosols were determined from DREAM simulations.

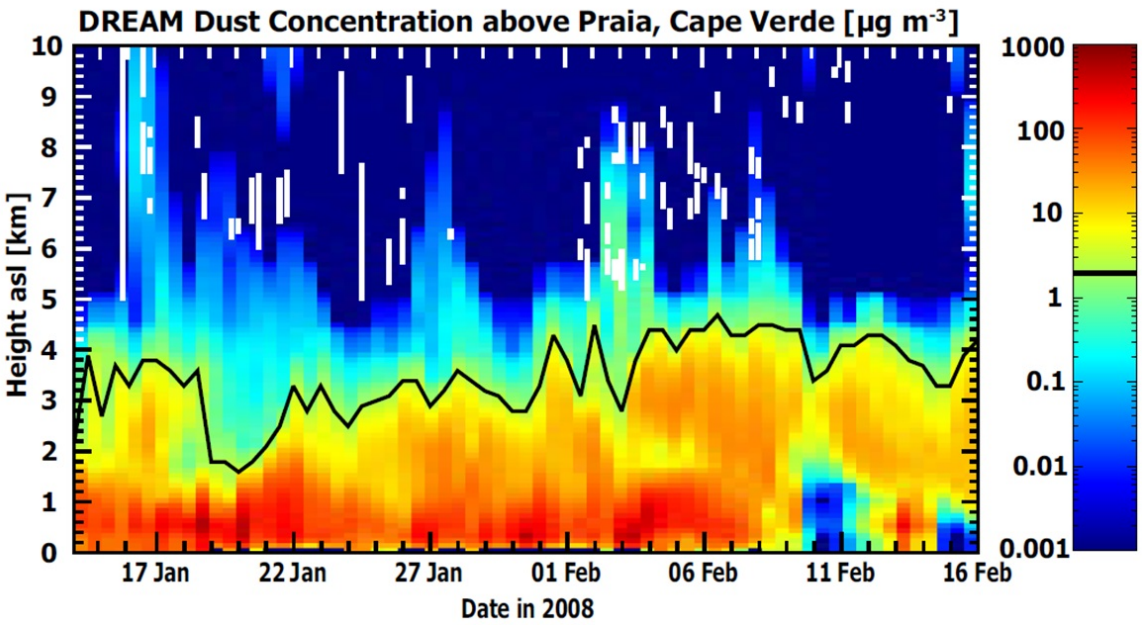

Figure 15: A DREAM model study shows the temporal evolution of the vertically resolved dust concentration for Cape Verde. Aerosols are not necessarily abundant at the height where clouds are forming. Dust concentrations are shown in $\mu g\,m^{-3}$. The white vertical bars indicate the classified cloud cases. The black line indicates a $2\,\mu g\,m^{-3}$ threshold (Seifert, P., 2011).

4.3 Co-located observations of microphysical properties of mixed-phase clouds and aerosol

As was shown in the previous section, vertical information about the aerosol distribution is a key prerequisite in order to put heterogeneous ice formation and aerosol load in relation. When information about the clouds, meaning cloud-top temperature and thermodynamic cloud phase are retrieved as demonstrated in Fig. 7, statistics can be developed. Recently, existing studies also take the aerosol properties into account, retrieving aerosol properties, however from models only (Seifert et al., 2010).
Figure 16 shows a lidar data set produced in Leipzig separated into dust-laden ($\geq 2\,\mu g\,m^{-3}$) and dust-free ($< 0.001\,\mu g\,m^{-3}$) situations by using the DREAM Seifert et al. (2010)). The fraction of ice-containing clouds appears to be increased for the dust-laden cases by up to 30% absolute difference. This also means that ice formation in clouds already seems to start at higher temperatures in the dust-laden case over Leipzig.

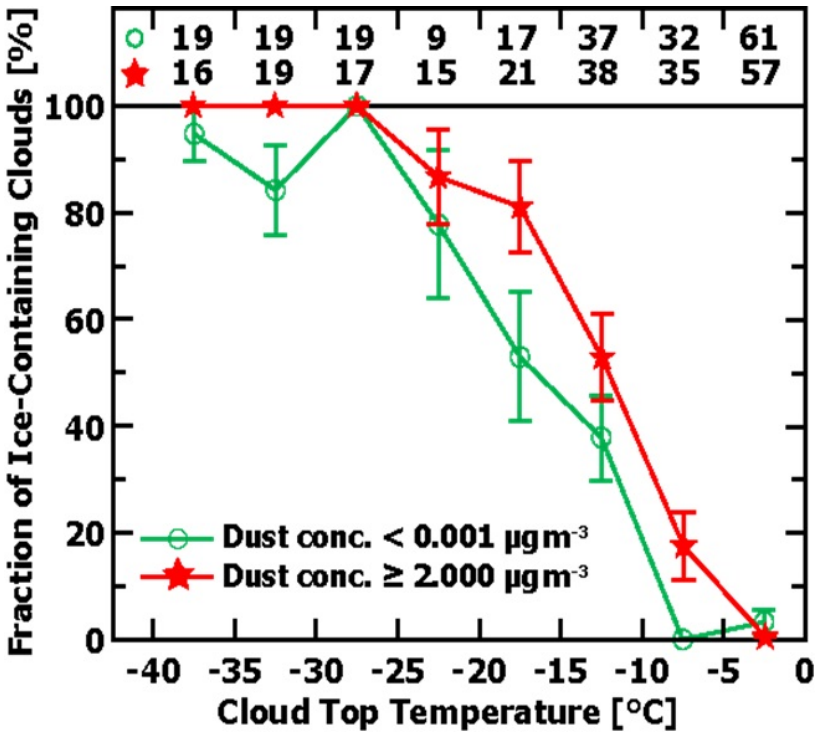

Figure 16: By using the Dust Regional Atmospheric Model DREAM the data set of Leipzig was separated into dust-free and dust-laden cases. The fraction of ice-containing clouds was found to be larger in dusty (red) situations than in dust-free situations (green). For the whole study more than 2300 cloud cases observed between February 1997 and June 2008 were analyzed (Seifert et al., 2010).

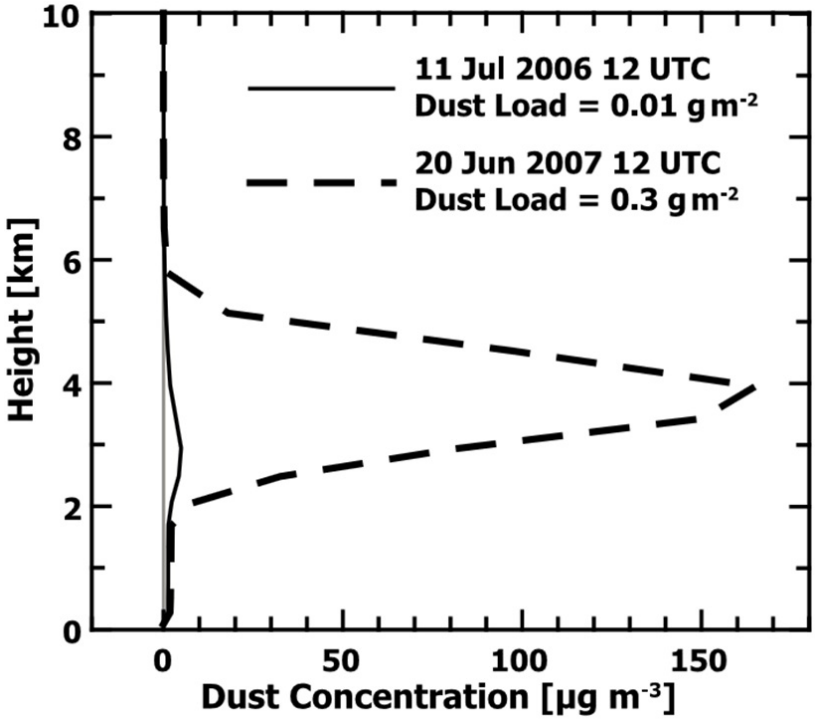

Figure 17: A comparison of DREAM-model-simulated aerosol load on 11 July 2006 and 20 June 2007 for an aerosol-cloud interaction study. There were more than an order of magnitude larger dust concentrations observed on 20 June 2007 between 2 km and 6 km height (Seifert et al., 2010).

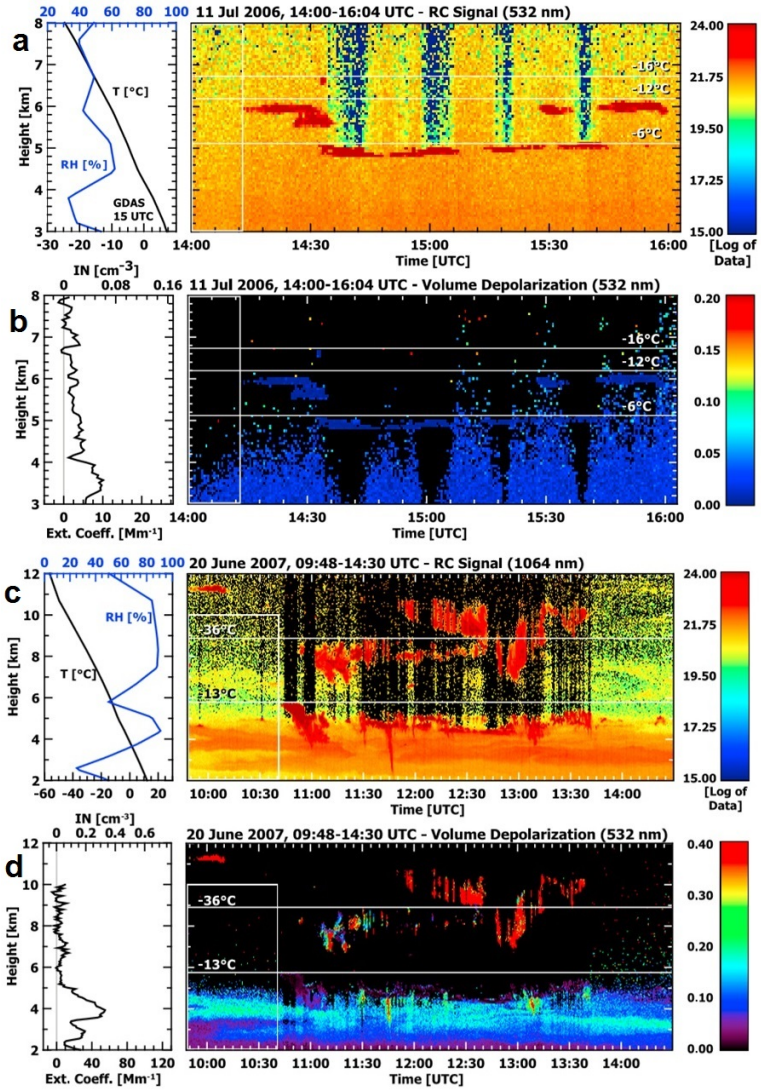

Figure 18: The cloud phase distribution in a dust-free a) and b) and dust-laden c) and d) situation is shown. a) and c) show the range-corrected signal at 532 nm and the temperature and relative humidity height profiles for 11 July 2006 and 20 June 2007, respectively. b) and d) show the volume depolarization ratio at 532 nm and the profiles of ice nucleating particles for 11 July 2006 and 20 June 2007, respectively. In the dust-free situation lower temperatures are needed in order to glaciate the cloud. Model information is used to retrieve aerosol information (see Fig. 17) (Seifert et al., 2010).

Figure 17 shows a comparison of the aerosol load on 11 July 2006 and 20 June 2007. The profiles of the dust concentrations are simulated by the DREAM model. The two examples are chosen as a nearly dust-free situation in 2006 and a dust-laden situation in the 2007 case. The aerosol load was found to be larger by more than an order of magnitude in 2007. In Fig. 18 both situations are compared in terms of cloud phase depending on the cloud-top temperature. In the case of the aerosol-free situation the clouds at $-6°C$, $-12°C$, and $-16°C$ cloud-top temperature do not show signs of ice formation. The backscatter coefficient was enhanced whereas the depolarization ratio was low. Regarding to Section 3.3 the observed cloud layers were classified as a pure liquid water cloud. In the case of the aerosol-laden atmosphere the clouds formed ice regarding to the cloud phase classification mentioned in Section 3.4 at $-13°C$ and $-36°C$ cloud-top temperature. As $-36°C$ is much lower than the temperatures in the dust-free situations, it is not surprising that this cloud contained ice. However, the cloud at $-13°C$ at approximately

6 km height contained ice in the aerosol-laden situation only (aerosols between 2 km and 6 km regarding to Fig. 17) whereas the clouds at similar temperatures in the aerosol-free situation did not contain ice. Obviously, this was only a case study which is not relevant for statistics, nevertheless, this example shows how the theoretically expected dependence between aerosols in the atmosphere and ice in clouds works.

5 Preparatory studies for applying the new approach relating aerosols and clouds

Before actual studies can be conducted it needs to be discussed what information is necessary to be retrieved from aerosol layers as well as from the supercooled clouds. One way of relating the properties of aerosol layers to the properties of supercooled clouds is to relate the number of INP to the thermodynamic phase of the clouds. However, this relation gives an incomplete answer only. Therefore, the question of how many ice crystals do form in dependence on the availability of ice nucleating particles arises. In the new study of Ansmann et al. (2019b), a relationship between ice-nucleating particle concentration and ice crystal number concentration in altocumulus and cirrus layers is presented based on ground-based active remote sensing with Raman polarization and Doppler lidar only. It was found that the ice crystal number concentration ranged from 0.1–10 L^{-1} in the altocumulus layers and 1-50 L^{-1} in the cirrus layers observed between 8–11 km height.
As there was no Doppler cloud radar nor a Doppler lidar available during the RV Polarstern cruise PS116, this Master's thesis can not reproduce the study of Ansmann et al. (2019b) completely. It therefore shows an overview of the relationship between the availability of ice nucleating particles and the thermodynamic phase of supercooled clouds only.
This Section shows an overview of the route of cruise PS116 of RV Polarstern from Bremerhaven to Cape Town in order to get knowledge about the latitudinal and longitudinal regions RV Polarstern crossed. Furthermore, an overview of the optical properties during the whole cruise is shown as well as the MACC-modeled aerosol concentration during the cruise as this shows the whole range of possible case studies. For the ensurance of the data quality, a MACC model temperature profile is compared to a radiosonde temperature profile, a standard reference backscatter coefficient is retrieved and different INP parametrizations are compared.

5.1 Overview of the route, cloud characteristics, and aerosol conditions during the RV Polarstern cruise

Figure 19 shows the track of the RV Polarstern cruise PS116. Each blue diamond indicates the daily noon position of the ship. The cruise started on 10 November 2018 in Bremerhaven (Germany) and ended on 11 December 2018 in Cape Town (Republic of South Africa). After the first week, RV Polarstern reached Las Palmas de Gran Canaria (Spain) where it was in the harbor for five days. After another four days RV Polarstern passed the region between Cape Verde and western continental Africa where the zone of highest Saharan dust concentrations was found. Afterward, the equator was crossed on 28 November 2018. From the equator it took another 13 days to reach Cape Town on 11 December 2018.

Figure 20 shows an overview of measured optical properties over the whole measurement period. Figure 20a shows the time-height cross-section of the range-corrected signal at 532-nm wavelength, Fig. 20b shows the volume depolarization ratio for the same time-height cross-section. The chosen scales enable to focus on the low clouds in Fig. 20a, and Fig. 20b enables to visualize the higher cirrus clouds.
The missing data from 17 to 22 of November 2018 (black period in Fig. 20) is due to the missing measurement permission in the harbor of Las Palmas de Gran Canaria during that time. In the last part of the cruise the Sun was close to the zenith during noon, so the measurements had to be stopped for several hours around noon in order to prevent

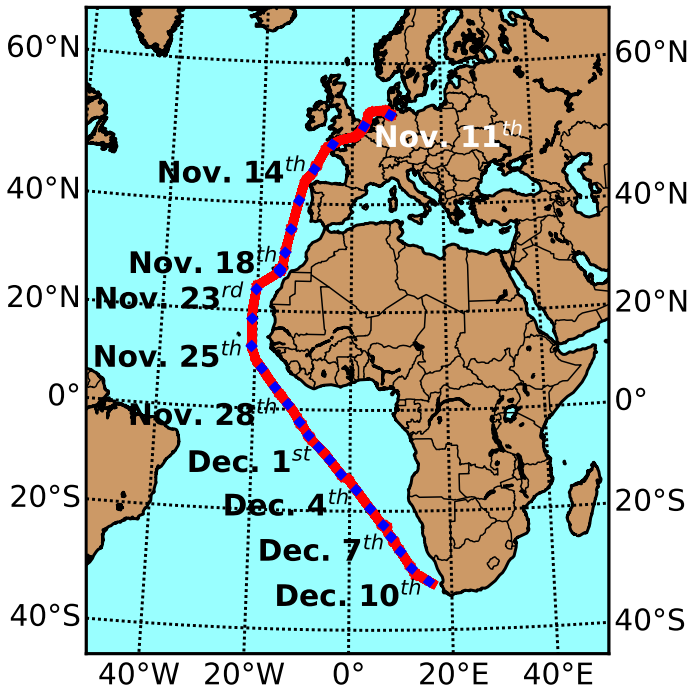

Figure 19: The track of the RV Polarstern cruise PS116 started in Bremerhaven (Germany), crossed Las Palmas de Gran Canaria (Spain) and ended in Cape Town (Republic of South Africa). It started on 10 November 2018 and ended on 11 December 2018.

damage on the photon detectors by direct sunlight.
It can be seen, that especially in November 2018 cirrus clouds occurred quite frequently, sometimes embedded in frontal systems. Also low clouds occurred from time to time, whereas middle-high clouds between 3 and 7 km occurred less frequently. Furthermore, the increased volume depolarization ratio from the surface up to 3 km height between 25 and 28 of November 2018 can be interpreted as a Saharan dust plume. December 2018 (southern hemisphere) had totally different characteristics in terms of clouds. High clouds and middle-high clouds were almost absent, whereas low clouds like stratus or stratocumulus with a base lower than 1 km and 1-2 km thickness occurred at a large percentage of the time. With respect to the climatological mean, this is an expected result. The large region in the west of Namibia has the highest probability worldwide to form stratocumulus clouds due to the cold ocean current stabilizing the air (Wood, 2012). However, due to this phenomenon, middle-high clouds in a temperature range between 0 and −38°C were not detected in December 2018 and therefore data measured in December 2018 is unfortunately not applied for the determination of the direct influence of aerosols on heterogeneous freezing.

Figure 21 shows an overview over the modeled (MACC model; see Section 3.7) concentrations of different aerosol types in µg m^{-3} during the whole cruise. Figure 21a shows the total aerosol concentration of all aerosol types. Close to the surface the aerosol concentrations reach values up to 10 µg m^{-3}. In the heights where aerosols may be relevant as ice nucleating particles for heterogeneous freezing between 0 and −38°C (indicated by the black horizontal lines) the aerosol concentrations were usually in the order of 10^{-2} µg m^{-3}, and in maximum up to $2 \cdot 10^{-1}$µg m^{-3}. Even this value is one order of magnitude lower than what was classified as dust-laden in (Seifert et al. (2010)).
Looking into more detail of the aerosol types, Fig. 21b shows a similar structure as the total aerosol concentration which indicates that the most contributing aerosol type to

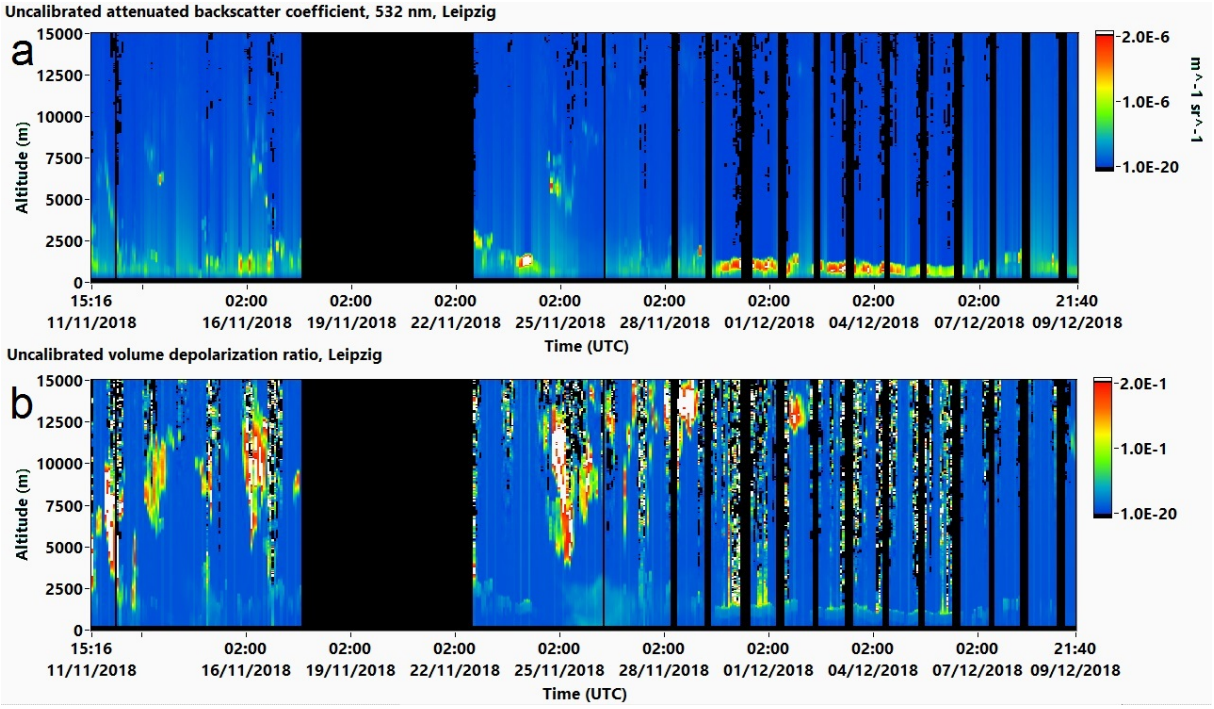

Figure 20: An overview of optical properties over the whole measurement period from PS116 is shown. a) shows an overview of the 532-nm range-corrected signal, b) shows the volume depolarization ratio. Due to the chosen scales a) focuses on the low clouds, and b) enables to see the higher cirrus clouds.

the total aerosol concentration are sea salt particles which are known as inefficient ice nucleating particles.

The concentration of dust aerosols is shown in Fig. 21c. Here, two events can be separated. The first dust event occurred on 15 November 2018 when RV Polarstern was in the west of the coast of Portugal reaching heights of up to 8 km. The second event occurred between 24 and 27 of November 2018 which was close to Cape Verde. At heights where the temperatures were between 0 and -38°C concentrations were only up to 10^{-1} µg m^{-3}. Both dust events were linked to Saharan dust outbreaks as trajectories indicate.

The aerosol mass concentrations of the remaining aerosol types (organics, black carbon, sulphates) are presented in Fig. 21d. Concentrations were always lower than 10^{-1} µg m^{-3}. Generally, the concentrations of these aerosol types were slightly higher close to the tropics and in the southern hemisphere. This may be linked to biomass burning activities in the tropical rainforests.

All in all, the modeled aerosol concentrations give a good hint on the classification into rather aerosol-free and aerosol-laden situations.

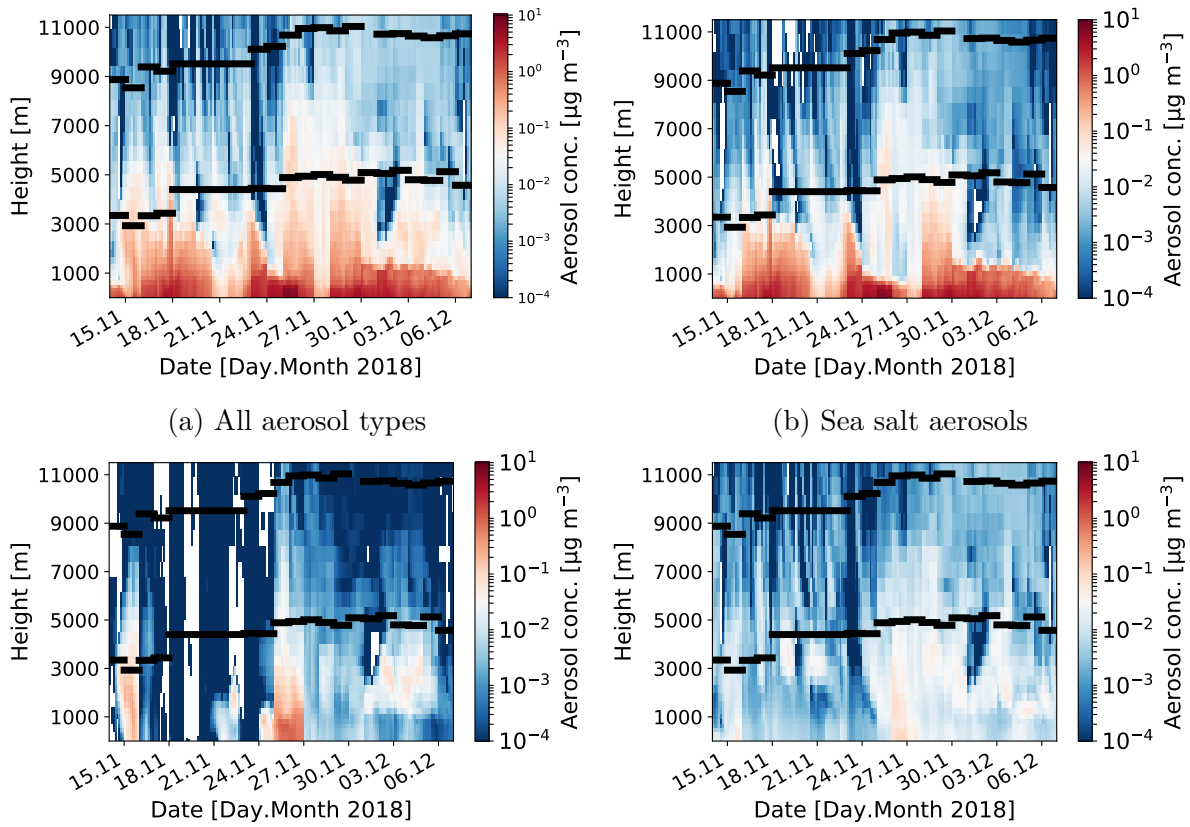

(a) All aerosol types

(b) Sea salt aerosols

(c) Dust aerosols

(d) Organics, black carbon, or sulphates

Figure 21: Overview over the aerosol concentration of different aerosol types during the RV Polarstern cruise simulated with MACC for the time period from 14 November 2018 to 7 December 2018. The lower and upper black contours indicate the 0°C and −38°C isotherms, respectively, as derived from the daily radiosonde launches (data from ECMWF (2019a)).

5.2 Comparison of the vertical temperature profile of MACC and radiosonde

The MACC model provides information on the aerosol mixing ratio in units of kg kg^{-1}. In order to retrieve the concentrations in µg m^{-3} the ideal gas law needs to be applied. With the aerosol density $\rho_{\text{aer}} = \rho_{\text{aer,conv}} \frac{p}{RT}$ ($\rho_{\text{aer,conv}}$ is the aerosol load from the MACC model in kg kg^{-1}) the conversion into the aerosol density in µg m^{-3} can be realized. R is the gas constant, p is the atmospheric pressure, and T the atmospheric temperature. As there are no radiosonde launches at every grid point, the temperature from the MACC model is used for all model levels. Therefore, a quality check is done. For this, a radiosonde temperature profile is compared to the model temperature profile. A pressure comparison will not be done because the pressure heights are linked to the model levels.
Figure 22 shows the mentioned temperature comparison between MACC and the radiosonde. The radiosonde was launched on 25 November 2018 at 1200 UTC (13.08°N, 20.83°W), MACC-data is from 25 November 2018 at 1200 UTC (13.25°N, 20.50°W). Below 2000 m height, the difference between model and measurement reaches up to 10 K. This seems to be a result of a strong temperature inversion which is poorly represented in the model simulations. However, the height region of interest from approximately 3 km to 10 km (temperature range of 0 to −38°C) shows a temperature uncertainty of less than 3 K which is approximately 1% at 250 K. So the conversion from aerosol load in kg kg^{-1}

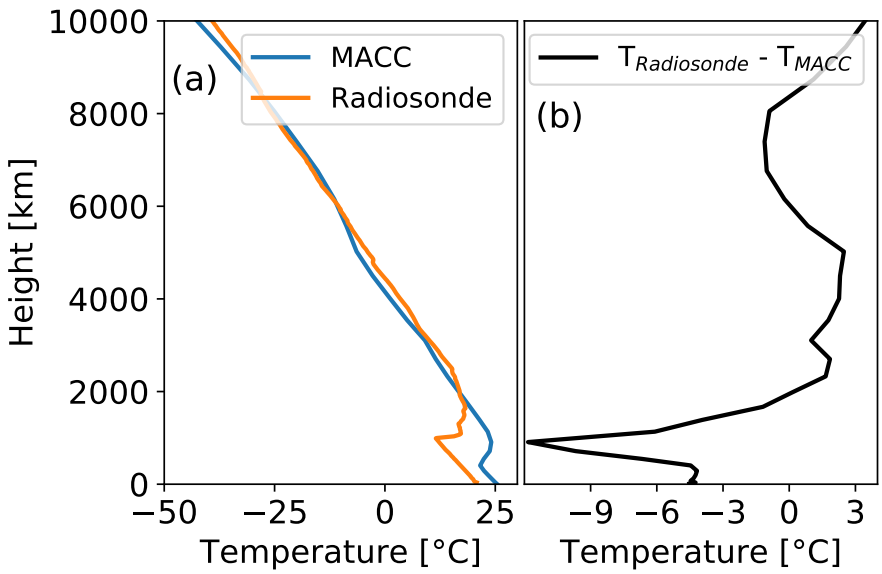

Figure 22: Comparison of the temperature profiles measured by a radiosonde and simulated by MACC. The radiosonde was launched on 25 November 2018 at 1200 UTC (13.08°N, 20.83°W), MACC-data is from 25 November 2018 at 1200 UTC (13.25°N, 20.50°W).

into aerosol concentration in µg m^{-3} is quite certain.

5.3 Retrieval of a standard reference backscatter coefficient

The atmospheric backscatter coefficient profile is influenced by molecules, aerosols, and clouds (Weitkamp, 2005). Assuming a cloud-free atmosphere, only molecules and aerosols scatter radiation backward at 180°. The scattering properties of molecules can explicitly be calculated by knowing pressure and temperature (from radiosondes) in the specific height. The aerosol concentration can vary strongly, however, from a certain height of usually 5 km and upwards high aerosol concentrations are rare. Nevertheless, there is usually a typical "background" aerosol concentration. This is assumed to be fairly constant in height. It adds to the molecular scattering. The value is called the reference backscatter coefficient and its magnitude is determined from the following representative case study.

Figure 23a shows the range-corrected signal at 1064 nm in a) and the volume depolarization ratio at 532 nm in b). It includes a surface-near Saharan dust layer up to 3 km height, an aerosol background conditioned region between at least 4 to 7 km height, and a cirrus cloud from 8 to 12 km height. The radiosonde temperature profile in Fig. 23b shows temperatures down to −50°C at cloud-top as well as temperatures between 0 and 25°C in the Saharan dust layer.

It is known, that in a cirrus cloud the particle linear depolarization ratio is between 40% and 60%, usually being close to 50% (Urbanek et al., 2018). Saharan dust should have a particle linear depolarization ratio of around 30% (Illingworth et al., 2015). By adjusting the reference backscatter coefficient, it can be determined which value leads to the most reasonable results (Seifert et al., 2007).

For retrieving the particle linear depolarization ratio of the cloud and the Saharan dust layer with the Klett method, first of all the lidar ratio of the cloud needs to be determined as a preparatory study. This is demonstrated in Fig. 24. For the cirrus cloud retrieval

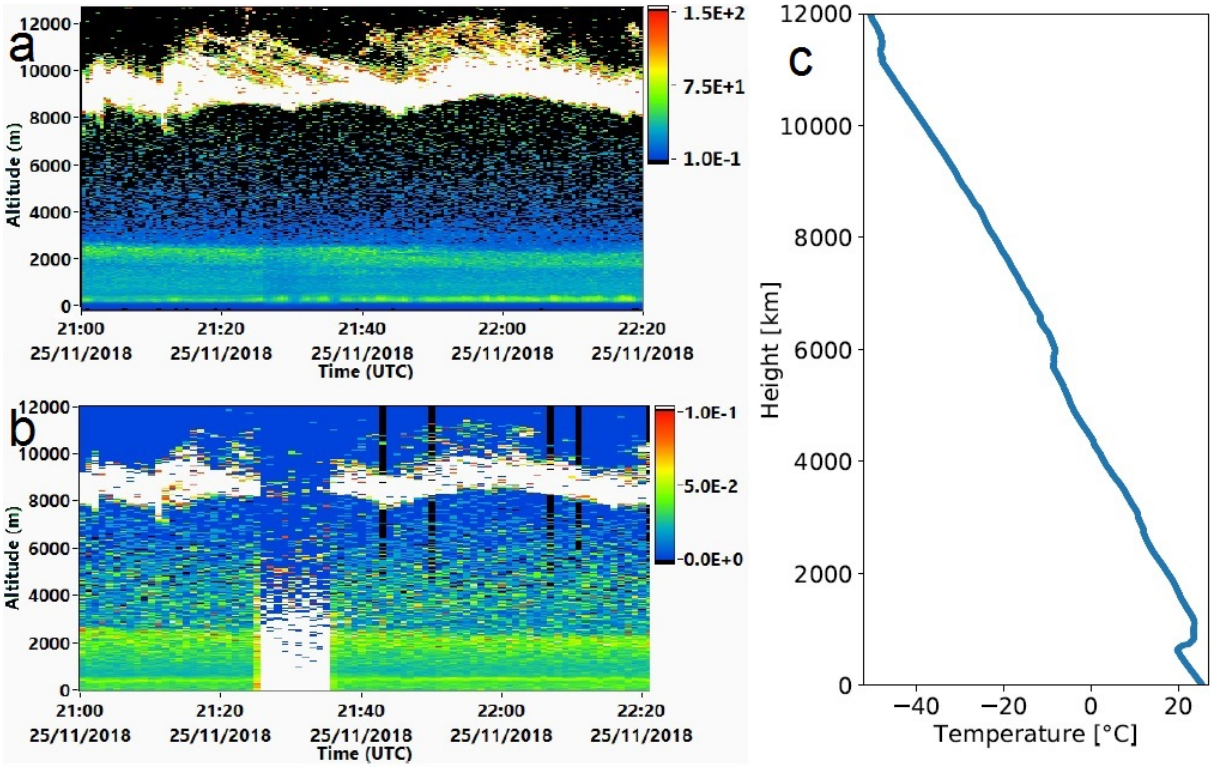

Figure 23: Time-height cross-section of a) range-corrected signal at 1064 nm and b) volume depolarization ratio at 532-nm wavelength; c) Radiosonde-based temperature profile on 25 November 2018, 1200 UTC (data from Schmithüsen (2019)). Shown is a case of a pronounced surface-near Saharan dust layer, a cirrus cloud between 8 and 12 km height, and a clean height region between 4 and 6 km, suitable as reference-height region for the backscatter coefficient with background aerosol conditions.

shown in Fig. 24a, the Klett method is used. It shows the backscatter coefficient profiles for three different profiles using a lidar ratio of 18.0 sr (black), 18.7 sr (orange), and 19.5 sr (green). Whenever the backscatter coefficient varies around 0 above the cloud-top, the chosen lidar ratio is correct for the cirrus cloud when assuming pure Rayleigh scattering below the cloud base. The lidar ratio of a cirrus cloud should usually be within 10 and 30 sr (Seifert et al., 2007). In this case, the orange curve (18.7 sr) varies noisy but most optimal around 0 $Mm^{-1}sr^{-1}$ above cloud top. Therefore, the chosen lidar ratio is 18.7 sr for the retrieval of the particle linear depolarization ratio of the cirrus cloud.
For the lidar ratio of the Saharan dust layer shown in Fig. 24b, the Raman method is used. It shows the lidar ratio from 1.25 km to 2.5 km height. It increases from 30 sr at 1.25 km height to around 55 sr at 2.5 km height. On average, 45 sr seems to be a reasonable value.
With the cloud thickness of approximately 2 km and an average backscatter coefficient of $2{\cdot}10^{-2}$ $km^{-1}sr^{-1}$, as well as the determined 18.7 sr as the lidar ratio, the cirrus cloud optical thickness results in 0.75. For the Saharan dust layer of approximately 2.5 km thickness, and an average particle backscatter coefficient of $2{\cdot}10^{-3}$ $km^{-1}sr^{-1}$ the aerosol optical thickness results in 0.23 (with the lidar ratio of 45 sr). As the layer between the Saharan dust layer and the cirrus cloud consists of almost only molecules which do not significantly contribute to the total aerosol optical thickness, the total aerosol optical thickness from the surface to the cirrus cloud-top is around 1. The lidar can penetrate through an optical thickness of 3. Therefore, the signal at cloud-top height is still large enough in order to apply the analyzing methods and to take this case as a representative

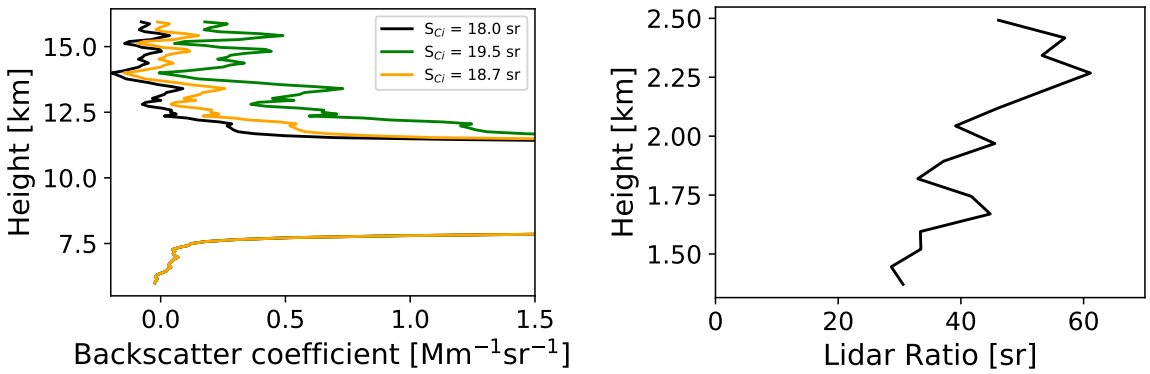

(a) Backscatter coefficient profiles for different chosen lidar ratios with the Klett method.

(b) Lidar ratio profile of the Saharan dust layer with Raman.

Figure 24: (a) profiles of particle backscatter coefficient for different lidar ratios as obtained with the Klett method for a cirrus cloud, and (b) the lidar ratio profile of the Saharan dust layer observed on 25 November 2018 as obtained with the Raman method. See Fig. 23 for an overview of the scene.

study.

Finally, Fig. 25 shows the backscatter coefficient profile in Fig. 25a1 and the particle linear depolarization ratio in Fig. 25b2 of both, the cirrus cloud (1) and the Saharan dust particles (2) as obtained with the Klett method.

As the reference backscatter coefficient is chosen to be constant with height here, it acts as an additional constant to the backscatter coefficient profile only. The backscatter coefficient curves for $0\,\mathrm{km^{-1}sr^{-1}}$, $1{\cdot}10^{-5}\,\mathrm{km^{-1}sr^{-1}}$, $1{\cdot}10^{-3}\,\mathrm{km^{-1}sr^{-1}}$, $1{\cdot}10^{-1}\,\mathrm{km^{-1}sr^{-1}}$ are therefore only shifted parallel to higher values if β_{ref} increases. The difference between $0\,\mathrm{km^{-1}sr^{-1}}$ and $1{\cdot}\ 10^{-5}\,\mathrm{km^{-1}sr^{-1}}$ is small.

The particle linear depolarization ratio (shown in Fig. 25b) also varies with varying β_{ref}. The larger β_{ref} gets the lower the particle depolarization ratio gets for the cirrus cloud, as well as for the Saharan dust layer. The particle depolarization ratio should be close to 50% (40-60%) for the cirrus cloud, and close to 30% for the Saharan dust layer. In both cases this fits best if β_{ref} gets close to $0\,\mathrm{km^{-1}sr^{-1}}$. As it is unlikely to have no aerosols at all in the atmosphere, the β_{ref}=$1{\cdot}10^{-5}\,\mathrm{km^{-1}sr^{-1}}$ seems most likely. The particle depolarization ratio for $1{\cdot}10^{-5}\,\mathrm{km^{-1}sr^{-1}}$ is only less than 1% lower than for $0\,\mathrm{km^{-1}sr^{-1}}$. A β_{ref} which is two orders of magnitude larger leads to an up to 7% (absolute) lower particle depolarization ratio of 16%, especially in the Saharan dust layer. This is deviating further from the expected 30%. Therefore, the background aerosol reference backscatter coefficient will be set to $\beta_{\mathrm{ref}} = 10^{-5}\,\mathrm{km^{-1}sr^{-1}}$ as a standard in the following. This value is always part of the calculated total particle backscatter coefficient. Therefore, it also needs to be accounted for as a source of uncertainty for the estimation of the number concentration of ice nucleating particles.

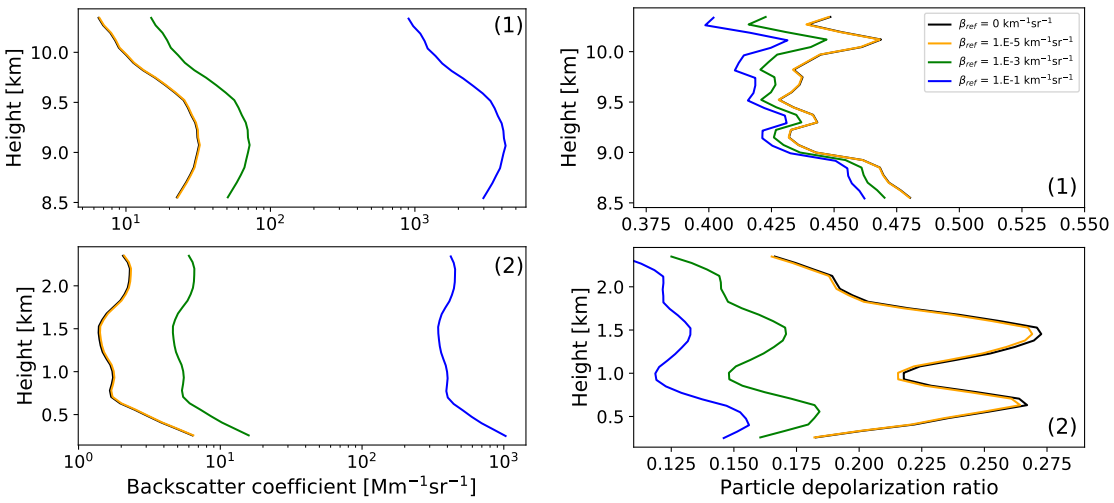

(a) Backscatter coefficient profiles for different chosen reference backscatter coefficients for the cirrus cloud (1) and the Saharan dust layer (2).

(b) Particle linear depolarization ratio profiles for different chosen reference backscatter coefficients for the cirrus cloud (1) and the Saharan dust layer (2).

Figure 25: Profiles of particle backscatter coefficient and particle linear depolarization ratio for different reference backscatter coefficients for the cirrus cloud (1) and the Saharan dust layer (2). See Fig. 23 for an overview over the scene.

5.4 Comparison of INP parametrizations

When profiles of particle backscatter coefficient and particle depolarization ratio are available, INP number concentrations can be retrieved applying the method of Mamouri and Ansmann (2016), which is introduced in Sec. 3.6. In this section, the relationship between aerosol optical properties and INP properties are illustrated. Figure 26 shows a comparison of INP-parametrizations assuming dust particles (red color space), or by assuming continental aerosols (green color space). The study is done for different particle backscatter coefficients in a typical range from 0.01 to 3 $\mathrm{Mm^{-1}sr^{-1}}$. This is done for the temperature range between 0 and −38°C for the US standard atmosphere.
For the desert dust INP-parametrizations shown as reddish graphs in Fig. 26a, the number of INP increases with increasing height (decreasing temperature) by approximately seven orders of magnitude between 0 and −38°C. In the logarithmic visualization it appears as a linear increase, such that an exponential increase of n_{INP} with decreasing temperature is expected. Furthermore, the curves are almost parallel to each other for different height-constant backscatter coefficients. In the chosen range of backscatter coefficients, one order of magnitude more of desert dust aerosol backscatter coefficient results in approximately one order of magnitude more ice nucleating particles.
If the INP-parametrization for continental aerosol is applied (green curves), it can be seen that these are usually more efficient ice nucleating particles between 2500 and 4500 m height (0 and −15°C). Here, the available INP are not strongly dependent on the backscatter coefficient. Higher up (or at lower temperatures), it can be seen that a saturation is almost reached. A lower temperature will not increase the number of INP strongly anymore (the effect is more pronounced for small continental particle concentrations). However, a higher backscatter coefficient of one order of magnitude will approximately increase the amount of INP by half an order of magnitude. At these temperatures between −30 and −38°C desert dust particles will be more efficient INP. Note that the most reliable results of the parametrization are within the temperature range from −9°C to −35°C for

continental aerosols and from $-21°C$ to $-35°C$ for desert dust aerosols. Principally, the parametrizations should only be applied within this temperature range. Otherwise, the results need to be analyzed more carefully.
A summarizing plot is shown in Fig. 26b. It shows the ratio of both parametrizations. The error in the number of INP can be in the order of up to three magnitudes which is especially the case for temperatures lower than -30°C, higher than -2°C (which is outside of the temperature range in which the parametrizations are well-working), and for very low backscatter coefficients. This means that the aerosol classification needs to be done carefully.
Comparing to case studies under real atmospheric conditions, Fig. 2 in Wex et al. (2019) presents samples of number concentrations of INP in Alert, Utqiagvik, Villum, and Ny-Ålesund. It can be seen that usual background aerosol conditions produce number concentrations of INP of $10^{-5}\,L^{-1}$ to $10^{-1}\,L^{-1}$ for temperatures between -5°C and -25°C. Comparing to Section 5.3 the backscatter coefficient of $10^{-5}\,km^{-1}sr^{-1}$ is the background aerosol backscatter coefficient. In Fig. 26 the number of INP is in the order of $10^{-1}\,L^{-1}$ for continental aerosols and in the order of $10^{-4}\,L^{-1}$ to $10^{-1}\,L^{-1}$ for desert dust aerosols in the comparable temperature range of $-5°C$ and $-25°C$ for a backscatter coefficient of $1 \cdot 10^{-2}\,Mm^{-1}sr^{-1}$. This means that the reference backscatter coefficient will already cause a number of INP which is in the same order of magnitude as high background aerosol conditions from the measurements in Wex et al. (2019). As the lidar technique deals with additional measurement noise, measurement signal and measurement noise can hardly be distinguished for background conditions. The lidar technique applied in this study is not sensitive enough to distinguish between high and low background aerosol conditions. Particle backscatter coefficients of at least one order of magnitude larger than the reference backscatter coefficient would be required in order to improve the signal to noise ratio. It can be seen that for certain temperature ranges the aerosol classification is even more important than the magnitude of the backscatter coefficient.

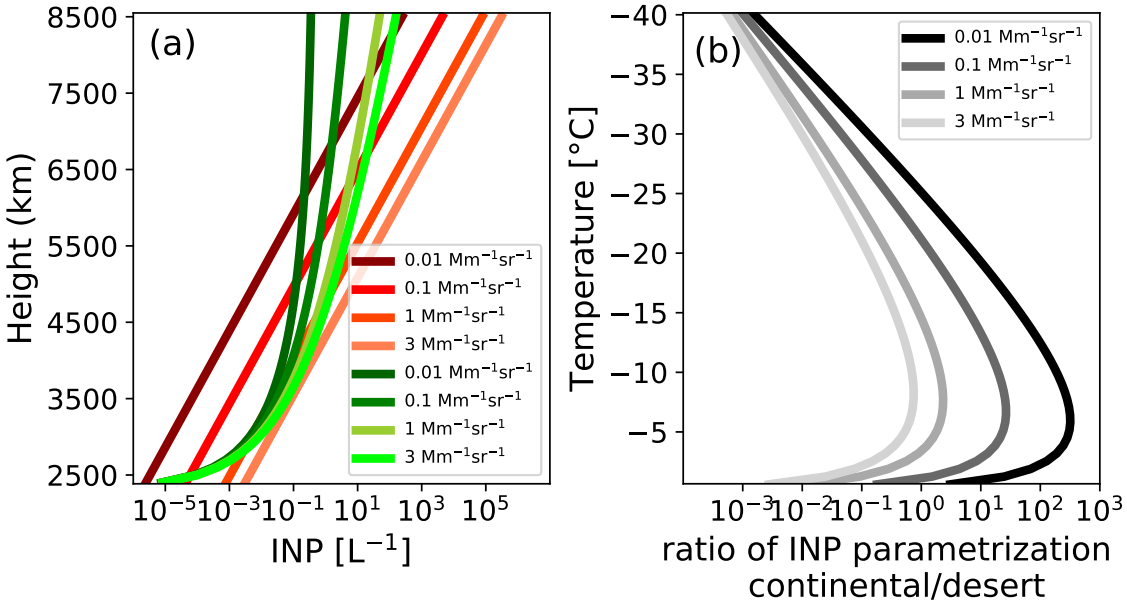

Figure 26: a) comparison of ice nucleating particle parametrizations (continental aerosol green, desert dust aerosol red), assuming different backscatter coefficients, and temperatures. b) the ratio of the INP curve assuming continental aerosols to assuming desert dust aerosols. It can be interpreted as an indicator for the order of magnitude of the uncertainty of INP type information. Important to note is that the vertical height axis is equivalent to the vertical temperature axis. Note that the most reliable results of the parametrization are within the temperature range of $-9°C$ to $-35°C$ for continental aerosols and $-21°C$ to $-35°C$ for desert dust aerosols for a) and b).

5.5 Sources of uncertainty in new lidar-based approach

The data analysis steps for the retrieval of INP number concentrations yield different sources of uncertainty. The classification of the aerosol type, the calculation of the backscatter coefficient, the conversion from backscatter coefficient into extinction coefficient, the conversion from extinction coefficient into particle number concentration, as well as the parametrization for the number concentration of ice nucleating particles are the largest sources of uncertainty.

The classification of the aerosol type is a crucial part of the analysis steps. As can be seen in Section 5.4 the uncertainty can reach up to three orders of magnitude in the sensitive temperature ranges assuming the desert dust particle parametrization compared to biomass burning smoke material. However, a careful aerosol type classification reduces the degree of uncertainty significantly.

The calculation of the backscatter coefficient is dependent on the lidar performance as well as the height and time region in which the lidar signal is averaged. The lidar measurement itself gives uncertainty of 30-50%. As aerosol concentrations may change quite fast, it is important to choose an appropriate time and height interval before the cloud. Choosing a short time period increases the signal noise. Choosing a long time period, it can not be guaranteed that the aerosol conditions stay constant.

The conversion of the backscatter coefficient into the extinction coefficient are dependent on the assumption for the lidar ratio. The lidar ratio is chosen to be constant with height and aerosol-type-dependent. Assuming the correct aerosol classification the uncertainty of the lidar ratio is usually in the range of 20-30%.

The conversion from extinction coefficient into particle number concentration is done using

conversion factors from an extended AERONET data analysis. This factor is a climatological value and may furthermore be uncertain. 20-30% measurement uncertainty may arise from here.
The parametrization from the particle number concentration to the INP number concentration is a further large source of uncertainty. Parametrizations are uncertain by a factor of 5, and may be even larger.
The total uncertainty after applying all steps is increasing step by step, and in total around one order of magnitude uncertainty may be realistic, in some cases even more. An absolute number is therefore hard to derive, to date, it is more a rough estimate of the INP situation in the surrounding of the clouds.
Furthermore, smaller uncertainties for the parametrization may arise when using radiosonde temperature and pressure data. The radiosonde is launched once per day only. Therefore, the atmosphere may have changed slightly in the time between.
When relating the number of INP to the phase of the cloud more uncertainty might be added by the classification of the cloud type. The cloud type classification is especially based on the combination of the backscatter coefficient signal as well as the volume depolarization ratio. An increased depolarization ratio below the cloud base is interpreted as an ice virga falling out of the cloud. However, there is an unknown threshold of a number concentration of ice crystals falling out of the cloud which is too small in order to significantly increase the volume depolarization ratio. Therefore, a cloud with a small number of ice crystals may be interpreted as a pure liquid water cloud. Furthermore, the volume depolarization ratio also increases within a liquid water cloud upwards due to multiple scattering events which may be misinterpreted as ice crystals. However, in well-defined clouds this phenomenon can clearly be separated from ice-containing clouds as the volume depolarization ratio must be close to 0 at cloud base in pure liquid water clouds.
One further effect which may add errors to this approach is the seeding effect. If an ice-forming cloud layer is located above the cloud of interest, ice crystals may fall into this cloud and may act as efficient ice nuclei. In this case cloud nucleation may not be related to the INP-situation only but also to the seeding effect. Therefore, these effects are excluded, meaning that clouds may not be accounted for if there is an ice-containing cloud above and the ice virga is detectable in less than 1 km of vertical distance.
All in all, this new approach is sensitive to many sources of uncertainty which makes it challenging to state qualitative statements at the current stage of the quality of the technique and methods. However, it is a good start and many improvable steps exist.

6 Case studies - Relating available INP to thermodynamic phase of clouds from MACC and lidar

In the previous Sections it was described how to relate aerosols and the thermodynamic phase of clouds. In the following Section all these methods will be applied to actual case studies. One case study is chosen to be close to Cape Verde on RV Polarstern, one case study was in the English Channel on RV Polarstern, and one case was a study chosen from the measurements at a lidar site in Dushanbe in Tajikistan. In the different cases different aerosol loads lead to different numbers of INP for different cloud-top temperatures. In the next step these numbers of INP are related to the cloud phase which is also measured by the lidar.

6.1 Mixed-phase cloud on 24 November 2018 close to Cape Verde (RV Polarstern)

Figure 27a shows the range-corrected signal at 1064 nm and the radiosonde temperature profile on 24 November 2018, 1200 UTC. First of all, the cloud free time from 1200 to 1520 UTC is striking. It was followed by an optically thin (optical thickness <3) cloud that occurred at heights between approximately 7 and 8 km. As can be seen from the radiosonde temperature profile in Fig. 27b, the temperature ranged from −4 to −28°C in the shown height range including the location of the cloud. This makes it an ideal case for the study of the direct influence of aerosol on the thermodynamic phase of the cloud due to heterogeneous freezing. All methods required for the INP retrieval and for the retrieval of the thermodynamic phase of the cloud are applied step by step for this case, as described in Section 3.

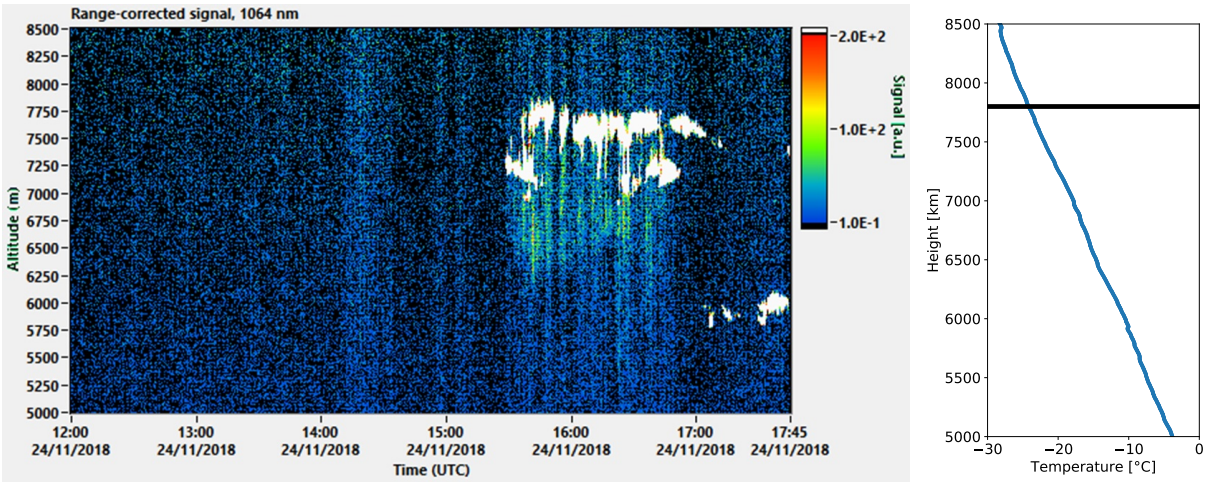

(a) Range-corrected signal at 1064 nm on 24 November 2018 from 1200 to 1745 UTC between 5 and 8.5 km height.

(b) Radiosonde temperature profile.

Figure 27: The range-corrected signal at 1064 nm and radiosonde temperature profile on 24 November 2018 at 1200 UTC (data from Schmithüsen (2019)) are shown between 5 and 8.5 km height with a reference height set between 4 and 5 km.

Regarding the scheme shown in Section 3.6 the first step of data processing is the aerosol classification. In this case, trajectories help in the classification of the aerosol type. Figure 28 shows the backward trajectories for three different height levels. The black star indicates the location of RV Polarstern on 24 November 2018, 1800 UTC. Following the backward trajectory at 7000 m height (green) to the northern part of South America leads to the assumption that the aerosol type was a mixture of emissions from the South American tropical region and the Atlantic ocean. The most important aerosol type released in tropical South America is usually biomass-burning smoke from the tropical rainforests (Seifert et al., 2015) which can reach altitudes of 7000 m when being lifted by deep convection (Gonzalez-Alonso et al. (2019), Angelo (2012)). The ocean can release sea salt in higher amounts, too (Schulz et al., 2004). However, there are no processes known where sea salt can reach altitudes of 7000 m. This leads to the assumption that the aerosol type is biomass-burning smoke. Another way to determine the aerosol type is by looking at the particle linear depolarization ratio which is shown in Fig. 29. The particle linear depolarization ratio was on average approximately 4% at the relevant height levels where the clouds occurred. Therefore, smoke or pollution seem to be the most likely aerosol types as only these particle types are known to produce particle linear depolarization ratios of below 5% (Illingworth et al., 2015). Desert dust can be excluded as an aerosol type, as the particle linear depolarization ratio would have to be much higher (Illingworth et al., 2015). The combination of trajectories and lidar observations lead to the classification of the aerosol type as smoke being the only aerosol type which seems reasonable by combining both methods.
After the aerosol type classification, the first step is to retrieve the backscatter coefficient of the aerosol in the vicinity of the cloud. Therefore, the backscatter coefficient profile from the lidar measurements is analyzed with the Klett method. For doing so, the recorded raw signals at 532-nm wavelength are averaged in time from 1200 UTC to 1520 UTC and also averaged in height from 7.4 km to 7.8 km. These are the time and height ranges where later on the cloud layer formed. The averaged particle backscatter coefficient results to β_{par}=5 $\cdot 10^{-2}\,\mathrm{Mm^{-1}sr^{-1}}$.
With an assumption of the lidar ratio of smoke as S_{par}=75 sr, the backscatter coefficient β_{par} can be transferred into the extinction coefficient $\sigma_{\mathrm{par}} = \beta_{\mathrm{par}} \cdot S_{\mathrm{par}}$=3.5 $\mathrm{Mm^{-1}}$.
With the conversion factor of $c_{290,\mathrm{c}}$=0.09 Mm $\mathrm{cm^{-3}}$ (see Section 3.6) the number concentration n results to $n = c_{290,\mathrm{c}} \cdot \sigma_{\mathrm{par}}$=0.3 $\mathrm{cm^{-3}}$.
The conversion from particle number concentration into the particle number concentration of INP is done with the parametrization 6. The final number concentration of ice nucleating particles results to $n_{\mathrm{INP,lidar}}$=0.9 $\mathrm{L^{-1}}$.

In former studies the INP retrieval was usually done by modeling the aerosol concentration. Therefore, a comparison between the lidar measurements and the MACC model data is done here. The input coordinates for the MACC model are 17°N and 19°W. As height level the pressure level of 400 hPa was chosen. The time for which the data extracted from MACC was 24 November 2018, 1500 UTC. The direct output of the model is shown in Fig. 30. It can be seen that the aerosol mass concentration at 400 hPa was found to be increased in the vicinity of the African continent. The aerosol load at the location of RV Polarstern reached a value of 3.38 µg $\mathrm{kg^{-1}}$. With the ideal gas law (see equation 8) this value is transferred into the aerosol mass concentration M_{par}=1.884 µg $\mathrm{m^{-3}}$.
In a next step the aerosol concentration is converted into an equivalent backscatter coefficient in order to make it comparable to the lidar measurement. Therefore, the parametrization in Mamouri and Ansmann (2017) is used as shown in Section 3.6. The

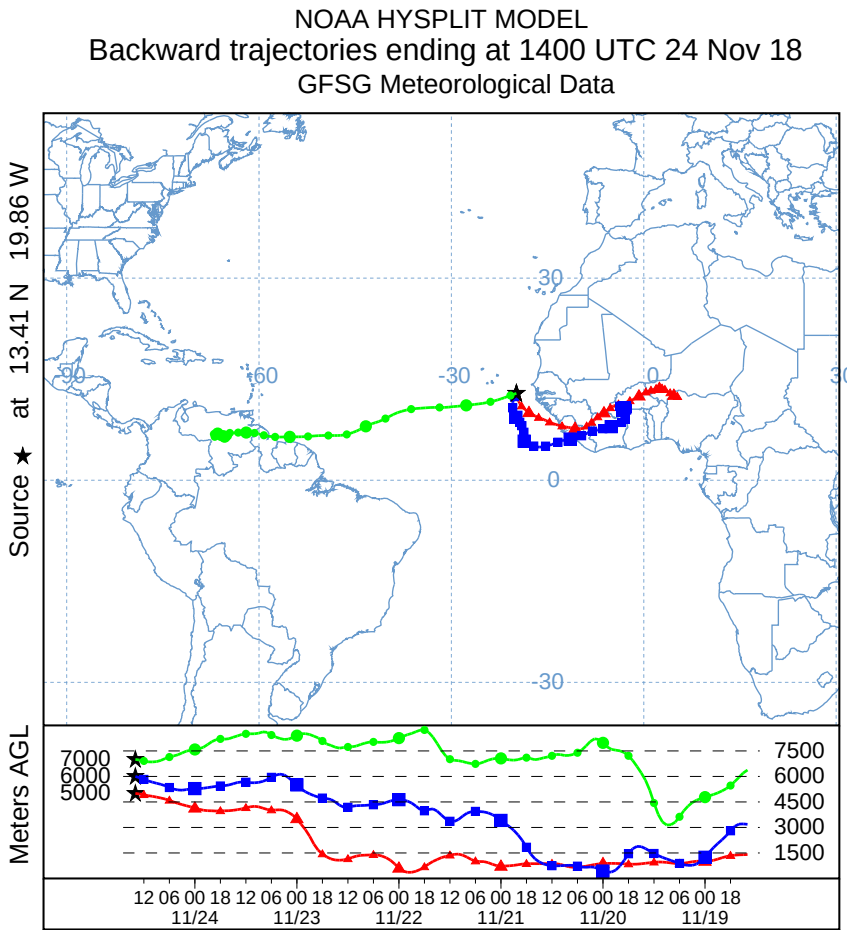

Figure 28: Backward trajectories ending at the location of RV Polarstern (13.41°N, 19.86°W) on 24 November 2018 at 1400 UTC for height levels of 5000 m, 6000 m, and 7000 m above ground level (Hysplit, 2019).

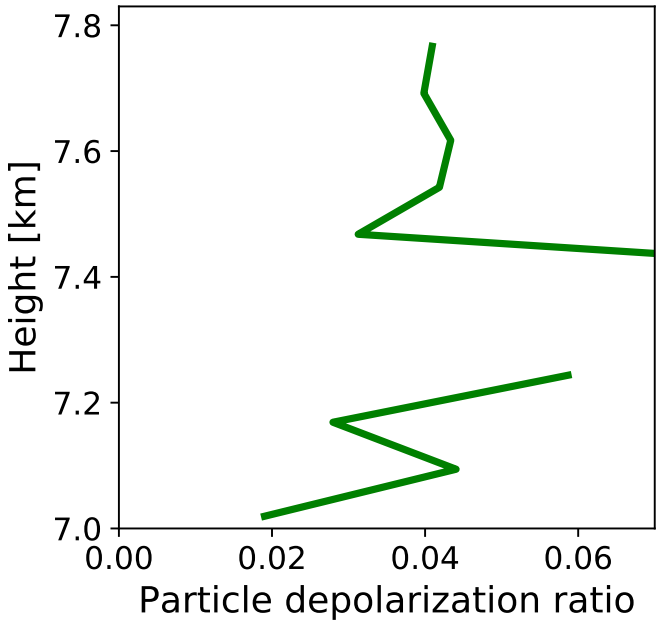

Figure 29: Mean profile of particle linear depolarization ratio for the case close to Cape Verde for 24 November 2018 between 1200 UTC and 1520 UTC.

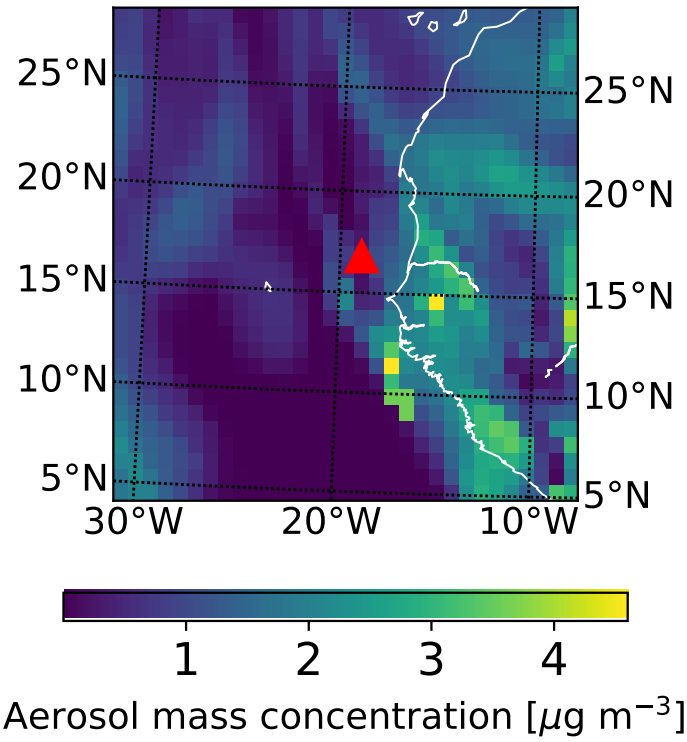

Figure 30: Aerosol mass concentration at 400 hPa height extracted from the MACC model for the vicinity of RV Polarstern (red triangle) for 24 November 2018, 1500 UTC (data from ECMWF (2019a)).

equivalent particle backscatter coefficient βpar, eq at 532 nm is:

$$\beta\text{par, eq} = \frac{M_{\text{par}}}{\rho_{\text{par}} c_{\text{v,par}} S_{\text{par}}} \tag{10}$$

with the mass concentration M_{par}, the particle density ρ_{par} (here $\rho_{\text{continental}}$=1.55 g cm^{-3}), the extinction-to-volume conversion factor $c_{\text{v,par}}$ (here $c_{\text{v,continental}}$=0.41 $\cdot$ 10^{-12} Mm), and the lidar ratio S_{par} (here $S_{\text{continental}}$=75 sr). The resulting $\beta_{\text{par,eq}}$ equals 3.3 $\cdot$10^{-2} Mm^{-1}sr^{-1}. With this value the same process as in the scheme in Fig. 12 for the INP retrieval will be done as for the lidar-retrieved backscatter coefficient. After applying the conversion factors and INP parametrization the final INP concentration from MACC is $n_{\text{INP,MACC}}$=0.5 L^{-1}.
Comparing $n_{\text{INP,MACC}}$ and $n_{\text{INP,lidar}}$, both values are in the same order of magnitude. As the measurements of the lidar, the MACC model data, as well as the parametrizations deal with quite some uncertainty, the resulting $n_{\text{INP,MACC}}$ and $n_{\text{INP,lidar}}$ can be considered to be in a good agreement, especially when considering that the absolute aerosol load is only slightly above the reference value (background aerosol).
The previous study part provided the number concentration of ice nucleating particles using two different methods. The well-known model-based method yields $n_{\text{INP,MACC}}$=0.5 L^{-1}, the new lidar-based method yields $n_{\text{INP,lidar}}$=0.9 L^{-1}. Further, the approach of this Master's thesis is to relate measured aerosol properties to the thermodynamic phase of the cloud. Therefore, the cloud characteristics still need to be determined in the following.
Figure 31a shows the 532-nm backscatter coefficient profile. It is based on the temporal average of all signal profiles observed between 1555 UTC and 1612 UTC as this part of the cloud was least scattered and broken, and the most constant in time (see Fig. 27a). The backscatter coefficient increased starting at approximately 7.3 km height, this is defined

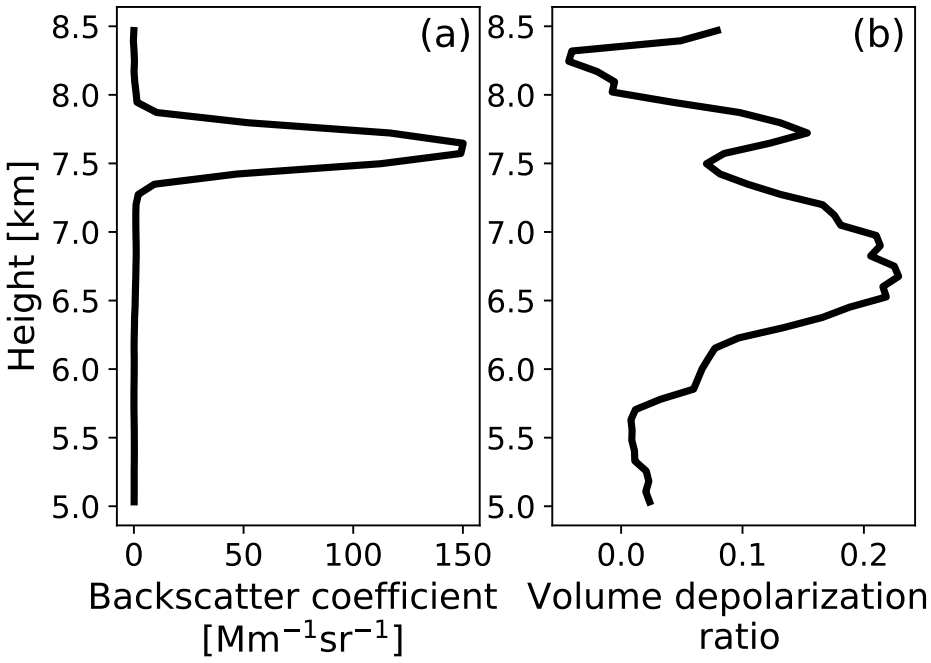

Figure 31: Profiles of the 532-nm particle backscatter coefficient (a) and the volume depolarization ratio between 5 and 8.5 km height (b) of a cloud observed with lidar from aboard RV Polarstern on 24 November 2018. The profiles are averaged over the time period from 1555 UTC to 1612 UTC with a vertical smoothing length of 300 m.

as the cloud-base height. Above the signal maximum, an extinction-related decrease of the signal up to a height of 7.9 km can be seen. There, the signal did not decrease further, such that this height level is defined as the cloud-top height. When searching for the temperature at the derived cloud-top height in the radiosonde data in Fig. 27b the cloud-top temperature is found. Here it is derived as −24°C.
Figure 31b shows the volume depolarization ratio profile between 5 km and 8.5 km height for the same averaging time period as for Fig. 31a. The higher the volume depolarization ratio is, the more nonspherical particles are situated within the volume. As can be seen, the volume depolarization ratio was highest between 6.5 km and 7 km height, which is lower than the cloud-base height. In this case this is interpreted as ice crystals falling out of the cloud (ice virga). Hence this means that the cloud must have contained ice. Therefore, the cloud is classified as a mixed-phase cloud, i.e. an ice-containing cloud.
For the confirmation of this classification Fig. 32 shows the backscatter coefficient in Fig. 32a and the volume depolarization ratio in Fig. 32b with the scaling adjusted. Also here the cloud base (increasing backscatter coefficient) can be interpreted to be located at around 7 km height, whereas the volume depolarization ratio was increased below the cloud base.
All in all, this case study shows that approximately $n_{\mathrm{INP,MACC}}$=0.5 L^{-1} from MACC, or $n_{\mathrm{INP,lidar}}$=0.9 L^{-1} from lidar measurements (assuming smoke particles) were sufficient in order to form ice in a cloud with a cloud-top temperature of -24°C.
However, the lidar-based classification into pure-liquid water clouds and ice-containing clouds remains to be an error-prone task. Clouds can already contain ice in low amounts even if the lidar technique shows no sign for ice crystals forming within the cloud. In Bühl et al. (2013a) a threshold of $\rho_{\mathrm{IWC,Threshold}} = 1 \cdot 10^{-6}\,\mathrm{kg\,m^{-3}}$ ice water content was defined below which ice crystals might not be detectable by the lidar technique. This means that in this case study the ice water content must have been larger than the threshold in Bühl

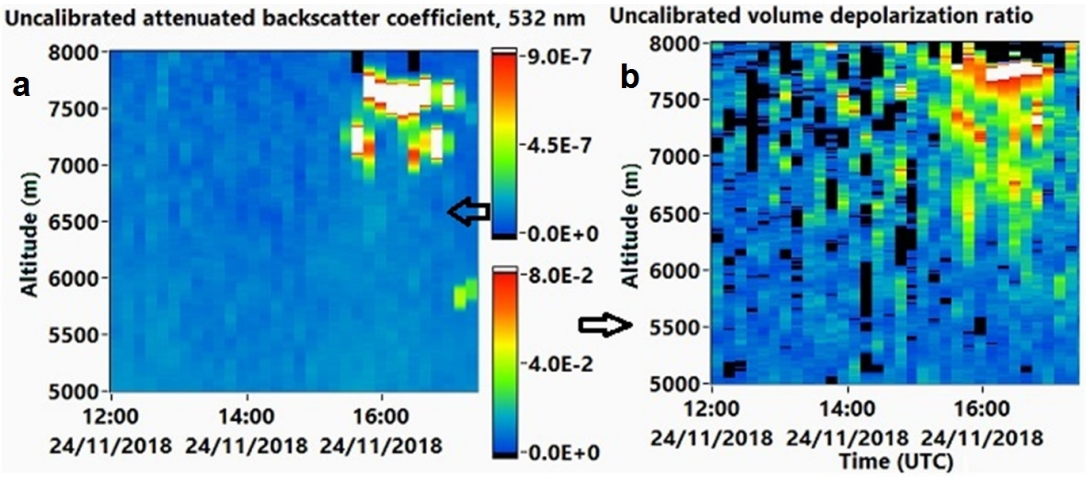

Figure 32: Time-height cross-sections of uncalibrated attenuated backscatter coefficient (a) and volume depolarization ratio (b) of a cloud observed from aboard RV Polarstern on 24 November 2018 between 1200 UTC and 1740 UTC.

et al. (2013a) as the cloud was classified as ice-containing.
Going one step further one can calculate the smallest-possible average ice crystal diameter when using the threshold for the ice water content as well as the ice nucleating particle number concentration. Assuming an idealized case that every ice nucleating particle triggers ice formation and that ice crystals can only have spheroidal shape, the minimal average diameter can be calculated. Knowing that ice was detected by lidar below the cloud, means that the ice water content in this case study $\rho_{\mathrm{IWC,24NOV2018}}$ must have been larger than the threshold $\rho_{\mathrm{IWC,Threshold}}$ ($\rho_{\mathrm{IWC,24NOV2018}} \geq \rho_{\mathrm{IWC,Threshold}}$).
$\rho_{\mathrm{IWC,24NOV2018}}$ is dependent on the number of ice crystals in a volume $n_{\mathrm{icecrystals}}$ (assuming that every INP triggers heterogeneous ice formation $n_{\mathrm{icecrystals}}$ is equal to the INP number concentration: $n_{\mathrm{icecrystals}}$=n_{INP}) and the mass of the ice crystals $m_{\mathrm{icecrystals}}$ with:

$$\rho_{\mathrm{IWC,24NOV2018}} = n_{\mathrm{icecrystals}} \cdot m_{\mathrm{icecrystals}} \tag{11}$$

$m_{\mathrm{icecrystals}}$ can be calculated from the density of ice $\rho_{\mathrm{ice}} = 918\,\mathrm{kg\,m^{-3}}$ and the volume of a single ice crystal $V_{\mathrm{icecrystal}}$. Assuming spheroidal ice crystals only, $V_{\mathrm{icecrystal}}$ depends on the radius of the ice crystal $r_{\mathrm{icecrystal}}$ with $V_{\mathrm{icecrystal}}$=$\frac{4}{3}\pi r^3_{\mathrm{icecrystal}}$.
Therefore, the mass of ice crystals results to:

$$m_{\mathrm{icecrystals}} = \rho_{ice} \cdot V_{\mathrm{icecrystal}} = \rho_{\mathrm{ice}} \cdot \frac{4}{3}\pi \mathrm{r}^3_{\mathrm{icecrystal}} \tag{12}$$

Inserting $m_{\mathrm{icecrystals}}$ into Eq. 11 and solving for $r_{\mathrm{icecrystal}}$ yields:

$$r_{\mathrm{icecrystal}}(n_{\mathrm{icecrystals}}) = (\frac{3\rho_{\mathrm{IWC,Threshold}}}{4\pi n_{\mathrm{INP}} \rho_{\mathrm{ice}}})^{\frac{1}{3}} \tag{13}$$

Inserting all the constants into Eq. 13 yields $r_{\mathrm{icecrystal}}(n_{\mathrm{icecrystals}})$=$6.38 \cdot 10^{-4} \cdot n_{\mathrm{INP}}^{-\frac{1}{3}}$.
Finally, the diameter of the ice crystals $d_{\mathrm{icecrystal}}(n_{\mathrm{icecrystals}})$ is twice as large as $r_{\mathrm{icecrystal}}(n_{\mathrm{icecrystals}})$:

$$d_{\mathrm{icecrystal}}(n_{\mathrm{icecrystals}}) = 2 \cdot r_{\mathrm{icecrystal}}(n_{\mathrm{icecrystals}}) = 1.28 \cdot 10^{-3} \cdot n_{\mathrm{INP}}^{-\frac{1}{3}} \tag{14}$$

Equation 14 delivers a simple dependency between the threshold diameter of ice crystals and the ice nucleating particle number concentration. In the previous case study the INP number concentrations $n_{\mathrm{INP,MACC}}$=$0.5\,\mathrm{L^{-1}}$ from MACC and $n_{\mathrm{INP,lidar}}$=$0.9\,\mathrm{L^{-1}}$

from lidar were determined. Thus, using equation 14, the smallest possible average diameters of the spheroidal ice crystals would be $d_{\mathrm{icecrystal}}(n_{\mathrm{INP,MACC}}) = 160.8\,\mu\mathrm{m}$ and $d_{\mathrm{icecrystal}}(n_{\mathrm{INP,lidar}}) = 132.2\,\mu\mathrm{m}$. Usually ice crystals start to fall out of the cloud when they reach a diameter of 1 mm (Box and Box (2015)). Therefore, the results seem to be reasonable as the ice crystals must be larger than the calculated minimum value of approximately 150 µm.
The retrieved idealized size of the ice crystals can in a next step even be converted into the respective radar reflectivity factor, as it would be observed with a standard Ka- or W-band cloud radar, such as the 35-GHz cloud radar operated within the Leipzig Aerosol and Cloud Remote Observations System (LACROS, Bühl et al. (2013b)) of TROPOS. Applying Eq. (1) from Hogan et al. (2006) yields the radar reflectivity factor Z as:

$$Z(n_{\mathrm{INP}}(d), d) = \frac{1}{0.93} \int_0^\infty n_{\mathrm{INP}}(d)|K(d)|^2 d^6 \gamma(d) \mathrm{d}d \tag{15}$$

As scattering by solid ice spheres and absence of extinction effects is assumed in the presented case it is a monomodal distribution, so the ratio of the actual backscattering cross-section $\gamma(d)$=1 and dd cancels out, respectively. The dielectric factor of solid ice $|K(d)|^2$ is equal to 0.174. In this case the radar reflectivity would have to be at least $Z_{\mathrm{MACC}}(0.5\,\mathrm{L}^{-1}, 160.8\,\mu\mathrm{m}) = -27.9\,\mathrm{dBZ}$ for the MACC-retrieved method, and for the lidar-retrieved method $Z_{\mathrm{lidar}}(0.9\,\mathrm{L}^{-1}, 132.2\,\mu\mathrm{m}) = -30.5\,\mathrm{dBZ}$.

6.2 Liquid water cloud 13 November 2018 above the English Channel (RV Polarstern)

This Section discusses another case of a cloud layer that occurred on 13 November 2018 and could potentially have been subject to heterogeneous ice formation. The 1064 nm time-height cross-section of the lidar observation from 1912 UTC to 2358 UTC, as well as the corresponding radiosonde-based temperature profile for 1200 UTC for the height range from 5 to 7 km are shown in Fig. 33b. A cloud layer prevailed from approximately 1912 to 2100 UTC at heights between 6 and 6.6 km. After 2100 UTC there was a cloud-free atmosphere observed until midnight.
In this case study the methods presented in 3.6 are applied for one more time.

Again, the data analysis procedure, as shown in Sec. 3.6, is started with the aerosol classification. Figure 34 provides the backward trajectories ending at heights of 4000, 5000, and 6000 m above RV Polarstern on 13 November 2018, 1800 UTC. Following these backward trajectories it can be seen that the air was moving over the sea for a long distance but a short time only. However, before that time the trajectory crossed the USA. Therefore, it cannot be excluded that continental aerosol is present in the air mass. Furthermore, sea salt contributes by 3 orders of magnitude less to the number concentration of ice nucleating particles (Mamouri and Ansmann, 2016). In this case the aerosol type would therefore be classified as continental (US American) aerosol.

In the next step the backscatter coefficient is retrieved from the lidar measurements. In this case the amount of clouds in the relevant height region was too high before the cloud of interest occurred. Therefore, the retrieval of the particle backscatter coefficient was not possible before the cloud appeared, and was such applied afterwards to the lidar observation from the time period from 2115 UTC to 2358 UTC. This measurement period is chosen in order to determine the particle backscatter coefficient β_{par} with the Raman method. The height- and time-averaged β_{par} was found to be $1.1 \cdot 10^{-2}\,\mathrm{Mm}^{-1}\mathrm{sr}^{-1}$.
With an assumed lidar ratio of S_{par}=35 sr for continental aerosol the particle extinction

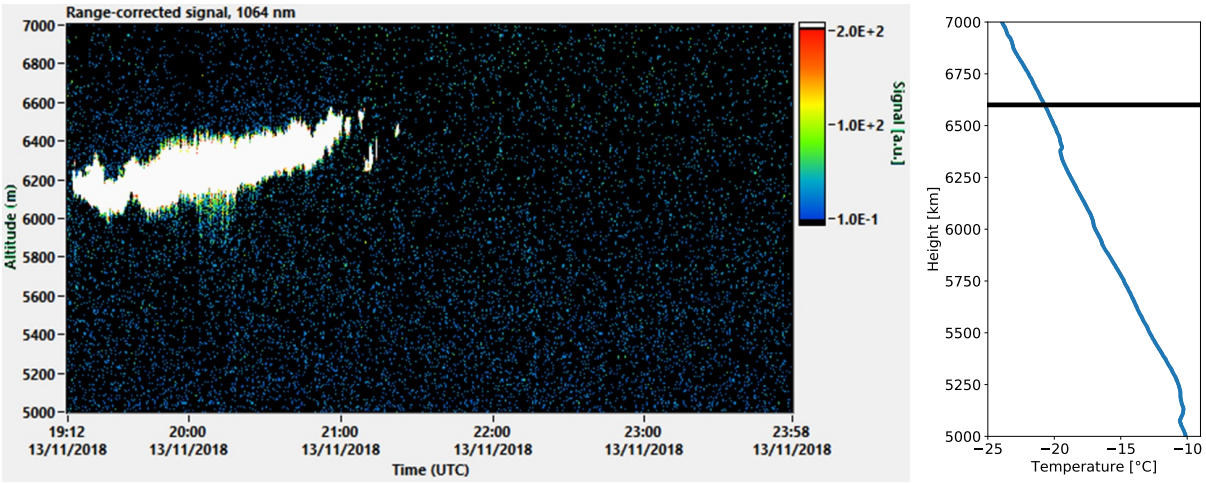

(a) Range-corrected signal at 1064 nm on 13 November 2018 from 1912 to 2358 UTC between 5 and 7 km.

(b) Radiosonde temperature profile.

Figure 33: 1064-nm range-corrected signal on 13 November 2018 and the radiosonde temperature profile on 14 of November 2018 from 1200 UTC (data from Schmithüsen (2019)) shown for between 5 and 7 km height. The reference height is set between 4 and 5 km.

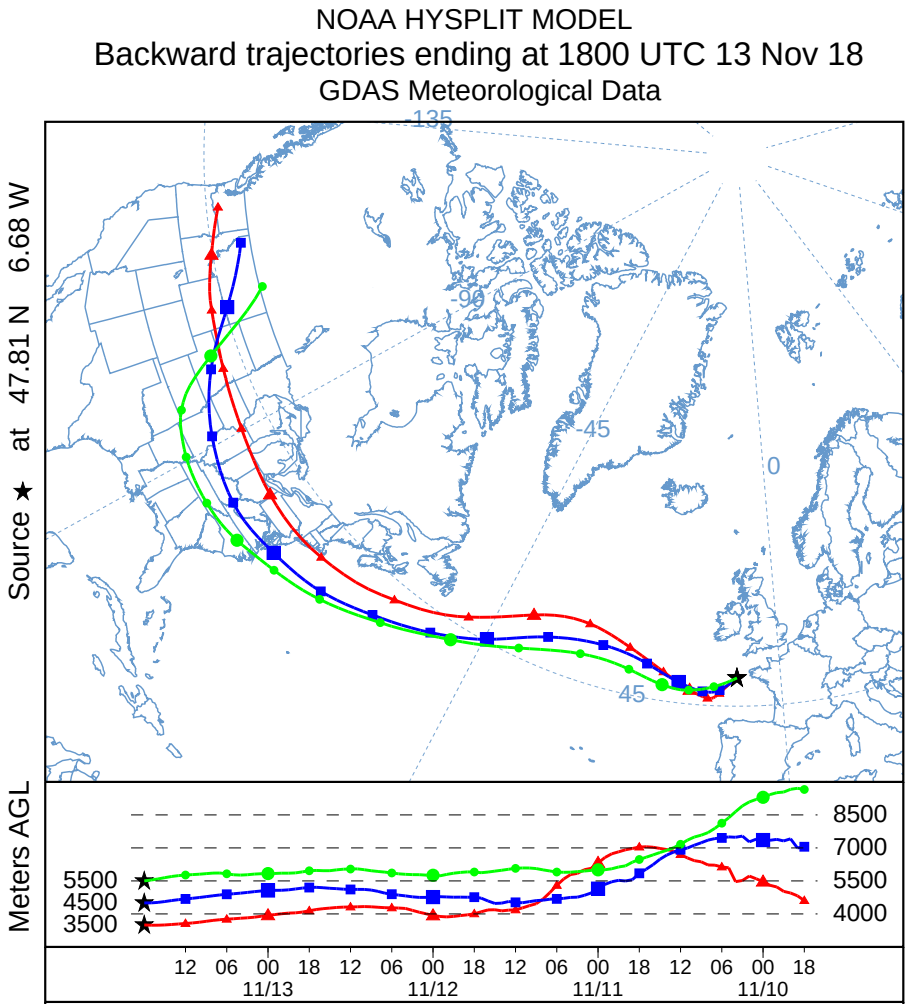

Figure 34: Backward trajectories ending over RV Polarstern on 13 November 2018, 1800 UTC (Hysplit, 2019).

coefficient results to σ_{par}=0.39 Mm^{-1}. The conversion factor $c_{290,\mathrm{c}}$=0.06 Mm cm^{-3} (see Eq. 9) leads to a particle number concentration of n_{290}=0.023 cm^{-3}.
Finally, the parametrization for continental aerosol from Mamouri and Ansmann (2016) (see Section 3.6) is applied. It yields the number concentration of ice nucleating particles of $n_{\mathrm{INP,lidar}}$=0.1 L^{-1}. This is less than a third of the number concentration of the case study presented in Section 6.1. Therefore, the probability of the cloud not to contain ice is increased.
Still, a comparison to the MACC-model-derived INP number concentration is done. The MACC model provides an output of the aerosol mass mixing ratio of 0.41 µg kg^{-1} for the gridpoint of 48.5°N and 6.3°W at the pressure level of 500 hPa on 13 November 2018, 2100 UTC. In Fig. 35 a lat-lon map of the 500 hPa aerosol mass concentration is shown. RV Polarstern was located in the middle of the area covered by Fig. 35 and seems to be in a relatively weakly polluted area at the 500 hPa level with 0.41 µg kg^{-1} of total aerosol mass concentration. This number is converted into the aerosol mass concentration of 0.29 µg m^{-3} by applying the ideal gas law. In the next step the parametrization for continental aerosol particles from Mamouri and Ansmann (2017) provides the equivalent particle backscatter coefficient of 3.5 $\cdot 10^{-2}$ Mm^{-1}sr^{-1}. Again, the conversion into extinction coefficient, particle number concentration and INP number concentration is done in the same way as for the lidar measurements. The final number concentration of INP from the MACC model is $n_{\mathrm{INP,MACC}}$=0.2 L^{-1}.
Comparing $n_{\mathrm{INP,MACC}}$ to $n_{\mathrm{INP,lidar}}$ it can be seen that these are again in the same order of magnitude. The particle backscatter coefficients derived from lidar and MACC differed by a factor of three, whereas the number of INP differ by a factor of 2. This is a result of the medium weak dependence from the continental aerosol INP parametrization on the number of INP for temperatures around −20°C. However, both numbers are similar and therefore in a good agreement. Also, both values (derived from lidar and derived from MACC) are smaller on 13 November 2018 than in the case study shown in Section 6.1 for 24 November 2018. However, the backscatter coefficients in both case studies were only slightly higher than the reference backscatter coefficient, so it is appreciable to compare to a case with a higher aerosol load (as will be done in Sec. 6.3).
The numbers of INP n_{INP} of approximately 0.1 and 0.2 L^{-1} as obtained from lidar and MACC, respectively, are in a next step directly related to the thermodynamic phase of the cloud. Therefore, the cloud characteristics need to be determined. In Fig. 36, profiles of the 532-nm particle backscatter coefficient and volume depolarization ratio are shown, which were obtained from the time period of cloud occurrence shown in the time-height cross-section of both parameters in Fig. 37. At slightly below 6.0 km height, the backscatter coefficient (shown in Fig. 36a) starts to increase with height. This is where the cloud-base height is located. The cloud-top height is located where the backscatter coefficient does not decrease further with height and reaches background level. This is the case at approximately 6.6 km. From the cloud-top height the cloud-top temperature can be retrieved by comparison to the radiosonde data shown in Fig. 33b. A cloud-top temperature of −21°C can be found which is similar to the case in Section 6.1.
Figure 36b shows the 532-nm volume depolarization ratio profile for the height range from 5 to 7 km. The height where the signal has its maximum as well as the signal structure shape look similar to the backscatter coefficient profile. In the case study in Sec. 6.1 a higher volume depolarization ratio was interpreted as ice crystals below the cloud. In this case an increase in volume depolarization ratio below the cloud is not visible. The increase of the volume depolarization ratio within the cloud is a result of multiple scattering of photons at the liquid cloud droplets. Multiple scattering leads to the reception of backscatter signals from photons which already previously experienced one or more

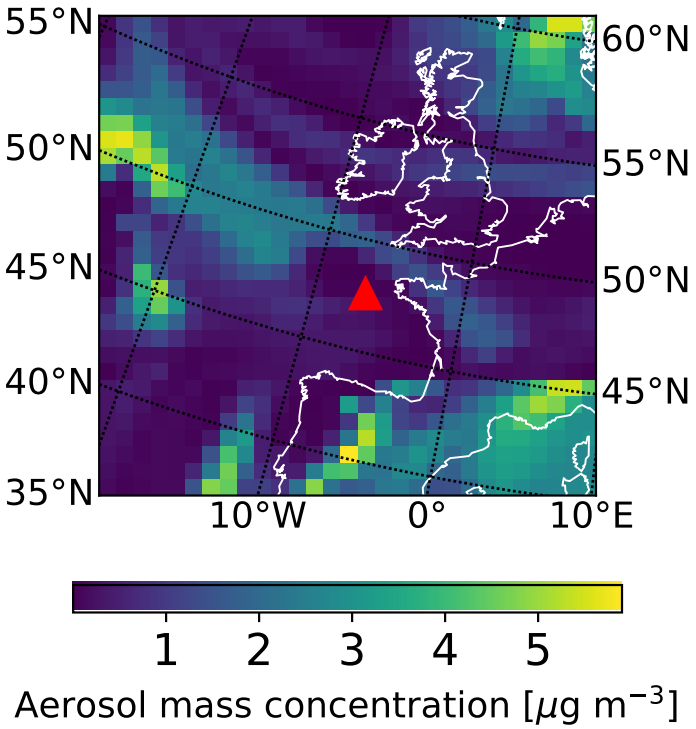

Figure 35: Aerosol mass concentration at 500 hPa height extracted from the MACC model for the vicinity of RV Polarstern (red triangle) on 13 November 2018, 2100 UTC (data from ECMWF (2019a)).

scattering events into an arbitrary direction. The effective backscattering angle of the multiple-scattered photons however deviates from 180°, which causes also the depolarization ratio to be larger than 0. With increasing cloud penetration depth, the likelihood for multiple scattering increases which goes along with a rather linear increase of the volume depolarization ratio profile within a liquid cloud layer, as it is the case here.
In conclusion, the discussed cloud layer is classified as a pure-liquid water cloud.

In this case study an INP number concentration of $0.1\,\mathrm{L}^{-1}$ from lidar, or $0.2\,\mathrm{L}^{-1}$ from MACC were not sufficient in order to form an ice-containing mixed-phase cloud at −21°C. As described in Sec. 6.1 clouds may contain a small amount of ice water which is less than the threshold $\rho_{\mathrm{IWC,Threshold}}$. It would not be detected by the lidar technique. Assuming that the ice water content must have been lower than $\rho_{\mathrm{IWC,Threshold}}$ in this case study (as the cloud was classified as a pure-liquid water cloud), this means that the largest possible average diameters of the spherical ice crystals would be $d_{\mathrm{icecrystal}}(n_{\mathrm{INP,MACC}})$ =218.2 µm and $d_{\mathrm{icecrystal}}(n_{\mathrm{INP,lidar}})$ =275.0 µm according to Eq. 14. If the average diameter of the ice crystals would have been larger (assuming that every INP triggers heterogeneous ice formation), the lidar would likely have detected ice crystals.
Coming to another conclusion, it also means that if there would have been a cloud radar available, it would have measured a lower reflectivity than a certain value. Using Eq. 15 in Sec. 6.1 the maximal possible radar reflectivities would be $Z_{\mathrm{MACC}}(0.2\,\mathrm{L}^{-1}, 218.2\,\mu\mathrm{m})$=−23.9 dBZ for the MACC-retrieved method or $Z_{\mathrm{lidar}}(0.1\,\mathrm{L}^{-1}, 275.0\,\mu\mathrm{m})$=−20.9 dBZ for the lidar-retrieved method.
Compared to the case study discussed in Section 6.1 where an approximately three times higher number of INP lead to heterogeneous ice formation in the cloud at a similar cloud-top temperature, one could already get to the assumption that a higher number of ice nucleating particles leads to a higher probability of a cloud to contain ice. However,

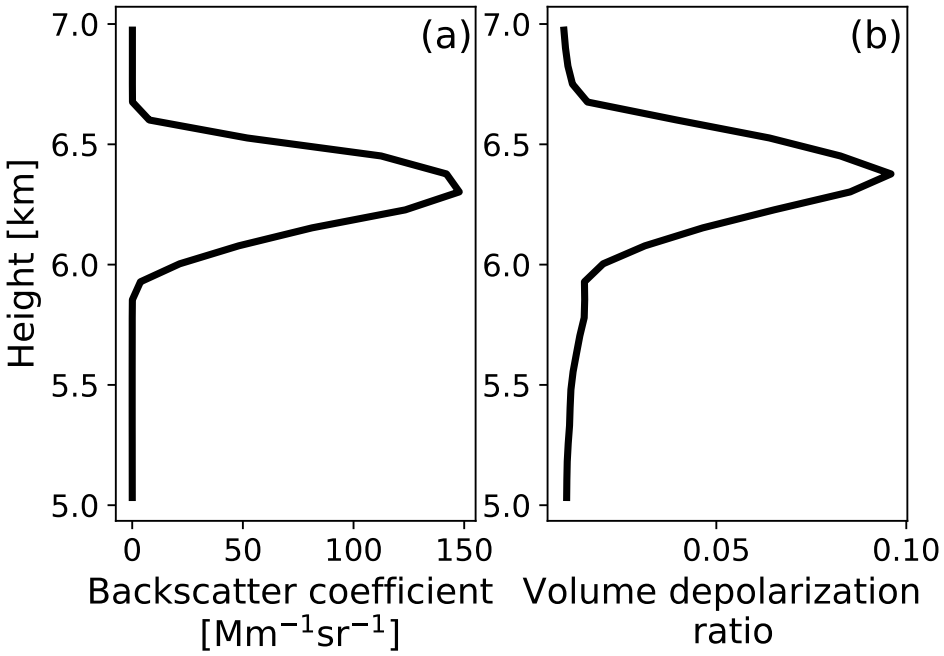

Figure 36: Profiles of the 532-nm wavelength particle backscatter coefficient (a) and the volume depolarization ratio between 5 and 7 km height (b) of a cloud observed with lidar on RV Polarstern on 13 November 2018. The profiles are averaged over the time period from 1917 UTC to 2030 UTC with a vertical smoothing length of 300 m.

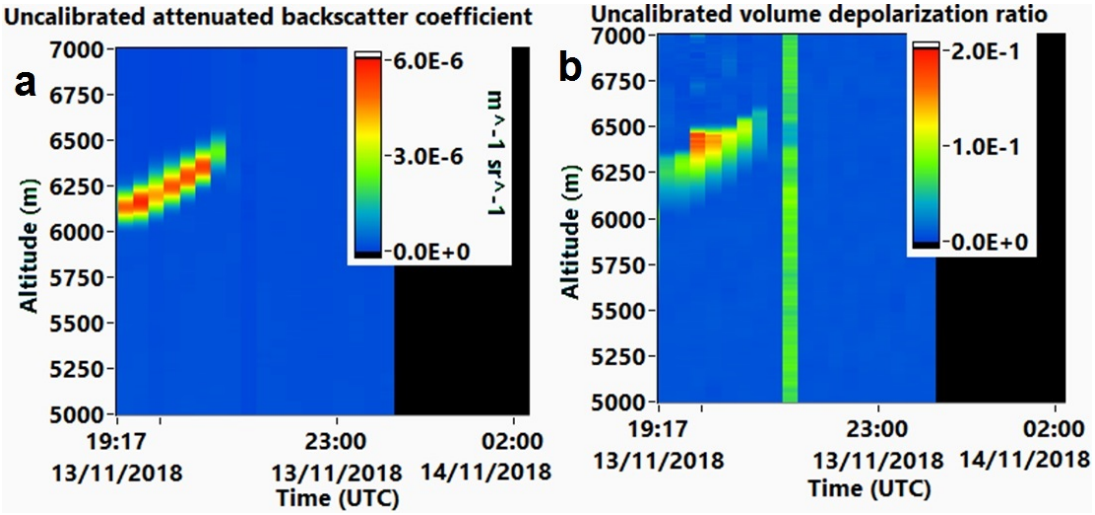

Figure 37: Time-height cross-sections of uncalibrated attenuated backscatter coefficient (a) and volume depolarization ratio (b) of a cloud observed from aboard RV Polarstern between 13 November 2018, 1917 UTC and 14 November 2018, 0200 UTC.

these were only two chosen case studies, or method demonstration studies. In order to get statistically relevant results more case studies need to be analyzed and statistics including the number of INP need to find a relationship between the number of INP and the thermodynamic phase of clouds. However, a statistical analysis of the RV Polarstern data is not possible at the current stage. On the one hand, the aerosol concentrations at the relevant heights were usually only slightly above the reference value during the cruise PS116. On the other hand the signal noise is frequently high, which decreases the amount of analyzable cases.

6.3 Mixed-phase cloud on 08 July 2019, Dushanbe (Tajikistan)

During the RV Polarstern cruise PS116 the aerosol concentrations were found to be weak during the whole cruise in the surrounding of clouds which had a detectable cloud-top between 0 and −38°C. The highest backscatter coefficient in the vicinity of a targeted cloud layer was 0.3 $Mm^{-1}sr^{-1}$ only. This is just slightly higher than background aerosol conditions, meaning the reference backscatter coefficient. Therefore, the following case study deals with a measurement by a Polly^{XT} lidar operated by TROPOS in Dushanbe (Tajikistan, 38.6°N, 68.8°E) in a highly polluted environment.

During the RV Polarstern cruise PS116 the aerosol concentrations were found to be weak during the whole cruise in the surrounding of clouds which had a detectable cloud-top between 0 and −38°C. The highest backscatter coefficient in the vicinity of a targeted cloud layer was 0.3 $Mm^{-1}sr^{-1}$ only. This is just slightly higher than background aerosol conditions, meaning the reference backscatter coefficient. Therefore, the following case study deals with a measurement by a Polly^{XT} lidar operated by TROPOS in Dushanbe (Tajikistan, 38.6°N, 68.8°E) in a highly polluted environment.

Figure 38 shows the range-corrected signal at 1064 nm wavelength during the night of 8 to 9 July 2019 in Dushanbe. Various cloud layers at approximately 4 and 5 km can be seen. Especially from 0040 UTC to 0115 UTC strong ice virgae are obvious. The question arises how the aerosol properties are situated in the surrounding of the cloud.

Therefore, the time period from before the first cloud layer occurred is analyzed in terms of aerosol properties. As an overview, Fig. 39 presents the time-height cross-section of the 1064 nm range-corrected signal for the time period from 5 to 1 hours before the first cloud occurrence. It should be noted that the color scales were set differently in Fig. 38 and Fig. 39 in order to highlight the cloud structure and aerosol structure, respectively. In Fig. 39 a pronounced aerosol layer can be seen, that extends from the surface up to altitudes of more than 5 km. Furthermore, no cloud occurred between 1800 UTC and 2256 UTC. During this measurement period the received backscattered signals can be averaged in time in order to retrieve a vertical profile of the backscatter coefficient with the Raman method and the number of INP.

Again, the retrieval of the number concentration of INP starts with the classification of the aerosol type. For this, combined lidar measurements and modeled backward trajectories help. The backward trajectories shown in Fig. 40 may give indications on the particle type. It can be seen that the trajectories at the relevant heights of 3000 m, 4000 m, and 5000 m reach regions which are in the west of Tajikistan. These regions are all arid and tend to desertification, however, air is not advected from an actual desert as in Saudi-Arabia. Therefore, at these heights only a low amount of desert dust particles and a higher amount of pollution and continental aerosols seems reasonable.

A multi-wavelength analysis of the aerosol optical properties obtained from the signals averaged over the time period shown in Fig. 39 is presented in Fig.41. In Fig. 41a the 532-nm backscatter coefficient shows values of 1.5 $Mm^{-1}sr^{-1}$ in the height range from 0 to 4 km. Above, it decreases to values of around 1 $Mm^{-1}sr^{-1}$. These values are almost one order of magnitude larger than it was usually observed at cloud-relevant heights during the RV Polarstern cruise. In Fig. 41a the particle backscatter coefficient of the 355-nm channel looks similar to the 532-nm channel, whereas the backscatter coefficient at 1064-nm wavelength was only half as large. This may be an indication for quite large particle sizes.

Figure 41b shows the particle linear depolarization ratio profile. Between the surface and

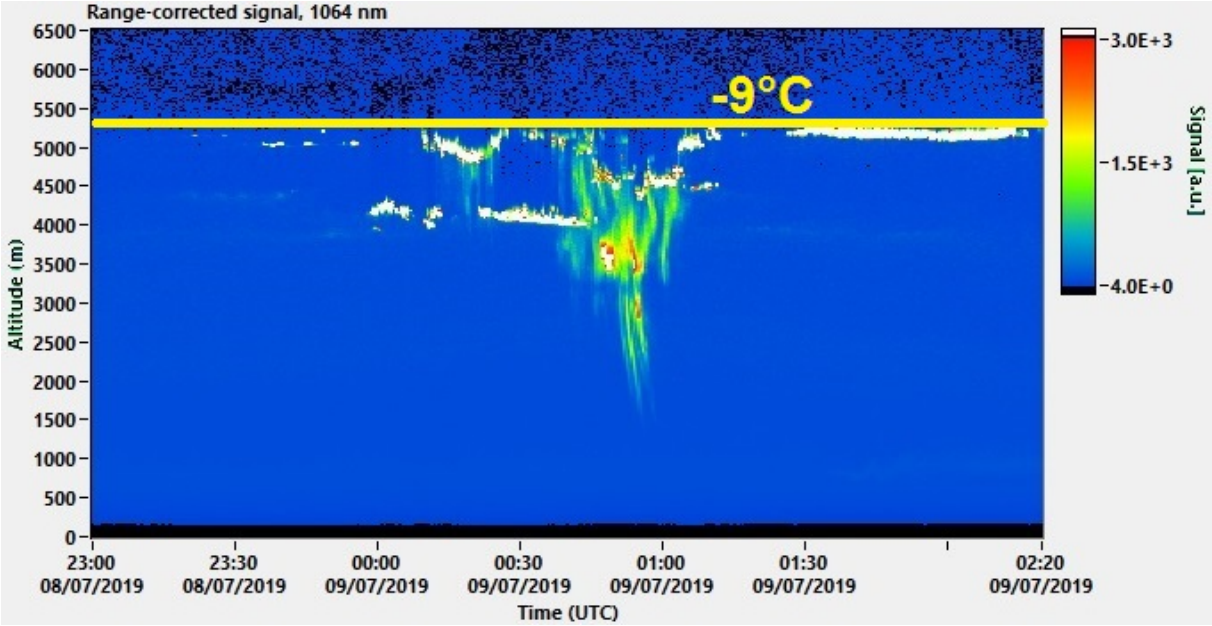

Figure 38: Time-height cross-section of 1064 nm range-corrected signal observed at Dushanbe, Tajikistan, between 8 July 2019 2300 UTC and 9 July 2019, 0220 UTC. Cloud layers and ice virgae are visible in the height range from 2000 to 5200 m height.

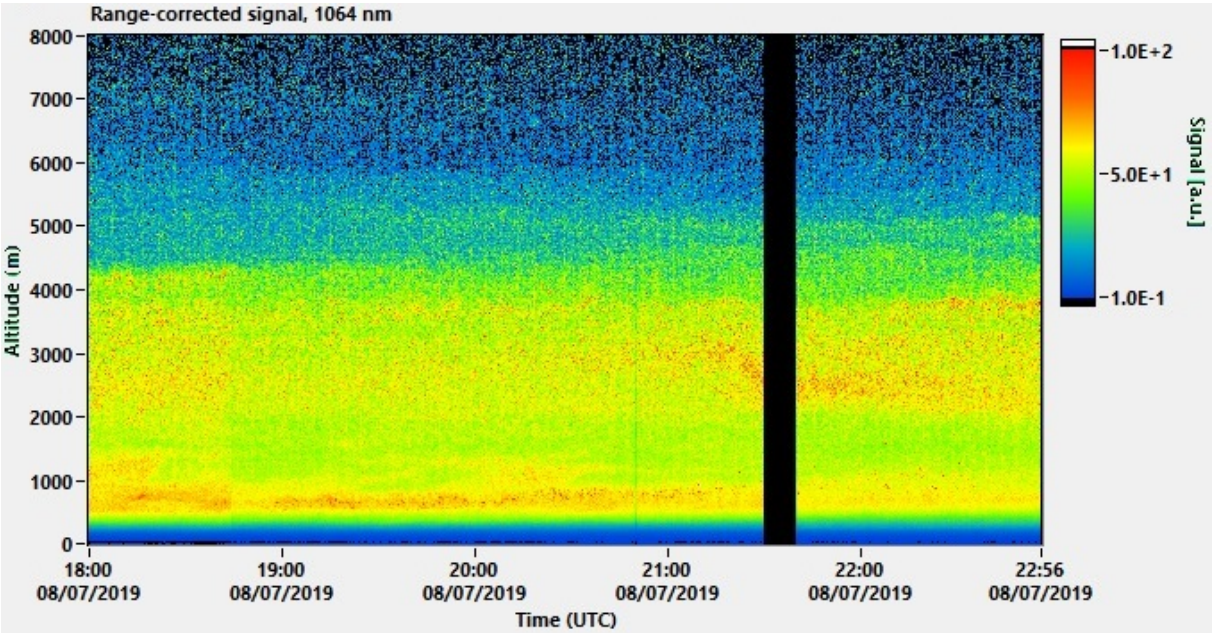

Figure 39: Time-height cross-section of 1064-nm range-corrected signal observed at Dushanbe, Tajikistan, between 8 July 2019, 1800 UTC and 8 July 2019, 2256 UTC. Aerosol layers are visible between the surface and approximately 6000 m height.

3 km height, the particle linear depolarization ratio at 532-nm and 355-nm wavelength are around 0.19 and 0.15, respectively. Probably it is a mixture of desert dust with a high particle linear depolarization ratio and another type of aerosol with a lower particle linear depolarization ratio. Higher up in the profile from approximately 4 km to 6 km height the particle linear depolarization ratio decreases to 0.1 and 0.05 for the 532 and the 355-nm wavelengths, respectively. At this height it is likely that the percentage of the desert dust is decreased, whereas the percentage of the low depolarizing aerosol fraction is larger.
Figure 41c shows the extinction coefficients for 355- and 532-nm wavelengths which were

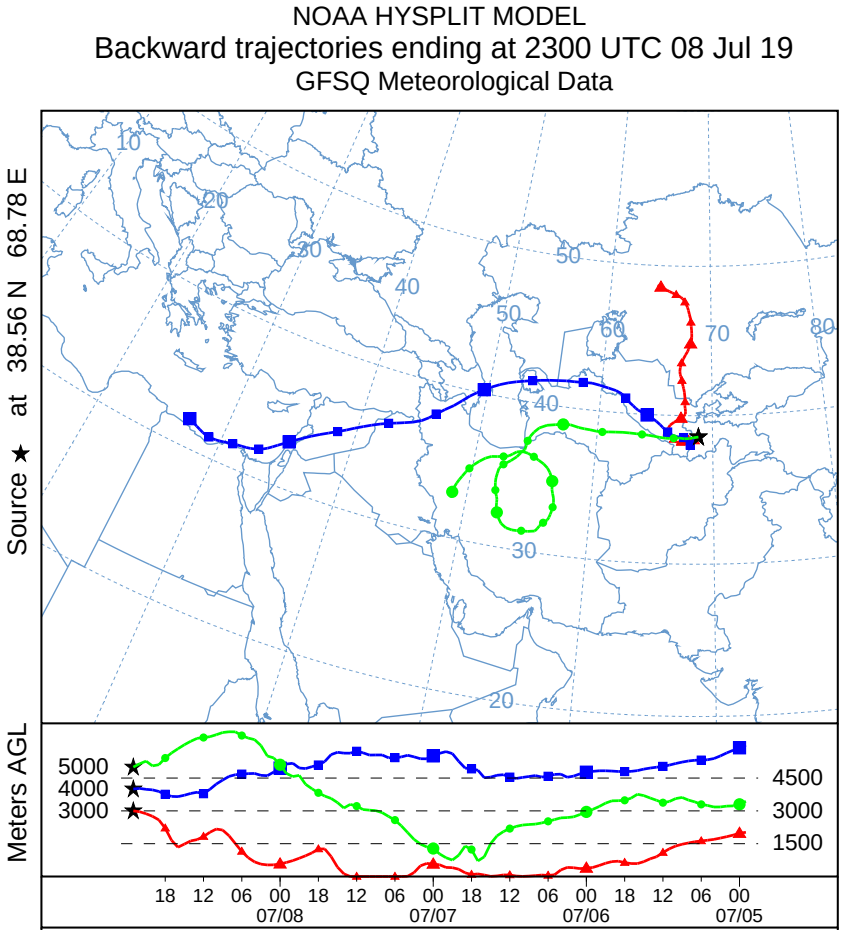

Figure 40: Backward trajectories for altitudes of 3 km (red), 4 km (blue), and 5 km (green) height above Dushanbe ending at 2300 UTC on 8 July 2019 (Hysplit, 2019).

obtained using the Raman method. At all heights, the particle extinction coefficients are lower (30 Mm^{-1}) for the 532-nm wavelength than for the 355-nm wavelength (50 Mm^{-1}). As the particle backscatter coefficient is similar for both wavelengths, this suggests that the lidar ratio is different for both wavelengths. Indeed, the lidar ratio in Fig. 41d at 532-nm and 355-nm are around 25 sr and 50 sr, respectively, and quite constant in height (at above 2 km altitude). At the heights lower than approximately 1 km the lidar ratio is slightly higher at both wavelengths which is another indication for an increased fraction of desert dust which usually has a lidar ratio of around 55 sr (Illingworth et al., 2015).
From the combination of the particle linear depolarization ratio and the lidar ratio, a mixture of desert dust and other aerosol types seems most reasonable. The percentage of desert dust is higher at the lower height (lower lidar ratio and higher particle linear depolarization ratio), whereas at the cloud-relevant height of 4 km to 5 km the percentage of other aerosol types seems to be larger (higher lidar ratio and lower particle linear depolarization ratio). Baars (2012) presents Equation 4.30, here reformulated as Equation 16, which helps to calculate a well-defined dust fraction defined as the ratio of the dust-related and measured particle backscatter coefficient $\beta^{\mathrm{par}}_{\mathrm{dust}}/\beta^{\mathrm{par}}_{\mathrm{meas.}}(\mathrm{z})$:

$$\frac{\beta^{\mathrm{par}}_{\mathrm{dust}}}{\beta^{\mathrm{par}}_{\mathrm{meas.}}}(\mathrm{z}) = \frac{[\delta^{\mathrm{par}}_{\mathrm{meas.}}(\mathrm{z}) - \delta^{\mathrm{par}}_{\mathrm{cont.}}](1+\delta^{\mathrm{par}}_{\mathrm{dust}})}{(\delta^{\mathrm{par}}_{\mathrm{dust}} - \delta^{\mathrm{par}}_{\mathrm{cont}})[1+\delta^{\mathrm{par}}_{\mathrm{meas.}}(\mathrm{z})]} \tag{16}$$

The particle linear depolarization ratios of pure dust $\delta^{\mathrm{par}}_{\mathrm{dust}}$ and of pure smoke $\delta^{\mathrm{par}}_{\mathrm{cont.}}$ at 532 nm are 0.31 and 0.05, respectively. $\delta^{\mathrm{par}}_{\mathrm{meas.}}$ is the measured particle linear depolarization ratio at 532-nm wavelength in the relevant height at around 5 km and is approxi-

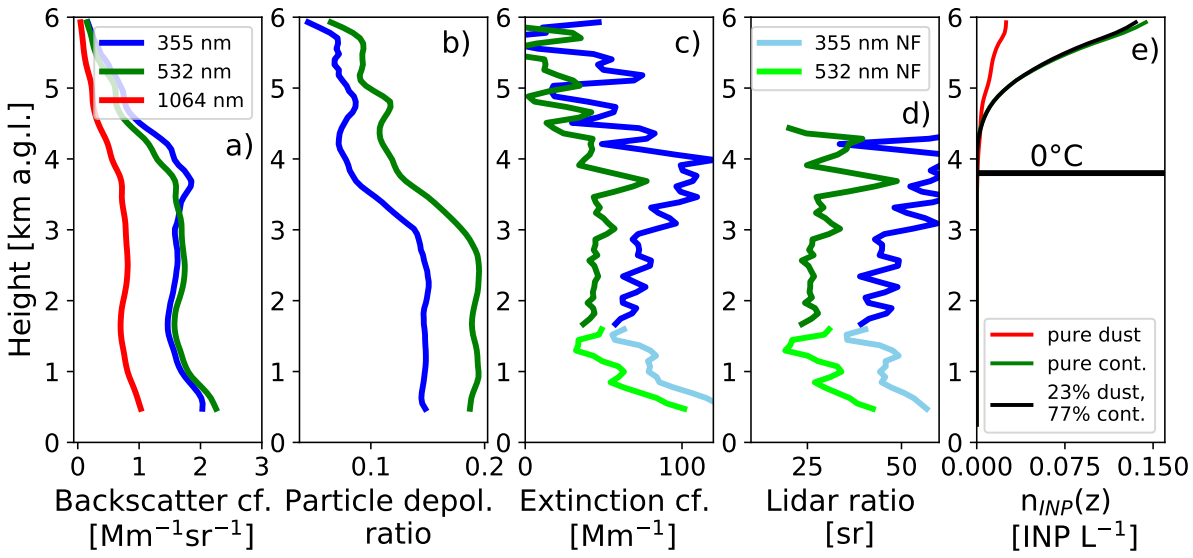

Figure 41: a) particle backscatter coefficient (355 nm, 532 nm, and 1064 nm), b) particle depolarization ratio (355 nm and 532 nm), c) particle extinction coefficient (355 nm and 532 nm) for the near and the far field of view, d) lidar ratio (355 nm and 532 nm) for near and far field of view, e) number of ice nucleating particles retrieved assuming pure desert dust particles (red), pure continental aerosol (green), and a mixture of 74% continental aerosol and 26% desert dust aerosol (black). The profiles are averaged for the night on 8 July 2019 between 1800 UTC and 2256 UTC in Dushanbe using a vertical smoothing of 300 m.

mately 0.10 at 532 nm. Inserting these values into Eq. 16 yields a fraction of dust of 23%. This means that dust contributes approximately 23% to the total particle backscatter coefficient and the remaining 77% are other aerosol types. The remaining aerosol types may be a mixture of pollution and further continental aerosol. However, here the aerosol types which are used for the aerosol-type-dependent INP parametrization are classified as 77% of smoke/continental aerosol for the 532-nm wavelength and 23% of desert dust aerosol. Figure 41e shows the calculated INP profile of this aerosol mixture in black. In the calculation of the profile it was assumed that 77% of the magnitude of the backscatter coefficient were reached by continental aerosol and 23% by desert dust aerosol. Therefore, Eq. 6 and Eq. 7 were used for the INP calculations for dust and continental aerosol, respectively. Furthermore, Fig. 41e shows for comparison also the number of INP when assuming desert dust particles only (red), or continental aerosol particles only (green). The temperature is at around −9°C at the cloud-top height of 5.3 km which is much higher than the temperatures observed in the case studies from Sections 6.1 and 6.2. However, the number of INP is in the same order of magnitude with up to 0.1 L^{-1} at cloud-top when assuming a mixture of 77% continental aerosol and 23% desert dust aerosol. The difference when assuming continental aerosols only is not large anyway (distance of green and black line is low). Only if the amount of desert dust particles is chosen to be 100%, the number of INP at these temperatures would be almost one order of magnitude lower. In comparison to Fig. 26 this is not surprising, as the efficiency of desert dust particles at temperatures slightly below 0°C to act as an INP is way lower than for continental aerosol.

Still, a comparison to the MACC-model-derived INP number concentration is done. The MACC model provides an output of the aerosol mass mixing ratio of 14.0 µg kg^{-1} for the gridpoint of 38.75°N and 68.50°E at the pressure level of 500 hPa on 08 July 2019,

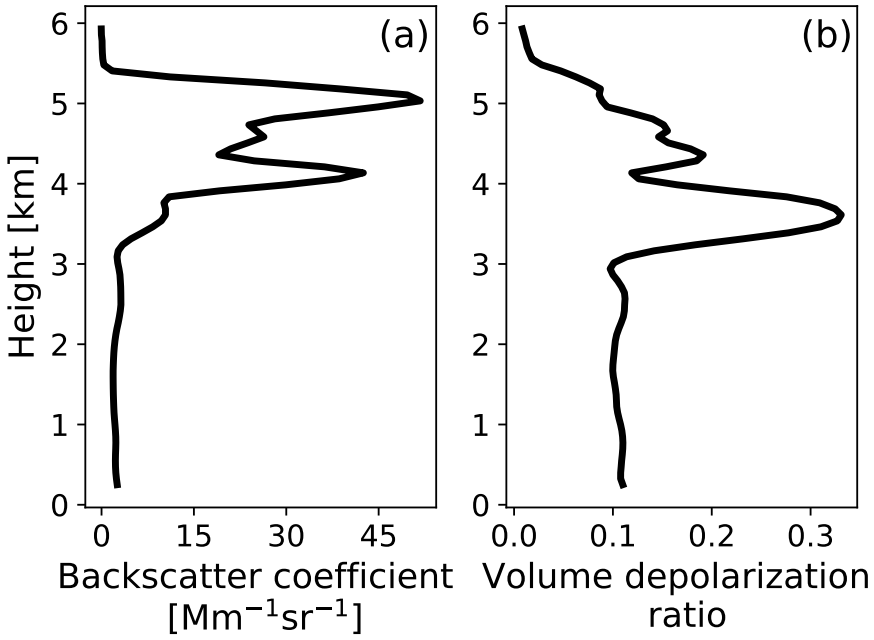

Figure 42: Profiles of the 532-nm wavelength particle backscatter coefficient (a) and the volume depolarization ratio between 0 and 6 km height (b) of a cloud observed with lidar on RV Polarstern on 09 July 2019. The profiles are averaged over the time period from 0000 UTC to 0129 UTC with a vertical smoothing length of 300 m.

2100 UTC. This number is converted into the aerosol mass concentration of 9.5 µg m^{-3} by applying the ideal gas law. In the next step the parametrization for continental aerosol particles from Mamouri and Ansmann (2017) provides the equivalent particle backscatter coefficient of 2.1 $\cdot 10^{-1}$ Mm^{-1}sr^{-1} when assuming 77% continental aerosol and 23% dust with the mentioned constants. Again, the conversion into extinction coefficient, particle number concentration and INP number concentration is done in the same way as for the lidar measurements. The final number concentration of INP derived from the MACC model is $n_{\mathrm{INP,MACC}}$=0.05 L^{-1} assuming 77% continental aerosol and 23% dust.

The case study discussed in this section yields INP number concentrations of approximately 0.1 L^{-1} at the cloud-top height retrieved from lidar observations, and 0.05 L^{-1} retrieved from MACC. This is in the same order of magnitude as for the case studies of RV Polarstern observations shown in Sec. 6.1 and 6.2, even though the cloud-top temperature for this case was more than 10 K above the ones for the two cases. The case study thus shows the relevance of increased aerosol concentrations for the final determination of INP number concentrations.

The classification of the thermodynamic phase of the cloud is done using Fig. 42. It shows the backscatter coefficient (in Fig. 42a) and the volume depolarization ratio (in Fig. 42b) of the 532-nm wavelength between the surface and 6 km height. It is averaged over the time period from 0000 UTC to 0129 UTC with a vertical smoothing length of 300 m. The strongest backscatter coefficient signal is reached between approximately 4 km and 5.2 km. However, the largest volume depolarization ratio signal is reached between 3.2 and 4 km. This means that the largest fraction of nonspherical particles is below the liquid-dominated cloud base. These are interpreted as ice crystals falling out of the cloud. Therefore, the cloud is classified as a mixed-phase cloud, i.e. an ice-containing cloud.

All in all, in this case an INP number concentration of $n_{\mathrm{INP,lidar}}$=0.1 L^{-1} (from lidar)

and $n_{\mathrm{INP,MACC}}$=0.05 L^{-1} (from MACC) was sufficient in order to form ice in the cloud at −9°C.
As described in Sec. 6.1 clouds may contain a small amount of ice water which is less than the threshold $\rho_{\mathrm{IWC,Threshold}}$. It would not be detected by the lidar technique. However, in this case the lidar technique was able to detect ice. Therefore, the ice water content can be assumed as being larger than $\rho_{\mathrm{IWC,Threshold}}$ in this case study. This means that the smallest possible average diameters of the spherical ice crystals would be $d_{\mathrm{icecrystal}}(n_{\mathrm{INP,lidar}})$=275.0 µm and $d_{\mathrm{icecrystal}}(n_{\mathrm{INP,MACC}})$=347.4 µm according to Eq. 14. If the average diameter of the ice crystals would have been smaller (assuming that every INP triggers heterogeneous ice formation) the lidar would probably not have detected ice crystals.
Coming to another conclusion it also means that if there would have been a cloud radar available, it would have measured a lower reflectivity than a certain value. Using Eq. 15 presented in Sec. 6.1 the maximal possible radar reflectivity would be $Z_{\mathrm{lidar}}(0.1\,\mathrm{L}^{-1}, 275.0\,\mu\mathrm{m})$=−20.9 dBZ or $Z_{\mathrm{MACC}}(0.05\,\mathrm{L}^{-1}, 347.4\,\mu\mathrm{m})$=−17.8 dBZ for the lidar-retrieved method and for the MACC-retrieved method, respectively.

7 Summary and Conclusions

Aerosols are an essential driver for the formation of clouds. Liquid water clouds require cloud condensation nuclei, and mixed-phase clouds require ice nucleating particles in order to heterogeneously form ice between 0°C and −38°C. There are different types of heterogeneous freezing which are differently efficient at different temperatures. Contact nucleation is the most efficient heterogeneous freezing type at temperatures slightly below 0°C. Immersion freezing, condensation freezing, and deposition freezing require lower temperatures and higher supersaturation.
Furthermore, different types of aerosols form ice differently efficient. Bioaerosols are most efficient at temperatures slightly below 0°C. Desert dust requires slightly lower temperatures, and black carbon, ammonium sulfates, and organics only need to be taken into account for temperatures below approximately -25°C. Different aerosol types and aerosol loads around the world lead to differences in the fraction of ice-containing clouds at comparable cloud-top temperatures. The fraction of ice-containing clouds varies for different regions, aerosol loads and seasons. Generally, a higher aerosol load leads to a larger fraction of ice-containing clouds.
The detection of aerosol-cloud interaction is a hard but crucial challenge. Aerosol information as well as cloud information need to be measured at the same altitude and time. Originally, models were used in order to retrieve the aerosol properties. In the frame of this study, the ship-based remote sensing lidar technique on board of the RV Polarstern cruise PS116 from Bremerhaven (Germany) to Cape Town (South Africa) from 10 November 2018 to 11 December 2018 was used in order to demonstrate a new approach to relate aerosol properties to the thermodynamic phase of clouds from lidar measurements only. From combined lidar and radiosonde measurements, cloud characteristics like the cloud boundaries, cloud phase, and cloud-top temperature can be determined. We showed that the combination of lidar measurements and backward-trajectory analyzes make it possible to derive aerosol characteristics as aerosol type and load in the vicinity of cloud layers. Furthermore, vertical profiles of ice nucleating particle number concentration can be retrieved. As aerosols within a cloud layer cannot be detected from lidar at the current stage of the technique, aerosol information is retrieved in the vicinity of the cloud closely before or after the cloud was passing over the measurement site.
Before case studies were shown, preparatory studies were conducted. This includes an overview of the route, clouds, and aerosol conditions during the cruise PS116. Clouds occurring in a temperature range between 0°C and −38°C occurred less frequent than other clouds, and the aerosol concentration at the relevant heights of the temperature range was usually low in the range between 10^{-4} µg m^{-3} and 10^{-1} µg m^{-3}. A radiosonde temperature profile was compared to a MACC-model-derived temperature profile. It showed that relative temperature uncertainties are lower than 1%, meaning that the conversion from the MACC model aerosol output in kg kg^{-1} into µg m^{-3} applying the ideal gas law is quite certain. The standard reference backscatter coefficient was set to 10^{-5} km^{-1}sr^{-1} as this reference value was determined as the most appropriate one in a case study. The value is an additive constant to every profile and can be interpreted as a background aerosol concentration. INP parametrizations of continental aerosols and desert dust aerosols were compared, showing that there are quite large differences of up to three orders of magnitude between different INP parametrizations. Furthermore, it seems that for low aerosol concentrations (background conditions) the reference backscatter coefficient contributes largest to the number of INP, such that low background aerosol conditions can hardly be distinguished from high background aerosol conditions with the current active remote sensing lidar technique.

Subsequently to the preparatory studies, three different case studies were presented. The first case study from close to Cape Verde lead to the result that $0.9\,\mathrm{L}^{-1}$ (originally 532-nm particle backscatter coefficient of $5.2\cdot10^{-2}\,\mathrm{Mm}^{-1}\mathrm{sr}^{-1}$) were sufficient in order to form a mixed-phase cloud at a cloud-top temperature of $-24°\mathrm{C}$. From the MACC model the INP concentration was calculated to be $0.5\,\mathrm{L}^{-1}$. The minimal possible diameters of spherical ice crystals were calculated to 160.8 µm and 132.2 µm from MACC and lidar, respectively. The theoretically calculated minimal possible radar reflectivities would have been $-27.9\,\mathrm{dBZ}$ and $-30.5\,\mathrm{dBZ}$ from MACC and lidar, respectively, if a cloud radar would have been available. In the second case study which was from the English Channel the number of INP was lower with $0.1\,\mathrm{L}^{-1}$ derived from lidar, or $0.2\,\mathrm{L}^{-1}$ as derived from the MACC model (original 532-nm backscatter coefficient of $1.1\cdot10^{-2}\,\mathrm{Mm}^{-1}\mathrm{sr}^{-1}$ for the lidar). In this case the cloud was classified as a pure liquid water cloud at a cloud-top temperature of $-21°\mathrm{C}$. The minimal possible diameters of spherical ice crystals were calculated to 218.2 µm and 275.0 µm from MACC and lidar, respectively. The theoretically calculated minimal possible radar reflectivities would have been $-23.9\,\mathrm{dBZ}$ and $-20.9\,\mathrm{dBZ}$ from MACC and lidar, respectively, if a cloud radar would have been available.
As the backscatter coefficients and the retrieved number of INP were generally low during the RV Polarstern cruise, a comparison to a case of a situation with high aerosol load from Dushanbe (Tajikistan) was conducted in the third case study. The particle backscatter coefficient of more than $1\,\mathrm{Mm}^{-1}\mathrm{sr}^{-1}$ was found to be approximately one order of magnitude larger than for most cases observed during PS116. This resulted in an aerosol particle number concentration of n_{290}=2.1 cm^{-3} (compared to $0.57\,\mathrm{cm}^{-3}$ and $0.023\,\mathrm{cm}^{-3}$ in the other case studies) and an INP number concentration of $0.1\,\mathrm{L}^{-1}$ derived from lidar, and $0.05\,\mathrm{L}^{-1}$ derived from MACC. The cloud was found to be a mixed-phase cloud with a top temperature of $-9°\mathrm{C}$. The minimal possible diameters of spherical ice crystals were calculated to 275.0 µm from lidar, and 347.4 µm from MACC. The theoretically calculated minimal possible radar reflectivity would have been $-20.9\,\mathrm{dBZ}$ from lidar, or $-17.8\,\mathrm{dBZ}$ from MACC, if a cloud radar would have been available.
The clouds contained ice for the two cases with the highest particle number concentration. As the cloud-top temperature was warmer (-9°C) in the cloud case in Dushanbe the number of INP was still slightly lower than in the cases observed from aboard RV Polarstern. Nevertheless, the cloud contained ice. However, the largest contribution to the total number of INP for both cases on RV Polarstern were possibly the reference backscatter coefficient as the aerosol concentration was low there and final statements can not be drawn to date. Furthermore, the number concentration of INP is only one physical quantity which is an approach to describe heterogeneous freezing in clouds in the form of a number. However, ice nucleating particles are particles which contain ice nuclei (which trigger ice nucleation) of a certain number on its surface. As a large ice nucleating particle has a larger surface, it is likelier that a large ice nucleating particle contains more ice nuclei than a small ice nucleating particle. The retrieved number concentrations of INP in this study, however, include the particle size only partly (small particles are neglected). Therefore, equal number concentrations of INP with large or with small particle sizes could potentially contain a different number of ice nuclei. Therefore, it could be beneficial to calculate the surface area of the INP and to relate this quantity to the number of available ice nuclei (Hiranuma et al., 2019). Relevant particle size distributions could be retrieved from photometer measurements.
All in all, it is not possible to get statistically significant results from the presented three case studies. The number of clouds in the temperature range from 0°C to $-38°\mathrm{C}$ where heterogeneous freezing is relevant was quite low. The cases in which a large concentration of aerosols reached the relevant temperature range in the subtropics and tropics was even

less frequent. Therefore, it was a hard venture to find representative cases at all. Nevertheless, it was shown that it is possible to directly relate measured aerosol properties to the thermodynamic phase of the cloud. It was possible to apply the presented new approach. Following studies relating aerosol properties and cloud characteristics should in a first instance focus on cases in which the aerosol concentration is high. It is more straight forward to separate signal and background noise for these cases. The certainty of the number of INP increases and if the number of measurements is large, also statistically relevant results could be obtained. An appropriate region would be a non-low latitudinal, polluted (for example desertificated, continental) winter hemispheric (0°C height level is already at lower heights where aerosol concentrations are usually higher) location, like western Asia. A long time series for the lidar in Dushanbe can be a good measurement series for this purpose. Long measurement periods in suitable regions as well as further improving lidar techniques might enable to relate aerosol properties and cloud characteristics also at background aerosol conditions by lidar measurements in the future.
The lidar-only studies presented above would benefit considerably if a co-located cloud radar would be available. The cloud radar would in comparison to the lidar enable to get information on the cloud-top height for clouds with an optical thickness of larger than 3. On the one hand, this would increase the amount of cloud case studies considerably. On the other hand, a bias that could possibly arise when only looking at clouds of optical thicknesses lower than 3 could be neglected. Furthermore, the cloud radar gives information on the ice crystal number concentration and ice water content which are further beneficial units in terms of improving the understanding of cloud processes (Ansmann et al., 2019a). Future ground-based remote-sensing supersites such as the Leipzig Aerosol and Cloud Remote Observation System (LACROS, Bühl et al. (2013b)) are prominent examples where the new approach for relating aerosol properties and heterogeneous freezing in supercooled clouds as presented in this Master's thesis can be applied and improved.

Bibliography

Althausen, D., Engelmann, R., Baars, H., Heese, B., Ansmann, A., Müller, D., and Komppula, M. (2009). Portable Raman Lidar PollyXT for Automated Profiling of Aerosol Backscatter, Extinction, and Depolarization. *Journal of Atmospheric and Oceanic Technology*, pages 2366, DOI 10.1175/2009JTECHA1304.1.

Angelo, C. (2012). Amazon fire analysis hits new heights. *Nature News*.

Ansmann, A., Mamouri, R.-E., Bühl, J., Seifert, P., Engelmann, R., Hofer, J., Nisantzi, A., Atkinson, J. D., Kanji, Z. A., Sierau, B., Vrekoussis, M., and Sciare, J. (2019a). Ice-nucleating particle versus ice crystal number concentration in altocumulus and cirrus embedded in saharan dust: A closure study. *Atmospheric Chemistry and Physics Discussions*, 2019:1–44.

Ansmann, A., Mamouri, R.-E., Bühl, J., Seifert, P., Engelmann, R., Hofer, J., Nisantzi, A., Atkinson, J. D., Kanji, Z. A., Sierau, B., V. M., and Sciare, J. (2019b). Ice-nucleating particle versus ice crystal number concentration in altocumulus and cirrus embedded in saharan dust: A closure study journal: Armospheric chemistry and physics, doi 10.5194/acp-2019-447.

Ansmann, A., Tesche, M., Seifert, P., Althausen, D., Engelmann, R., Fruntke, J., Wandinger, U., Mattis, I., and Müller, D. (2009). Evolution of the ice phase in tropical altocumulus: SAMUM lidar observations over Cape Verde. *Journal of Geophysical Research (Atmospheres)*, pages D17208, DOI 10.1029/2008JD011659.

Baars, H. (2012). Aerosol profiling with lidar in the amazon basin during the wet and dry season 2008.

Bühl, J., Ansmann, A., Seifert, P., Baars, H., and Engelmann, R. (2013a). Toward a quantitative characterization of heterogeneous ice formation with lidar/radar: Comparison of calipso/cloudsat with ground-based observations. *Geophysical Research Letters*, 40(16):4404–4408.

Bühl, J., Seifert, P., Wandinger, U., Baars, H., Kanitz, T., Schmidt, J., Myagkov, A., Engelmann, R., Skupin, A., Heese, B., Klepel, A., Althausen, D., and Ansmann, A. (2013b). Lacros: the leipzig aerosol and cloud remote observations system. *SPIE*, 2013.

Boucher, O., Randall, D., Artaxo, P., Bretherton, C., Feingold, G., Forster, P., Kerminen, V.-M., Kondo, Y., Liao, H., Lohmann, U., Rasch, P., Satheesh, S., Sherwood, S., Stevens, B., and Zhang, X. (2013). Clouds and aerosols. In Climate Change 2013: The Physical Science Basis. Contribution of Working Group I to the Fifth Assessment Report of the Intergovernmental Panel on Climate Change. T.F. Stocker, D. Qin, G.-K. Plattner, M. Tignor, S.K. Allen, J. Doschung, A. Nauels, Y. Xia, V. Bex, and P.M. Midgley. *Eds. Cambridge University Press*, pages 571–657, DOI 10.1017/CBO9781107415324.016.

Box, M. A. and Box, G. P. (2015). Physics of radiation and climate. *CRC Press*.

Bühl, J., Seifert, P., Radenz, M., Baars, H., and Ansmann, A. (2019). Ice crystal number concentration from measurements of lidar, cloud radar and radar wind profiler. *Atmospheric Measurement Techniques Discussions*, 2019:1–25.

Charlson, R. J., Schwartz, S. E., Hales, J. M., Cess, R. D., Coakley, Jr., J. A., Hansen, J. E., and Hofmann, D. J. (1992). Climate Forcing by Anthropogenic Aerosols. *Science*, pages 423–430, DOI 10.1126/science.255.5043.423.

Copernicus (2019). Monitoring Atmospheric Composition and Climate. `https://www.copernicus.eu/en/monitoring-atmospheric-composition-and-climate`.

DeMott, P., Prenni, A., Liu, X., Kreidenweis, S., Petters, M., Twohy, C., Richardson, M., Eidhammer, T., and Rogers, D. (2010). Predicting global atmospheric ice nuclei distributions and their impacts on climate. *Proceedings of the National Academy for Sciences of the United States of America*, pages 11217–11222, DOI 10.1073/pnas.0910818107.

ECMWF (2019a). MACC data ECMWF. `https://www.ecmwf.int/en/research/projects/macc-ii`.

ECMWF (2019b). MACC model levels. `https://www.ecmwf.int/en/forecasts/documentation-and-support/137-model-levels`.

Engelmann, R., Kanitz, T., Baars, H., Heese, B., Althausen, D., Skupin, A., Wandinger, U., Komppula, M., Stachlewska, I. S., Amiridis, V., Marinou, E., Mattis, I., Linné, H., and Ansmann, A. (2016). The automated multiwavelength raman polarization and water-vapor lidar polly^{XT}: the next generation. *Atmospheric Measurement Techniques*, 9(4):1767–1784.

Floutsi, A. (2019). Aerosol characteristics from lidar ratio and depolarization ratio - personal communication.

Gonzalez-Alonso, L., Val Martin, M., and Kahn, R. A. (2019). Biomass-burning smoke heights over the amazon observed from space. *Atmospheric Chemistry and Physics*, 19(3):1685–1702.

Haarig, M., Ansmann, A., Baars, H., Jimenez, C., Veselovskii, I., Engelmann, R., and Althausen, D. (2018). Depolarization and lidar ratios at 355, 532, and 1064 nm and microphysical properties of aged tropospheric and stratospheric Canadian wildfire smoke. *Atmospheric Chemistry & Physics*, pages 11847–11861, DOI 10.5194/acp–18–11847–2018.

Hiranuma, N., Adachi, K., Bell, D. M., Belosi, F., Beydoun, H., Bhaduri, B., Bingemer, H., Budke, C., Clemen, H.-C., Conen, F., Cory, K. M., Curtius, J., DeMott, P. J., Eppers, O., Grawe, S., Hartmann, S., Hoffmann, N., Höhler, K., Jantsch, E., Kiselev, A., Koop, T., Kulkarni, G., Mayer, A., Murakami, M., Murray, B. J., Nicosia, A., Petters, M. D., Piazza, M., Polen, M., Reicher, N., Rudich, Y., Saito, A., Santachiara, G., Schiebel, T., Schill, G. P., Schneider, J., Segev, L., Stopelli, E., Sullivan, R. C., Suski, K., Szakáll, M., Tajiri, T., Taylor, H., Tobo, Y., Ullrich, R., Weber, D., Wex, H., Whale, T. F., Whiteside, C. L., Yamashita, K., Zelenyuk, A., and Möhler, O. (2019). A comprehensive characterization of ice nucleation by three different types of cellulose particles immersed in water. *Atmospheric Chemistry and Physics*, 19(7):4823–4849.

Hogan, R. J., Mittermaier, M. P., and Illingworth, A. J. (2006). The retrieval of ice water content from radar reflectivity factor and temperature and its use in evaluating a mesoscale model. *Journal of Applied Meteorology and Climatology*, 45(2):301–317.

Hoose, C. and Möhler, O. (2012). Heterogeneous ice nucleation on atmospheric aerosols: a review of results from laboratory experiments. *Atmospheric Chemistry & Physics*, pages 9817–9854, DOI 10.5194/acp–12–9817–2012.

Hysplit (2019). Hysplit Trajectoriy. https://www.ready.noaa.gov/HYSPLIT.php.

Illingworth, A. J., Barker, H. W., Beljaars, A., Ceccaldi, M., Chepfer, H., Clerbaux, N., Cole, J., Delanoë, J., Domenech, C., Donovan, D. P., Fukuda, S., Hirakata, M., Hogan, R. J., Huenerbein, A., Kollias, P., Kubota, T., Nakajima, T., Nakajima, T. Y., Nishizawa, T., Ohno, Y., Okamoto, H., Oki, R., Sato, K., Satoh, M., Shephard, M. W., Velázquez-Blázquez, A., Wandinger, U., Wehr, T., and van Zadelhoff, G.-J. (2015). The EarthCARE Satellite: The Next Step Forward in Global Measurements of Clouds, Aerosols, Precipitation, and Radiation. *Bulletin of the American Meteorological Society*, pages 1311–1332, DOI 10.1175/BAMS–D–12–00227.1.

Jimenez, C., Ansmann, A., Donovan, D., Engelmann, R., Malinka, A., Schmidt, J., and Wandinger, U. (2017). Retrieval of microphysical properties of liquid water clouds from atmospheric lidar measurements: Comparison of the Raman dual field of view and the depolarization techniques, Proc. SPIE 10429, 1042907, https://doi.org/10.1117/12.2281806.

Kanitz, T., Seifert, P., Ansmann, A., Engelmann, R., Althausen, D., Casiccia, C., and Rohwer, E. G. (2011). Contrasting the impact of aerosols at northern and southern midlatitudes on heterogeneous ice formation. *Geophysical Research Letters (AGU)*, pages L17802, DOI 10.1029/2011GL048532.

Lihavainen, H., Kerminen, V.-M., and Remer, L. A. (2010). Aerosol-cloud interaction determined by both in situ and satellite data over a northern high-latitude site. *Atmospheric Chemistry & Physics*, pages 10987–10995, DOI 10.5194/acp–10–10987–2010.

Mamouri, R.-E. and Ansmann, A. (2016). Potential of polarization lidar to provide profiles of CCN- and INP-relevant aerosol parameters. *Atmospheric Chemistry & Physics*, pages 5905–5931, DOI 10.5194/acp–16–5905–2016.

Mamouri, R.-E. and Ansmann, A. (2017). Potential of polarization/raman lidar to separate fine dust, coarse dust, maritime, and anthropogenic aerosol profiles. *Atmospheric Measurement Techniques*, 10(9):3403–3427.

Murray, B., O'Sullivan, D., Atkinson, J., and Webb, M. (2012). Ice nucleation by particles immersed in supercooled cloud droplets. *The Royal Society of Chemistry*.

Nakajima, T., Higurashi, A., Kawamoto, K., and Penner, J. E. (2001). A possible correlation between satellite-derived cloud and aerosol microphysical parameters. *Geophysical Research Letters (AGU)*, pages 1171–1174, DOI 10.1029/2000GL012186.

NASA Earth Observatory (2019). Aerosol Optical Depth. https://earthobservatory.nasa.gov/global-maps/MODAL2_M_AER_OD.

Nickovic, S., Kallos, G., Papadopoulos, A., and Kakaliagou, O. (2001). A model for prediction of desert dust cycle in the atmosphere. *JGR Atmospheres (AGU)*, pages 18, DOI 10.1029/2000JD900794.

Pawson, S. (2017). Aerosol transport and assimilation. https://gmao.gsfc.nasa.gov/research/aerosol/modeling/nr1_movie/.

Pratt, K. A., Demott, P. J., French, J. R., Wang, Z., Westphal, D. L., Heymsfield, A. J., Twohy, C. H., Prenni, A. J., and Prather, K. A. (2009). In situ detection of biological particles in cloud ice-crystals. *Nature Geoscience*, pages 398–401, DOI 10.1038/ngeo521.

Pruppacher, H. R. (1995). A New Look at Homogeneous Ice Nucleation in Supercooled Water Drops. *Journal of Atmospheric Sciences*, pages 1924–1933, DOI 10.1175/1520–0469.

Rosenfeld, D., Sherwood, S., Wood, R., and Donner, L. (2014). Climate effects of aerosol-cloud interactions. pages 379–380, DOI 10.1126/science.1247490.

Sassen, K., DeMott, P. J., Prospero, J. M., and Poellot, M. R. (2003). Saharan dust storms and indirect aerosol effects on clouds: CRYSTAL-FACE results. *Geophysical Research Letters (AGU)l*, pages 1633, DOI 10.1029/2003GL017371.

Schmidt, J., Wandinger, U., and Malinka, A. (2013). Dual-field-of-view Raman lidar measurements for the retrieval of cloud microphysical properties. *OSA Publishing*, pages 2235, DOI 10.1364/AO.52.002235.

Schmithüsen, H. (2019). Radiosonde measurements during POLARSTERN cruise PS116.

Schulz, M., de Leeuw, G., and Balkanski, Y. (2004). Sea-salt aerosol source functions and emissions. In Granier, C., Artaxo, P., and Reeves, C. E., editors, *Emissions of Atmospheric Trace Compounds*, pages 333–359, Dordrecht. Springer Netherlands.

Seifert, P., Ansmann, A., Mattis, I., Wandinger, U., Tesche, M., Engelmann, R., Müller, D., PéRez, C., and Haustein, K. (2010). Saharan dust and heterogeneous ice formation: Eleven years of cloud observations at a central European EARLINET site. *Journal of Geophysical Research (Atmospheres)*, pages D20201, DOI 10.1029/2009JD013222.

Seifert, P., Ansmann, A., Müller, D., Wandinger, U., Althausen, D., Heymsfield, A. J., Massie, S. T., and Schmitt, C. (2007). Cirrus optical properties observed with lidar, radiosonde, and satellite over the tropical indian ocean during the aerosol-polluted northeast and clean maritime southwest monsoon. *Journal of Geophysical Research: Atmospheres*, 112(D17).

Seifert, P., Kunz, C., Baars, H., Ansmann, A., Bühl, J., Senf, F., Engelmann, R., Althausen, D., and Artaxo, P. (2015). Seasonal variability of heterogeneous ice formation in stratiform clouds over the Amazon Basin. *Geophysical Research Letters (AGU)*, pages 5587–5593, DOI 10.1002/2015GL064068.

Seifert, P. (2011). Dust-related ice formation in the troposphere: A statistical analysis based on 11 years of lidar observations of aerosols and clouds over Leipzig. `http://nbn-resolving.de/urn:nbn:de:bsz:15-qucosa-71167`.

Seinfeld, J., Bretherton, C., Carslaw, K., Coe, H., DeMott, P., Dunlea, E., Feingold, G., Ghan, S., Guenther, A., Kahn, R., Kraucunas, I., Kreidenweis, S., Molina, M., Nenes, A., Penner, J., Prather, K., Ramanathan, V., Ramaswamy, V., Rasch, P., Ravishankara, A., Rosenfeld, D., Stephens, G., and Wood, R. (2016). Improving our fundamental understanding of the role of aerosolcloud interactions in the climate system. *Proceedings of the National Academy for Sciences of the United States of America*, pages 3113, DOI 10.1073/pnas.1514043113.

Shinozuka, Y., Clarke, A. D., Nenes, A., Jefferson, A., Wood, R., McNaughton, C. S., Ström, J., Tunved, P., Redemann, J., Thornhill, K. L., Moore, R. H., Lathem, T. L., Lin, J. J., and Yoon, Y. J. (2015). The relationship between cloud condensation nuclei (ccn) concentration and light extinction of dried particles: indications of underlying aerosol processes and implications for satellite-based ccn estimates. *Atmospheric Chemistry and Physics*, 15(13):7585–7604.

Twomey, S. (1977). The Influence of Pollution on the Shortwave Albedo of Clouds. *Journal of Atmospheric Sciences*, pages 1149–1154, DOI 10.1175/1520–0469.

Urbanek, B., Groß, S., Wirth, M., Rolf, C., Krämer, M., and Voigt, C. (2018). High depolarization ratios of naturally occurring cirrus clouds near air traffic regions over europe. *Geophysical Research Letters*, 45(23):13,166–13,172.

Vali, G., DeMott, P. J., Möhler, O., and Whale, T. F. (2015). Technical note: A proposal for ice nucleation terminology, journal: Atmospheric chemistry and physics, doi 10.5194/acp-15-10263-2015.

Weitkamp, C. (2005). *Lidar; Range-Resolved Optical Remote Sensing of the Atmosphere*. Springer.

Wex, H., Huang, L., Zhang, W., Hung, H., Traversi, R., Becagli, S., Sheesley, R. J., Moffett, C. E., Barrett, T. E., Bossi, R., Skov, H., Hünerbein, A., Lubitz, J., Löffler, M., Linke, O., Hartmann, M., Herenz, P., and Stratmann, F. (2019). Annual variability of ice-nucleating particle concentrations at different arctic locations. *Atmospheric Chemistry and Physics*, 19(7):5293–5311.

Wood, R. (2012). Stratocumulus clouds. *Monthly Weather Review*, 140(8):2373–2423.

List of Figures

List of Tables

Selbstständigkeitserklärung

Hiermit erkläre ich, dass ich die vorliegende Arbeit selbstständig verfasst habe und keinerlei außer den angegebenen Hilfsmitteln oder Quellen verwendet habe. Jegliche verwendete Literatur oder andere Quelle wurde als solche gekennzeichnet und zitiert. Alle abgebildeten Grafiken, sofern sie nicht mit einem Quellenvermerk versehen sind, wurden von mir selbst erstellt. Des Weiteren wurde diese Arbeit noch nie in gleicher oder ähnlicher Form bei einer anderen Prüfungsbehörde eingereicht.
Ich erkläre mich damit einverstanden, eine positive Bewertung der Arbeit vorausgesetzt, dass Kopien dieser Arbeit in der Bücherei der Fakultät für Physik und Geowissenschaften der Universität Leipzig sowie am Leibniz Institut für Troposphärenforschung in Leipzig zur Verfügung gestellt werden.

Leipzig, 16 November 2019,

Kevin Ohneiser